

Postearthquake Reconnaissance Report on Transportation Infrastructure Impact of the February 27, 2010, Offshore Maule Earthquake in Chile

PUBLICATION NO. FHWA-HRT-11-030

OCTOBER 2011



U.S. Department of Transportation
Federal Highway Administration

Research, Development, and Technology
Turner-Fairbank Highway Research Center
6300 Georgetown Pike
McLean, VA 22101-2296

FOREWORD

On February 27, 2010, a devastating magnitude 8.8 earthquake struck off the coast of the Maule region of Chile, affecting a large area that included Chile's two most populated cities: Concepción and Santiago, the Chilean capital. A transportation infrastructure reconnaissance team (TIRT) was organized by the Federal Highway Administration (FHWA) and performed a thorough postearthquake investigation of highway infrastructure from April 4 to 13, 2010. TIRT was assisted by Chile's Ministry of Public Works and two local universities: Pontifical Catholic University of Chile and University of Chile, both located in Santiago. This report presents the preliminary findings of the earthquake's effects on the transportation infrastructure, including bridges and other highway structures that the team visited during the reconnaissance. This project was funded by FHWA's Innovative Bridge Research and Deployment program.

Jorge E. Pagán-Ortiz
Director, Office of Infrastructure
Research and Development

Notice

This document is disseminated under the sponsorship of the U.S. Department of Transportation in the interest of information exchange. The U.S. Government assumes no liability for the use of the information contained in this document. This report does not constitute a standard, specification, or regulation.

The U.S. Government does not endorse products or manufacturers. Trademarks or manufacturers' names appear in this report only because they are considered essential to the objective of the document.

Quality Assurance Statement

The Federal Highway Administration (FHWA) provides high-quality information to serve Government, industry, and the public in a manner that promotes public understanding. Standards and policies are used to ensure and maximize the quality, objectivity, utility, and integrity of its information. FHWA periodically reviews quality issues and adjusts its programs and processes to ensure continuous quality improvement.

TECHNICAL DOCUMENTATION PAGE

1. Report No. FHWA-HRT-11-030	2. Government Accession No.	3. Recipient's Catalog No.	
4. Title and Subtitle Post-Earthquake Reconnaissance Report on Transportation Infrastructure: Impact of the February 27, 2010, Offshore Maule Earthquake in Chile		5. Report Date October 2011	
		6. Performing Organization Code	
7. Author(s) Wen-Huei Phillip Yen, Genda Chen, Ian Buckle, Tony Allen, Daniel Alzamora, Jeffrey Ger, and Juan G. Arias		8. Performing Organization Report No.	
9. Performing Organization Name and Address Turner-Fairbank Highway Research Center Federal Highway Administration 6300 Georgetown Pike, McLean, VA 22101 Department of Civil, Architectural and Environmental Engineering, Missouri University of Science and Technology 1401 N. Pine St., Rolla, MO 65409 Department of Civil and Environmental Engineering University of Nevada Reno 1664 N. Virginia St., Reno, NV 89557 State Materials Laboratory Washington State Department of Transportation P.O. Box 47365, Olympia, WA 98504		10. Work Unit No. (TRAIS)	
		11. Contract or Grant No.	
12. Sponsoring Agency Name and Address Office of Infrastructure Research and Development Federal Highway Administration 6300 Georgetown Pike McLean, VA 22101-2296		13. Type of Report and Period Covered Final Report: December 2009–Present	
		14. Sponsoring Agency Code	
15. Supplementary Notes The Contracting Officer's Technical Representative (COTR) was W. Phillip Yen, HRDI-50.			
16. Abstract This report documents the findings and lessons learned from the February 27, 2010, M8.8 offshore Maule earthquake in Chile. Fewer than 0.15 percent of the bridges in Chile's inventory, most built after 1995, collapsed or suffered damage that rendered them useless. Many spans of precast prestressed discontinuous girder bridges with continuous decks fell off their supports, probably due to significant in-plane rotation of the superstructure as a result of severe shaking. Lateral steel stoppers used to provide both vertical and lateral restraints on girders were largely unsuccessful due to their inadequate connection detail to cap beams and abutments. Reinforced concrete shear keys performed well as fuses limiting the transfer of excessive seismic loads from the superstructure to the foundation of bridges even though they could be optimized for maximum energy dissipation as part of the lateral restraint system at the bottom flange of girders. Vertical seismic bars were widely used to restrain the vertical motion of decks, and they also performed well. Bridge substructures (foundation, column, and cap beam) generally behaved satisfactorily except for two columns that suffered shear failure due to ground settlement and lateral spreading. All mechanically stabilized earth walls exceeded the expected performance.			
17. Key Words Seismic performance, Bridge damage, Superstructure rotation, Retaining wall, Soil liquefaction, Lateral spreading		18. Distribution Statement No restrictions. This document is available to the public through NTIS: National Technical Information Service 5301 Shawnee Road Alexandria, VA 22312	
19. Security Classif. (of this report) Unclassified	20. Security Classif. (of this page) Unclassified	21. No. of Pages 214	22. Price

SI* (MODERN METRIC) CONVERSION FACTORS

APPROXIMATE CONVERSIONS TO SI UNITS

Symbol	When You Know	Multiply By	To Find	Symbol
LENGTH				
in	inches	25.4	millimeters	mm
ft	feet	0.305	meters	m
yd	yards	0.914	meters	m
mi	miles	1.61	kilometers	km
AREA				
in ²	square inches	645.2	square millimeters	mm ²
ft ²	square feet	0.093	square meters	m ²
yd ²	square yard	0.836	square meters	m ²
ac	acres	0.405	hectares	ha
mi ²	square miles	2.59	square kilometers	km ²
VOLUME				
fl oz	fluid ounces	29.57	milliliters	mL
gal	gallons	3.785	liters	L
ft ³	cubic feet	0.028	cubic meters	m ³
yd ³	cubic yards	0.765	cubic meters	m ³
NOTE: volumes greater than 1000 L shall be shown in m ³				
MASS				
oz	ounces	28.35	grams	g
lb	pounds	0.454	kilograms	kg
T	short tons (2000 lb)	0.907	megagrams (or "metric ton")	Mg (or "t")
TEMPERATURE (exact degrees)				
°F	Fahrenheit	5 (F-32)/9 or (F-32)/1.8	Celsius	°C
ILLUMINATION				
fc	foot-candles	10.76	lux	lx
fl	foot-Lamberts	3.426	candela/m ²	cd/m ²
FORCE and PRESSURE or STRESS				
lbf	poundforce	4.45	newtons	N
lbf/in ²	poundforce per square inch	6.89	kilopascals	kPa

APPROXIMATE CONVERSIONS FROM SI UNITS

Symbol	When You Know	Multiply By	To Find	Symbol
LENGTH				
mm	millimeters	0.039	inches	in
m	meters	3.28	feet	ft
m	meters	1.09	yards	yd
km	kilometers	0.621	miles	mi
AREA				
mm ²	square millimeters	0.0016	square inches	in ²
m ²	square meters	10.764	square feet	ft ²
m ²	square meters	1.195	square yards	yd ²
ha	hectares	2.47	acres	ac
km ²	square kilometers	0.386	square miles	mi ²
VOLUME				
mL	milliliters	0.034	fluid ounces	fl oz
L	liters	0.264	gallons	gal
m ³	cubic meters	35.314	cubic feet	ft ³
m ³	cubic meters	1.307	cubic yards	yd ³
MASS				
g	grams	0.035	ounces	oz
kg	kilograms	2.202	pounds	lb
Mg (or "t")	megagrams (or "metric ton")	1.103	short tons (2000 lb)	T
TEMPERATURE (exact degrees)				
°C	Celsius	1.8C+32	Fahrenheit	°F
ILLUMINATION				
lx	lux	0.0929	foot-candles	fc
cd/m ²	candela/m ²	0.2919	foot-Lamberts	fl
FORCE and PRESSURE or STRESS				
N	newtons	0.225	poundforce	lbf
kPa	kilopascals	0.145	poundforce per square inch	lbf/in ²

*SI is the symbol for the International System of Units. Appropriate rounding should be made to comply with Section 4 of ASTM E380.
(Revised March 2003)

TABLE OF CONTENTS

CHAPTER 1. INTRODUCTION	1
1.1 BACKGROUND	1
1.2 THE TRANSPORTATION INFRASTRUCTURE RECONNAISSANCE TEAM	4
1.2.1 Objective	4
1.2.2 Team Members	4
1.3 REPORT ORGANIZATION	5
CHAPTER 2. GEOLOGY, SEISMOLOGY, AND GROUND MOTIONS	7
2.1 BACKGROUND	7
2.2 GEOLOGY AND SEISMOLOGY	7
2.3 GROUND MOTIONS	10
CHAPTER 3. OVERVIEW OF BRIDGE PERFORMANCE AND SEISMIC DESIGN REQUIREMENTS IN CHILE	23
3.1 OVERVIEW OF BRIDGE PERFORMANCE	23
3.1.1 Damage Statistics.....	23
3.1.2 Bridges Visited By Reconnaissance Team	23
3.1.3 Damage Summary.....	26
3.2. SEISMIC DESIGN REQUIREMENTS FOR BRIDGES	27
CHAPTER 4. STRUCTURAL PERFORMANCE OF HIGHWAY BRIDGES	29
4.1 OVERVIEW	29
4.2 PERFORMANCE OF STRAIGHT CONCRETE BRIDGES	30
4.2.1 Américo Vespucio/Independencia	30
4.2.2 Avenida Chada Acceso Sur Overpass.....	34
4.2.3 Las Mercedes Route 5 Overpass.....	35
4.2.4 Llacolen Bridge Over Biobío River	36
4.2.5 Juan Pablo II Bridge Over Biobío River.....	41
4.2.6 Ramadillas Bridges	46
4.3 PERFORMANCE OF SKEWED AND CURVED CONCRETE AND STEEL BRIDGES	51
4.3.1 Américo Vespucio/Miraflores	51
4.3.2 Américo Vespucio/Lo Echevers	53
4.3.3 Avenida Romero Acceso Sur Overpass	55
4.3.4 Route 5 Railway Overcrossing at Hospital	57
4.3.5 Quilicura Railway Overcrossing at Avenida Manuel Antonio Matta.....	59
4.4 PERFORMANCE OF STEEL BRIDGES	62
4.4.1 Tubul Bridge	62
4.4.2 Cardenal Raúl Silva Henríquez Bridge.....	65
4.4.3 Biobío River Bridge.....	71
4.4.4 Pichibudis Bridge.....	73
4.4.5 El Bar Bridge	76
4.4.6 Itata River Bridge.....	79
4.4.7 Pedestrian Bridge Over Route 5	81

4.5 PERFORMANCE OF OTHER BRIDGE TYPES	82
4.5.1 Claro River Bridges	82
4.5.2 Chepe Railroad Bridge Over Biobío River	87
4.5.3 Maipú River Bridges	90
CHAPTER 5. GEOTECHNICAL PERFORMANCE OF TRANSPORTATION	
INFRASTRUCTURE	93
5.1 OVERVIEW	93
5.2 GEOTECHNICAL OBSERVATIONS REGARDING BRIDGE AND PIER	
STRUCTURES.....	94
5.2.1 Non-Liquefaction Geotechnical Issues Observed for Bridges.....	95
5.2.2 Liquefaction Impact on Performance of Bridge and Pier Structures.....	99
5.2.3 Effect of Regional Ground Uplift Observed for Bridges.....	136
5.3 GEOTECHNICAL OBSERVATIONS REGARDING RETAINING WALL	
PERFORMANCE	138
CHAPTER 6. LESSONS LEARNED FROM THE EARTHQUAKE.....	155
6.1 GENERAL.....	155
6.2 SUPERSTRUCTURE ROTATION.....	155
6.2.1 Skewed Bridges	155
6.2.2 Straight Bridges	157
6.3 GIRDER DAMAGE	158
6.3.1 Fracture of Steel Girders	158
6.3.2 Failure of Concrete Girders	158
6.4 CONNECTION BETWEEN SUPERSTRUCTURE AND SUBSTRUCTURE.....	159
6.4.1 Shear Key and Steel Stopper Failures.....	159
6.4.2 Vertical Seismic Bars.....	159
6.4.3 Bridge Bearings	160
6.5 GIRDER SEAT LENGTH.....	160
6.6 COLUMN SHEAR FAILURE.....	160
6.7 FOUNDATION MOVEMENT AND DAMAGE.....	160
6.7.1 Overview.....	160
6.7.2 Sites Not Affected by Liquefaction	160
6.7.3 Sites Affected by Liquefaction	161
6.8 RETAINING WALLS AND ROADWAY FILL	161
CHAPTER 7. CONCLUSIONS AND RECOMMENDATIONS	163
7.1 GENERAL.....	163
7.2 CONCLUSIONS ON TRANSPORTATION INFRASTRUCTURE	
PERFORMANCE.....	163
7.3 RECOMMENDATIONS FOR IMMEDIATE IMPLEMENTATION.....	163
7.3.1 Diaphragms in Concrete Girder Superstructures	163
7.3.2 Support Length.....	164
7.3.3 Lateral Seismic Restraints.....	164
7.3.4 Substructure Design.....	164
7.3.5 Retaining Wall Design.....	164
7.4 RECOMMENDATIONS FOR FUTURE WORK AND RESEARCH NEEDS	165
7.4.1 Structural Engineering Recommendations	165
7.4.2 Geotechnical Engineering Recommendations	167

APPENDIX A. SUBSURFACE DATA	169
A.1 SUBSURFACE DATA.....	169
A.1.1 Subsurface Data for Américo Vespucio/Miraflores (Site 1).....	169
A.1.2 Subsurface data for Américo Vespucio/Lo Echevers (Site 2)	170
A.1.3 Subsurface Data for Avenida Romero Acceso Sur (Site 7)	171
A.1.4 Subsurface Data for Avenida Chada Acceso Sur (Site 8)	173
A.1.5 Subsurface Data for Route 5 Railway Overcrossing at Hospital (Site 10)	176
A.1.6 Subsurface Data for Via Elevada 21 de Mayo/Cruce Ferroviario (Site 28)	177
APPENDIX B. SEISMIC DESIGN REQUIREMENTS FOR BRIDGES AND WALLS	
IN CHILE	185
B.1 SEISMIC DESIGN REQUIREMENTS FOR BRIDGES	185
B.1.1 Analysis Methods	186
B.1.2 Response Modification Factors (<i>R</i>).....	189
B.1.3 Determination of Elastic Forces and Displacements.....	190
B.1.4 Combination of Forces in Two Perpendicular Directions.....	190
B.1.5 Minimum Support Length.....	191
B.1.6 Modified Design Forces for Structural Elements and Connections	191
B.1.7 Modified Design Forces for Foundations.....	191
B.1.8 Seismic Design of Foundations, Abutments, and Retaining Walls.....	192
B.1.9 Seismic Design of Reinforced Concrete Elements	192
B.1.10 Forces from Plastic Hinges on Piers or Columns.....	192
B.1.11 Diaphragms	192
B.1.12 Anchor Bars (Seismic Bars).....	193
B.1.13 Lateral Stoppers (Shear Keys).....	193
B.1.14 Seismic Joints.....	193
B.1.15 Seismic Isolation Systems	193
B.2. SEISMIC DESIGN REQUIREMENTS FOR WALLS.....	193
ACKNOWLEDGMENTS	195
REFERENCES.....	197

LIST OF FIGURES

Figure 1. Map. Site locations visited by TIRT.....	2
Figure 2. Photo. TIRT team members and Chilean support personnel.....	5
Figure 3. Map. Location of epicenter, seismic recording stations, and TIRT sites	7
Figure 4. Map. Historic seismicity for Chile	8
Figure 5. Illustration. Conceptual diagram of a subduction zone earthquake	9
Figure 6. Illustration. Offshore Maule earthquake aftershock distribution with depth	10
Figure 7. Illustration. Accelerogram from Universidad de Chile, Depto. Ing. Civil (interior building).....	12
Figure 8. Illustration. Response spectra from Universidad de Chile, Depto. Ing. Civil (interior building).....	12
Figure 9. Illustration. Accelerogram from CRS Maipú RM.....	13
Figure 10. Illustration. Response spectra from CRS Maipú RM.....	13
Figure 11. Illustration. Accelerogram from Hospital de Curicó.....	14
Figure 12. Illustration. Response spectra from Hospital de Curicó.....	14
Figure 13. Illustration. Accelerogram from San Pedro De La Paz, Colegio Concepción	15
Figure 14. Illustration. Response spectra from San Pedro De La Paz, Colegio Concepción	15
Figure 15. Map. Locations of ground motion sensors and structures visited by TIRT— Santiago vicinity	16
Figure 16. Map. Locations of ground motion sensors and structure visited by TIRT— Santiago to Rancagua.....	17
Figure 17. Map. Locations of ground motion sensors and structures visited by TIRT— Curicó, Talca, Iloca vicinity.....	18
Figure 18. Map. Locations of ground motion sensors and structures visited by TIRT— Concepción vicinity	19
Figure 19. Map. Locations of ground motion sensors and structures visited by TIRT— Maule epicenter to Tubul vicinity.....	20
Figure 20. Illustration. Geologic cross section of Concepción.....	22
Figure 21. Map. Damaged sections in downtown Concepción	22
Figure 22. Map. Seismic zone map for central Chile	28
Figure 23. Photo. Damage to eastbound Independencia bridge.....	30
Figure 24. Photo. Curtain wall at east abutment of eastbound Independencia bridge.....	30
Figure 25. Photo. Damage to steel stoppers on eastbound Independencia bridge.....	31
Figure 26. Illustration. Details of steel stoppers	31
Figure 27. Photo. Typical flared wall pier of westbound Independencia bridge.....	32
Figure 28. Photo. Displaced seismic bar on westbound Independencia bridge.....	32
Figure 29. Photo. Shear key damage at abutment of westbound Independencia bridge	32
Figure 30. Photo. Shear key damage at intermediate bents of westbound Independencia bridge ...	32
Figure 31. Photo. Westbound Independencia bridge.....	33
Figure 32. Photo. Entrance ramp to westbound Independencia bridge	33
Figure 33. Photo. Shear key damage at entrance ramp abutment.....	33
Figure 34. Photo. Flared wall pier of exit ramp from westbound Independencia bridge	33
Figure 35. Photo. Close-up of damage to exit ramp from westbound Independencia bridge.....	34
Figure 36. Photo. Curtain wall shear failure at abutment of Chada bridge	34
Figure 37. Photo. Bottom flange damage to Chada bridge.....	34

Figure 38. Photo. Curtain wall damage at bent of Chada bridge	35
Figure 39. Photo. Soil separation from column of Chada bridge	35
Figure 40. Illustration. Plan view of superstructure rotation of Chada bridge	35
Figure 41. Photo. Las Mercedes bridge and girder unseating at abutments	36
Figure 42. Photo. Llacolen bridge looking south-southwest	36
Figure 43. Photo. Unseated simply supported span in eastern approach to Llacolen bridge	37
Figure 44. Photo. Abutment at unseated end of span in eastern approach to Llacolen bridge	37
Figure 45. Photo. Concrete spalling beneath cap beam of eastern approach to Llacolen bridge	37
Figure 46. Photo. Flexural cracks at the level of rip rap on eastern approach to Llacolen bridge	38
Figure 47. Photo. Close-up view of cracks at the level of rip rap on eastern approach to Llacolen bridge	38
Figure 48. Photo. Ground settlement and lateral movement of eastern approach to Llacolen bridge	38
Figure 49. Photo. Exterior face of westbound ramp to Llacolen bridge at the river end	39
Figure 50. Photo. Interior face of westbound ramp to Llacolen bridge at the river end	39
Figure 51. Photo. Bent of westbound ramp to Llacolen bridge	39
Figure 52. Photo. Seismic bar condition on westbound ramp to Llacolen bridge	39
Figure 53. Photo. Neoprene pad degradation on westbound ramp to Llacolen bridge	40
Figure 54. Photo. Columns with soil marks indicating ground settlement at west end of Llacolen bridge	40
Figure 55. Photo. Sand boils near columns at west end of Llacolen bridge	40
Figure 56. Photo. Spalling in deck slab at west end of Llacolen bridge	40
Figure 57. Photo. Horizontal crack in web of end girders at west end of Llacolen bridge	41
Figure 58. Photo. Spalling of shear key at southwest abutment of Llacolen bridge	41
Figure 59. Photo. Approaches to Juan Pablo II bridge	41
Figure 60. Photo. Southwest view of northern approach to Juan Pablo II bridge, facing Biobío River	42
Figure 61. Photo. Northeast view of northern approach to Juan Pablo II bridge, facing away from Biobío River	42
Figure 62. Photo. Intermediate bent of northern approach to Juan Pablo II bridge	42
Figure 63. Photo. Column settlement under approach to Juan Pablo II bridge (cracks on far side)	43
Figure 64. Photo. Reduced column height due to shear failure under approach to Juan Pablo II bridge	43
Figure 65. Photo. Soil surface on far side of undamaged column under approach to Juan Pablo II bridge	43
Figure 66. Photo. Cracks on far side of undamaged column under approach to Juan Pablo II bridge	44
Figure 67. Photo. Differential settlement underneath first span over water at northern end of Juan Pablo II bridge	44
Figure 68. Photo. Shear failure in upstream column at northern end of Juan Pablo II bridge	45
Figure 69. Photo. Front face of failure plane at northern end of Juan Pablo II bridge	45
Figure 70. Photo. Back face of failure plane at northern end of Juan Pablo II bridge	45
Figure 71. Photo. Shear failure in downstream column at northern end of Juan Pablo II bridge	46
Figure 72. Photo. Satellite image of Ramadillas bridges	46
Figure 73. Photo. Side view of east Ramadillas bridge	47
Figure 74. Photo. Wall-type pier beneath east Ramadillas bridge	47
Figure 75. Photo. Deck misalignment under east Ramadillas bridge	47

Figure 76. Photo. Sand boils close to pier under east Ramadillas bridge.....	48
Figure 77. Photo. Overview of west Ramadillas bridge	48
Figure 78. Photo. Abutment damage beneath west Ramadillas bridge	49
Figure 79. Photo. Pier rotation in collapsed span of west Ramadillas bridge	49
Figure 80. Photo. Sand boils near collapsed span in west Ramadillas bridge	49
Figure 81. Photo. Settlement at south abutment under east Ramadillas bridge.....	50
Figure 82. Photo. Sliding at south abutment under west Ramadillas bridge	50
Figure 83. Photo. Block flow toward river due to liquefaction on south bank of Ramadillas bridges.....	50
Figure 84. Photo. Northeast end of Miraflores bridge	51
Figure 85. Photo. Southwest end of Miraflores bridge	51
Figure 86. Photo. Top view of Miraflores bridge from far side	51
Figure 87. Photo. Bottom view of Miraflores bridge from near side	52
Figure 88. Photo. Collapsed span of Miraflores bridge	52
Figure 89. Photo. Miraflores bridge after removal of superstructure	52
Figure 90. Photo. Acute corner of southwest abutment of Miraflores bridge	53
Figure 91. Photo. Obtuse corner of southwest abutment of Miraflores bridge.....	53
Figure 92. Photo. Collapsed northeast-bound Lo Echevers bridge	53
Figure 93. Photo. Three unseated spans of northeast-bound Lo Echevers bridge.....	54
Figure 94. Photo. Failure of a steel stopper on Lo Echevers bridge.....	54
Figure 95. Photo. Displaced elastomeric bearing on Lo Echevers bridge	54
Figure 96. Illustration. Intermediate bent details for Romero bridge	55
Figure 97. Photo. Collapse of Romero bridge	55
Figure 98. Photo. Seismic bars at west abutment of Romero bridge.....	56
Figure 99. Photo. Seismic bars at east abutment of Romero bridge.....	56
Figure 100. Photo. Pounding at west abutment of Romero bridge.....	56
Figure 101. Photo. Back wall and wing wall damage at west abutment of Romero bridge.....	57
Figure 102. Photo. Three bridges (one demolished) at Route 5 overcrossing at Hospital	57
Figure 103. Photo. Collapse of bridge at Route 5 overcrossing at Hospital.....	57
Figure 104. Photo. Damage at north abutment of Route 5 overcrossing at Hospital	58
Figure 105. Photo. Damage at south abutment of Route 5 overcrossing at Hospital	59
Figure 106. Photo. Overview of Quilicura railway overcrossing	59
Figure 107. Photo. Cross frames on Quilicura railway overcrossing	60
Figure 108. Photo. Stiffeners on Quilicura railway overcrossing.....	60
Figure 109. Photo. East abutment of Quilicura railway overcrossing	60
Figure 110. Photo. West abutment of Quilicura railway overcrossing.....	61
Figure 111. Photo. West span of Quilicura railway overcrossing lowered onto sandbank	61
Figure 112. Photo. Damage to anchor bolts on Quilicura railway overcrossing	61
Figure 113. Photo. Damage to cross frame on Quilicura railway overcrossing	62
Figure 114. Photo. Unseating at southern ends of each span of Tubul bridge	62
Figure 115. Photo. Punching of Tubul bridge deck into back wall	62
Figure 116. Photo. Buckling of pavement at north abutment of Tubul bridge.....	63
Figure 117. Photo. Span 6 of Tubul bridge, unseated at north end during an aftershock.....	63
Figure 118. Photo. Bottom flange buckling and concrete spalling on Tubul bridge	64
Figure 119. Photo. Shear crack in Tubul bridge	64
Figure 120. Photo. Tilting wall pier on Tubul bridge.....	64
Figure 121. Photo. Spalling due to shear action and vertical crack in Tubul bridge	65

Figure 122. Photo. Crack in footing of Tubul bridge	65
Figure 123. Photo. Cardenal Raúl Silva Henríquez bridge looking south.....	66
Figure 124. Photo. Elastomeric pad and stopper over bent on Cardenal Raúl Silva Henríquez bridge	66
Figure 125. Photo. Girder offset and cross frame buckling on Cardenal Raúl Silva Henríquez bridge	67
Figure 126. Photo. Cross frame buckling on Cardenal Raúl Silva Henríquez bridge	67
Figure 127. Photo. Girder damage at northeast abutment of Cardenal Raúl Silva Henríquez bridge	68
Figure 128. Photo. Temporary repair at northeast abutment of Cardenal Raúl Silva Henríquez bridge	68
Figure 129. Photo. Spans and pile bents of southwest portion of Cardenal Raúl Silva Henríquez bridge	69
Figure 130. Photo. Erosion of alluvial material around bent legs of Cardenal Raúl Silva Henríquez bridge.....	69
Figure 131. Photo. Debris-impact hole in bent leg of Cardenal Raúl Silva Henríquez bridge.....	69
Figure 132. Photo. Fillet weld fractures at the girder-to-abutment connection on the Cardenal Raúl Silva Henríquez bridge.....	70
Figure 133. Photo. Close-up of girder end on Cardenal Raúl Silva Henríquez bridge.....	70
Figure 134. Photo. Close-up of transverse stiffeners on Cardenal Raúl Silva Henríquez bridge	70
Figure 135. Photo. Collapsed spans in Biobío River bridge.....	71
Figure 136. Photo. Unseated spans in Biobío River bridge.....	72
Figure 137. Photo. Lateral spreading near east end of Biobío River bridge.....	72
Figure 138. Photo. Collapsed spans and piers of Biobío River bridge.....	72
Figure 139. Photo. Cracks in pile caps of Biobío River bridge	72
Figure 140. Photo. Satellite image of Pichibudis bridge	73
Figure 141. Photo. Cross frames in Pichibudis bridge.....	73
Figure 142. Photo. Web stiffeners in Pichibudis bridge	74
Figure 143. Photo. Offset in girder top flange of south abutment of Pichibudis bridge.....	74
Figure 144. Photo. Offset in handrail on south abutment of Pichibudis bridge.....	74
Figure 145. Photo. X-braces damage in south abutment of Pichibudis bridge.....	75
Figure 146. Photo. Diaphragm crushing in south abutment of Pichibudis bridge.....	75
Figure 147. Photo. Damage on south abutment due to corrosion in Pichibudis bridge.....	76
Figure 148. Photo. Satellite image of El Bar bridge.....	76
Figure 149. Photo. Side view of El Bar bridge	77
Figure 150. Photo. Retrofit girder connections on El Bar bridge	77
Figure 151. Photo. Retrofit deck connections on El Bar bridge	77
Figure 152. Photo. Lateral deformation at south abutment of El Bar bridge.....	78
Figure 153. Photo. Damage at south abutment of El Bar bridge	78
Figure 154. Photo. Damage to rebar X-brace system on north abutment of El Bar bridge.....	78
Figure 155. Photo. Damage to north abutment back wall of El Bar bridge.....	79
Figure 156. Photo. Satellite image of Itata River bridge	79
Figure 157. Photo. Side view and superstructure details for Itata River bridge	80
Figure 158. Photo. Girder supports at each pier of Itata River bridge.....	80
Figure 159. Photo. Damage to girder supports of Itata River bridge.....	81
Figure 160. Photo. Damaged Route 5 pedestrian bridge	81
Figure 161. Photo. Steel girder on neoprene pad at abutment of Route 5 pedestrian bridge	82

Figure 162. Photo. End cross frame near collapsed span of Route 5 pedestrian bridge	82
Figure 163. Photo. Anchor bolt failure (shear and pull out) on Route 5 pedestrian bridge.....	82
Figure 164. Illustration. Highway bridges crossing Claro River before earthquake	83
Figure 165. Photo. Collapse of masonry arch bridge at Claro River	83
Figure 166. Photo. Close-up view of collapsed bridge at Claro River	83
Figure 167. Photo. Deck slab and crown of arch on Claro River bridge.....	84
Figure 168. Photo. Pier of Claro River bridge	84
Figure 169. Photo. Foundation of Claro River bridge	85
Figure 170. Illustration. Scenario for the progressive collapse of Claro River bridge	86
Figure 171. Photo. North end of Chepe railroad bridge over roadway.....	87
Figure 172. Photo. River spans of Chepe railroad bridge.....	87
Figure 173. Photo. South end of Chepe railroad bridge	87
Figure 174. Photo. Bottom view and cross section on north end of Chepe railroad bridge	87
Figure 175. Photo. Section on south end of Chepe railroad bridge	88
Figure 176. Illustration. Settlement and lateral movement of wall and bent due to ground spreading under Chepe railroad bridge	88
Figure 177. Photo. Settlement and tilting of bent on Chepe railroad bridge	89
Figure 178. Photo. Settlement behind retaining wall on Chepe railroad bridge.....	89
Figure 179. Photo. Ruptured cross bracing at south end of Chepe railroad bridge	90
Figure 180. Photo. Fractured steel piles at south end of Chepe railroad bridge	90
Figure 181. Photo. Three parallel bridges crossing Maipú River south of Santiago	90
Figure 182. Photo. Crushing of haunches at pier 3 of Maipú River bridge.....	91
Figure 183. Photo. Shear cracks at span 1 of Maipú River bridge	91
Figure 184. Photo. Longitudinal and vertical seismic forces in haunches at pier 3 of Maipú River bridge.....	91
Figure 185. Photo. Damage at Romero bridge and shaft foundation supporting abutment (collapsed superstructure removed)	96
Figure 186. Photo. Interior pier of Chada structure with 5.8- to 7.8-inch (150- to 200-mm) gap in soil transverse to bridge centerline.....	97
Figure 187. Photo. East abutment of Chada structure showing large pavement crack directly below bridge centerline.....	97
Figure 188. Illustration. Fill slumping observed for bridge sites 7 and 8.....	98
Figure 189. Photo. Fill slumping observed at Romero bridge.....	98
Figure 190. Photo. View of roadway fill failure from abutment of Route 5 railway crossing at Hospital.....	99
Figure 191. Photo. Close-up of approach fill failure and damaged sign bridge	99
Figure 192. Photo. Lateral spreading at Mataquito bridge	101
Figure 193. Photo. Lateral spreading at Mataquito bridge with lateral movement beneath and around bridge	101
Figure 194. Photo. Lateral spreading and ground failure at old Ramadillas bridge	102
Figure 195. Photo. Sand boils at southwest end of Llacolen bridge.....	102
Figure 196. Photo. Ejected sand due to liquefaction and ground failure at La Mochita bridge ..	103
Figure 197. Photo. Severe ground failure at La Mochita bridge	104
Figure 198. Photo. Lateral spreading and ground failure at Raqui 2 bridge.....	104
Figure 199. Photo. San Nicolás bridge center pier settlement probably due to liquefaction of soil layers beneath river	105

Figure 200. Photo. Ramps at Juan Pablo II bridge where existing ground was improved with DDC	106
Figure 201. Photo. Lateral movement of fill in ramps at Juan Pablo II bridge	106
Figure 202. Photo. Abutment fill settlement of northeast abutment of Mataquito bridge.....	108
Figure 203. Photo. Soil settlement without bridge settlement at northeast abutment of Mataquito bridge.....	108
Figure 204. Photo. Soil settlement at interior pier at northeast abutment of Mataquito bridge...	109
Figure 205. Photo. Abutment fill settlement at northwest abutment of Raqui 1 bridge	110
Figure 206. Photo. Abutment and girders shoved into each other and deck at the northwest abutment of the Raqui 1 bridge.....	111
Figure 207. Photo. Raqui 1 bridge viewed from north side.....	111
Figure 208. Photo. Evidence of ground failure perpendicular to roadway centerline at northwest approach of Raqui 1 bridge	112
Figure 209. Map. Aerial view of Biobío River and crossings	113
Figure 210. Photo. Evidence of slope instability due to liquefaction at northeast abutment and approaches of Llacolen bridge	113
Figure 211. Illustration. Plan view of liquefaction-induced slide at northeast abutment of Llacolen bridge	114
Figure 212. Photo. Settlement due to liquefaction-induced slope instability at northeast end of Llacolen bridge	114
Figure 213. Photo. Settlement and lateral ground movement of interior pier at northeast end of Llacolen bridge	115
Figure 214. Photo. Lateral ground and foundation movement at interior pier and fallen span at northeast end of Llacolen bridge.....	116
Figure 215. Photo. Close-up of cracked column at northeast end of Llacolen bridge.....	116
Figure 216. Photo. Wall settlement due to slope movement and instability caused by liquefaction at northwest end of Chepe railroad bridge.....	117
Figure 217. Photo. Settlement of approach structure for Juan Pablo II bridge.....	118
Figure 218. Photo. Close-up of settlement of approach structure for Juan Pablo II bridge.....	118
Figure 219. Photo. Roadway settlement due to settlement of approach structure pier foundations for Juan Pablo II bridge.....	119
Figure 220. Photo. Roadway settlement due to settlement of mainline pier foundations for Juan Pablo II Bridge.....	119
Figure 221. Photo. Liquefaction-induced differential settlement of mainline pier foundations supporting Juan Pablo II bridge	120
Figure 222. Photo. Damage to pier columns for mainline Juan Pablo II bridge.....	120
Figure 223. Photo. View of collapsed spans from northeast river bank of Biobío River.....	121
Figure 224. Photo. Close-up of old Biobío River bridge showing exposed pile foundations	121
Figure 225. Photo. Ground failure near northeast abutment of old Biobío River bridge	122
Figure 226. Photo. Tilting of northeast abutment pier wall of old Biobío River bridge	122
Figure 227. Photo. Ground failure of north approach fill for La Mochita bridge.....	123
Figure 228. Photo. La Mochita bridge north approach fill liquefaction-induced ground failure...	124
Figure 229. Photo. La Mochita bridge north approach fill and edge of dredging pit	124
Figure 230. Photo. La Mochita bridge deck and girder lateral movement	125
Figure 231. Photo. La Mochita bridge deck and girder lateral movement and approach fill settlement	126
Figure 232. Photo. La Mochita bridge lateral bridge deck and girder at south abutment	126

Figure 233. Photo. Southeast approach fill damage at Raqui 2 bridge.....	127
Figure 234. Photo. Collapsed and shifted spans at Raqui 2 bridge as viewed from base of southeast abutment.....	128
Figure 235. Photo. Collapsed and shifted spans at Raqui 2 bridge due to liquefaction.....	128
Figure 236. Photo. South approach fill damage and collapsed spans at Tubul Bridge.....	129
Figure 237. Photo. Settlement of fill beside the south abutment of Tubul bridge.....	129
Figure 238. Photo. Overview of damage to south abutment of Tubul bridge.....	130
Figure 239. Photo. Close-up of exposed pile and pile cap damage on south abutment of Tubul bridge.....	130
Figure 240. Photo. Overview of Tubul bridge north abutment.....	131
Figure 241. Photo. Tubul bridge collapsed spans and substructure.....	131
Figure 242. Photo. Puerto de Coronel Muelle foundation displacement and bending.....	132
Figure 243. Photo. Close-up of Puerto de Coronel Muelle foundation displacement and bending.....	132
Figure 244. Photo. View northeast from Tubul bridge south abutment showing areas left dry and boats left above the new mean water level.....	137
Figure 245. Photo. Tubul bridge with boats run through by old timber pilings.....	137
Figure 246. Photo. Retaining wall at Américo Vespucio/Miraflores.....	139
Figure 247. Photo. Retaining wall at Américo Vespucio/Lo Echevers.....	140
Figure 248. Photo. Retaining wall at 14 de la Fama.....	140
Figure 249. Photo. Retaining wall at Quilicura railroad overcrossing.....	140
Figure 250. Photo. Retaining wall at Américo Vespucio/Independencia eastbound.....	140
Figure 251. Photo. Retaining wall at Américo Vespucio/Independencia westbound.....	140
Figure 252. Photo. Retaining wall at Maipú River bridge.....	141
Figure 253. Photo. Retaining wall at Estribo Francisco Mostazal (Avenida Independencia).....	141
Figure 254. Photo. Retaining wall at Chepe railroad bridge over Biobío River.....	141
Figure 255. Photo. Retaining wall at Raqui 2.....	141
Figure 256. Photo. South retaining wall at Juan Pablo II.....	141
Figure 257. Photo. North retaining wall at Juan Pablo II.....	142
Figure 258. Photo. Retaining wall at 21 de Mayo.....	142
Figure 259. Photo. Retaining wall at Rotonda General Bonilla.....	142
Figure 260. Photo. Retaining wall at Muros Talca (SW).....	142
Figure 261. Photo. Toppling of coping at Américo Vespucio/Independencia.....	143
Figure 262. Photo. Wall movement near Chepe railroad bridge due to lateral spreading and settlement.....	144
Figure 263. Photo. Wall settlement and rotation due to lateral spreading and settlement.....	144
Figure 264. Map. Retaining walls near Juan Pablo II bridge.....	145
Figure 265. Photo. Wall settlement near Juan Pablo II bridge due to liquefaction-induced settlement.....	145
Figure 266. Map. Vía Elevada 21 de Mayo.....	146
Figure 267. Photo. Tiered wall corner tilting outward at wall site 28A.....	147
Figure 268. Photo. Wall corner tilting outward at wall site 28B.....	148
Figure 269. Photo. Lateral movement of lower wall top at wall site 28C.....	149
Figure 270. Photo. Back side of upper wall at wall site 28C.....	149
Figure 271. Photo. Fill material from tiered wall at wall site 28C.....	150
Figure 272. Photo. Differential settlement at wall site 28C.....	150
Figure 273. Photo. Possible liquefaction features near wall site 28C.....	151

Figure 274. Illustration. Plan view of wall at Muros Talca	152
Figure 275. Photo. Wall with steep top slope at Muros Talca.....	152
Figure 276. Photo. Wall with cracked block pattern at Muros Talca	153
Figure 277. Photo. Bridge supported on footing on top of block-faced geogrid wall at Estribo Francisco Mostazal.....	153
Figure 278. Illustration. Notations on skew direction.....	155
Figure 279. Illustration. Deck rotation of a representative bridge (two spans shown).....	156
Figure 280. Illustration. Rotational and translational mode responses to ground motions.....	157
Figure 281. Photo. Exterior girder damage at Chada bridge, no diaphragms.....	158
Figure 282. Photo. Exterior girder damage at San Nicolás bridge, partial diaphragms	159
Figure 283. Photo. Exterior girder damage at west abutment of Llacolen bridge, concrete teeth...	159
Figure 284. Map. Image of site 1 taken prior to earthquake.....	169
Figure 285. Illustration. Boring log at site 1	169
Figure 286. Map. Image of site 2 taken prior to earthquake and showing approximate location of test hole.....	170
Figure 287. Illustration. As-built bridge plan for site 2	170
Figure 288. Illustration. As-built bridge profile for site 2 showing footing foundations	171
Figure 289. Illustration. Boring log at site 2.....	171
Figure 290. Map. Image of site 7 taken prior to earthquake and showing approximate location of test hole.....	172
Figure 291. Illustration. As-built bridge plan for site 7	172
Figure 292. Illustration. Boring log for site 7	173
Figure 293 Map. Image of site 8 taken prior to earthquake and showing approximate location of test hole.....	173
Figure 294. Illustration. As-built bridge plan for site 8.....	174
Figure 295. Illustration. Boring log for site 8.....	175
Figure 296. Map. Image of site 10 taken prior to earthquake and showing approximate location of test hole.....	176
Figure 297. Illustration. As-built bridge plan for site 10.....	176
Figure 298. Illustration. Boring log SA-2 for site 10.....	177
Figure 299. Map. Image of site 28 taken prior to earthquake and showing approximate locations of test holes.....	177
Figure 300. Illustration. Boring log S-1 for site 28.....	178
Figure 301. Illustration. Detailed standard penetration test blow counts for boring log S-1 for site 28	179
Figure 302. Illustration. Boring log S-2 for site 28.....	180
Figure 303. Illustration. Detailed standard penetration test blow counts for boring log S-2 for site 28	181
Figure 304. Illustration. Boring log S-3 for site 28.....	182
Figure 305. Illustration. Detailed standard penetration test blow counts for boring log S-3 for site 28	183

LIST OF TABLES

Table 1. Specific sites' structural names and GPS locations	3
Table 2. Summary of available earthquake records for the offshore Maule earthquake	11
Table 3. Number of damaged bridges.....	23
Table 4. Bridges visited by reconnaissance team	24
Table 5. Summary of performance for abutments and interior piers on slopes affected by liquefaction-induced ground movement or settlement	134
Table 6. Summary of sites with retaining walls.....	139
Table 7. Summary of bridges and bridge damage	155
Table 8. Seismic zones.....	185
Table 9. Soil coefficients	185
Table 10. Seismic behavior categories.....	186
Table 11. Importance factor, K_I	187
Table 12. Spectral constants, T_I and K_2	187
Table 13. Approximate formulas for natural periods for bridges	188
Table 14. Response modification factors (R).....	190

LIST OF ACRONYMS

AASHTO	American Association of State and Highway Transportation Officials
CIP	Cast-in-place
DDC	Deep dynamic compaction
EERI	Earthquake Engineering Research Institute
FHWA	Federal Highway Administration
GEER	Geotechnical Extreme Events Reconnaissance
GPS	Global Positioning System
LRFD	Load and resistance factor design
MOP	Ministry of Public Works
MSE	Mechanically stabilized earth
NEHRP	National Earthquake Hazards Reduction Program
PGA	Peak ground acceleration
QDR	Quake data recorder
TIRT	Transportation infrastructure reconnaissance team
USGS	United States Geological Survey

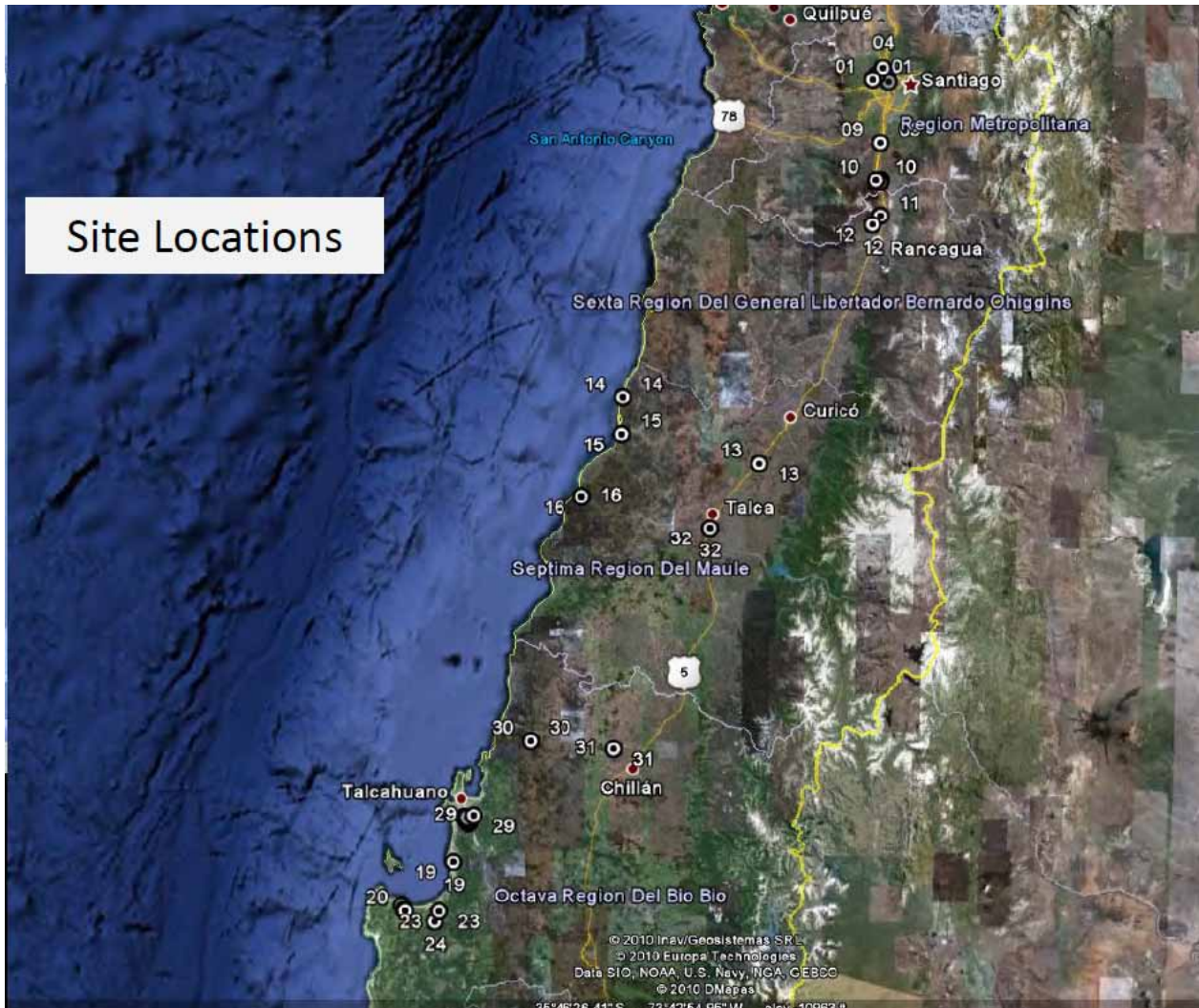
CHAPTER 1. INTRODUCTION

1.1 BACKGROUND

Over the course of the last century, Chile has experienced several strong earthquakes. According to the United States Geological Survey (USGS), M8.2 earthquakes struck the nation in 1906, 1943, and 1960, and an M8.0 earthquake hit in 1985. The M8.2 earthquake in 1960 was a foreshock that occurred the day before the largest earthquake ever recorded, the M9.5 Chilean earthquake. The offshore Maule earthquake on February 27, 2010, was measured at M8.8 and lasted more than 2 min. It is estimated that this earthquake was approximately 500 times more powerful than the earthquake that devastated Haiti in January 2010. Several aftershocks, including nine events with a magnitude exceeding 6.0, occurred in the days following the Chilean earthquake.⁽¹⁾ The M8.8 event is the fifth largest earthquake recorded in modern times and was characterized by its long duration and strong ground motion, which also caused tsunamis across the region. Many bridges and tunnels constructed with seismic design codes similar to the 1983 U.S. and European codes were damaged in the earthquake.

Because of the size of the event, the intensity of the ground shaking, the geological similarity of the Maule region and the Northwestern United States (e.g., Washington and Oregon's subduction zones), and the comparable nature of the infrastructure construction and seismic design codes used, the performance of transportation infrastructure during this earthquake provided valuable lessons in earthquake engineering. In March 2010, the Federal Highway Administration (FHWA) contacted Chile's Ministry of Public Works (MOP) and worked with University Transportation Center, Washington State Department of Transportation, University of Nevada, and Missouri University of Science and Technology to organize the transportation infrastructure reconnaissance team (TIRT). TIRT and a member of the Earthquake Engineering Research Institute (EERI) were dispatched to Chile on April 3 to perform a comprehensive earthquake reconnaissance. TIRT was supported by local bridge engineers from MOP and local researchers from Pontifical Catholic University of Chile and the University of Chile.

TIRT visited more than 32 transportation infrastructure sites, including highway bridges and port facilities from Santiago down to Tubul, a small city near Concepción. The specific locations visited are shown in figure 1 and listed in table 1 with site names, Global Positioning System (GPS) coordinates, and city and county names.



© Google, Inav/Geosistemas SRL, Europa Technologies, and DMaps
Figure 1. Map. Site locations visited by TIRT.

Table 1. Specific sites' structural names and GPS locations.

Site No.	Site Name	Location	Latitude (S) (degrees)	Longitude (W) (degrees)
1a	Américo Vespucio/Miraflores eastbound	Santiago	-33.39	-70.77
1b	Américo Vespucio/Miraflores westbound			
2a	Américo Vespucio/Lo Echevers eastbound	Santiago	-33.38	-70.75
2b	Américo Vespucio/Lo Echevers westbound			
3	I-5/14 de la Fama	Santiago	-33.40	-70.68
4	Pedestrian bridge over Route 5	Santiago	-33.34	-70.71
5	Quilicura railway crossing at Avenida Manuel Antonio Matta	Santiago	-33.37	-70.70
6a	Américo Vespucio/Independencia westbound	Santiago	-33.37	-70.69
6b	Américo Vespucio/Independencia eastbound			
6c	Américo Vespucio/Independencia westbound exit ramp			
6d	Américo Vespucio/Independencia westbound entrance ramp			
7	Avenida Romero Acceso Sur overpass	Paine	-33.86	-70.72
8	Avenida Chada Acceso Sur overpass	Paine	-33.87	-70.73
9a	Maipú River (local access bridge)	Buin	-33.69	-70.72
9b	Maipú River (current Route 5 bridge)			
9c	Maipú railroad crossing			
10a	Route 5 railway crossing at Hospital westbound	Buin	-33.86	-70.75
10b	Route 5 railway crossing at Hospital eastbound			
11	Estribo Francisco Mostazal (Avenida Independencia)	Mostazal	-34.03	-70.72
12	Las Mercedes Route 5 overpass	Rancagua	-34.07	-70.76
13a	Claro River	San Rafael	-35.18	-71.39
13b	Claro River			
14	Pichibudis	Iloca	-34.88	-72.16
15	Mataquito	Iloca	-35.05	-72.16
16	Cardenal Raúl Silva Henríquez	Constitución	-35.34	-72.39
17	Llacolen	Concepción	-36.83	-73.07
18	Chepe railroad bridge over Biobío River	Concepción	-36.82	-73.07
19a	Puerto de Coronel Muelle Norte	Coronel	-37.03	-73.15
19b	Puerto de Coronel Muelle Sur			
20	Raqui 1	Raqui	-37.25	-73.44
21	Raqui 2	Raqui	-37.25	-73.44

Table 1. Specific sites' structural names and GPS locations—Continued.

Site No.	Site Name	Location	Latitude (S) (degrees)	Longitude (W) (degrees)
22	Tubul	Raqui	-37.23	-73.46
23	El Bar	Arauco	-37.26	-73.24
24a	Ramadillas (west, old)	Arauco	-37.31	-73.26
24b	Ramadillas (east, new)			
25	Juan Pablo II	Concepción	-36.82	-73.09
26	Biobío River (old)	Concepción	-36.84	-73.06
27	La Mochita	Concepción	-36.85	-73.06
28	Vía Elevada 21 de Mayo/Cruce Ferroviario	Concepción	-36.82	-73.07
29	Rotonda General Bonilla	Concepción	-36.81	-73.03
30	Itata River	Coelemu	-36.47	-72.69
31	San Nicolás	San Nicolás	-36.50	-72.21
32	Muros Talca (SW)	Talca	-35.48	-71.67

1.2 THE TRANSPORTATION INFRASTRUCTURE RECONNAISSANCE TEAM

1.2.1 Objective

TIRT's mission was to conduct a thorough postearthquake investigation concentrating on highway bridges, tunnels, and retaining walls in the areas affected by the earthquake, including the cities of Concepción and Santiago. Performance of these structures, including damaged and undamaged conditions, were carefully documented and analyzed. The information gathered from this effort will be studied, and the results will be used to assess, refine, and improve current design codes and standards that benefit the United States, Chile, and the general engineering community.

1.2.2 Team Members

TIRT included six members led by the FHWA Office of Infrastructure Research and Development, including three FHWA representatives, one representative of the American Association of State and Highway Transportation Officials (AASHTO), and two university representatives. Juan G. Arias, a student representing EERI, joined and assisted the team in the investigation. The team was coordinated by FHWA's Sheila Duwadi throughout the preparation, reconnaissance, and postreconnaissance reporting. The U.S. team members were fully supported by their Chilean colleagues. Figure 2 shows the team members and local participants. Pictured from left to right are Daniel Alzamora (FHWA Resource Center), Dr. Ian Buckle (University of Nevada), Dr. Phillip W. Yen (FHWA team leader), Genda Chen (Missouri University of Science and Technology), Juan G. Arias (University of Nevada), Rodrigo Oviedo (Pontifical Catholic University of Chile), Dr. Jeffrey Ger (FHWA Florida Division), Tony Allen (Washington State Department of Transportation), Sandra Achurra (MOP), and Mauricio Guzman (MOP).



Figure 2. Photo. TIRT team members and Chilean support personnel.

1.3 REPORT ORGANIZATION

This report presents the preliminary reconnaissance findings of the earthquake performance of transportation infrastructure based on available information, visual observations, and preliminary analysis. Chapter 2 describes the seismic details of the earthquake. Chapter 3 presents a summary of Chilean seismic design codes studied by TIRT, and chapter 4 provides the findings of the investigation of structural performance. Chapter 5 documents the geotechnical observations of infrastructure performance, including bridges, retaining walls, and other structures. Chapter 6 presents the lessons learned from this reconnaissance, and chapter 7 offers conclusions and recommendations.

CHAPTER 2. GEOLOGY, SEISMOLOGY, AND GROUND MOTIONS

2.1 BACKGROUND

The USGS Web site and a report provided by the Geotechnical Extreme Events Reconnaissance (GEER) team were used to provide necessary background information regarding the seismic and geologic setting for the sites specifically investigated by TIRT.^(1,2) Additional information not available at the time of the USGS posting and the GEER report (e.g., boring logs, ground motion data, etc.) is also included in this chapter.

2.2 GEOLOGY AND SEISMOLOGY

The offshore Maule earthquake occurred on February 27, 2010, at 3:34 a.m. (local time) at the boundary between the Nazca and South American tectonic plates.⁽¹⁾ The location of the earthquake's epicenter is shown in figure 3 relative to the sites investigated by TIRT, shown as white dots with black centers and white numbers. The earthquake epicenter, located at 35.909 °S, 72.733 °W, was approximately 208 mi (335 km) southwest of Santiago, 65.2 mi (105 km) northeast of Concepción, and 71.4 mi (115 km) west-southwest of Talca. The depth of the earthquake hypocenter was 22 mi (35 km).



Figure 3. Map. Location of epicenter, seismic recording stations, and TIRT sites.

Chile has a long history of severe earthquakes along its approximately 1,860-mi (3,000-km) coastline. Since the beginning of the 20th century, five earthquakes of M8.0 or higher have been recorded in Chile: M8.2 in 1906, M8.2 in 1943, M8.0 in 1985, and an M8.2 foreshock that preceded an M9.5 earthquake in 1960. Since 1973, there have been 13 events of M7.0 or greater.

The February 27, 2010, earthquake originated about 140 mi (230 km) north of the source region (the point of initial rupture) of the M9.5 earthquake of 1960, the largest instrumentally recorded earthquake in the world. The 2010 earthquake was approximately 190 mi (300 km) south of the source region of the M8.2 earthquake of 1906 and approximately 540 mi (870 km) south of the source region of the M8.5 earthquake of 1922.

Figure 4 shows the spatial relationship between previous earthquakes (M6.5 or greater, 1900–1963 and M5.5 or greater, 1964–present) and the 2010 M8.8 offshore Maule earthquake (depicted by a yellow star) and its associated aftershocks (depicted by yellow circles). The points of initial rupture for the M8 or larger earthquakes are denoted by red circles with thick black borders. The estimated rupture zones of the 1922 M8.5 and 1960 M9.5 earthquakes are marked in white. These rupture zones were defined by the areal extent of aftershocks or by geological and macroseismic observations. The 2010 M8.8 earthquake ruptured the portion of the South American subduction zone between these massive historical earthquakes, with the 1906 and 1922 megaquakes to the north and the 1960 megaquake to the south. The offshore Maule earthquake rupture zone was over 370 mi (600 km) long and 81 mi (130 km) wide. The last time this portion of the subduction zone ruptured may have been the 1835 event experienced by Charles Darwin.

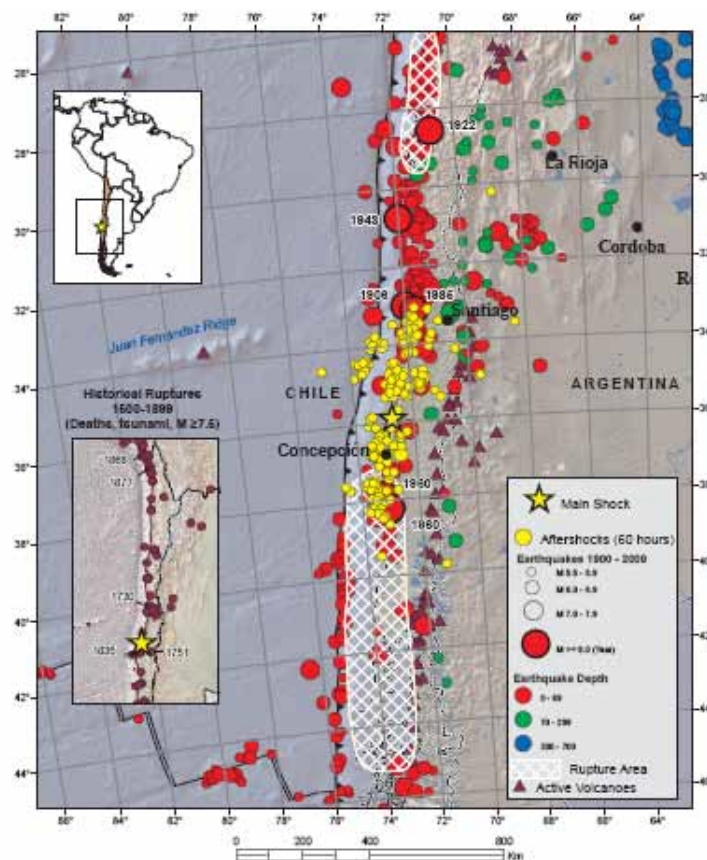


Figure 4. Map. Historic seismicity for Chile.⁽¹⁾

The 2010 offshore Maule earthquake occurred as thrust faulting on the interface between two plates, with the Nazca plate moving down and landward below the South American plate. The slip rate between the two plates is estimated to be approximately 2.7 inches/year (70 mm/year).⁽³⁾ This rate is much higher than the slip rate for the Cascadia subduction zone located along coastal Washington and Oregon (approximately 1.4 inches/year (35 mm/year)), which explains the more frequent occurrence of this type of event along the Chilean coastline.⁽⁴⁾ Ruegg et al. estimated that at least 33 ft (10 m) of slip deficit had accrued on this segment of the plate boundary since the last time this portion of the subduction zone ruptured in 1835.⁽³⁾ GPS measurements indicate that the actual horizontal movement of the overriding plate was as much as 12 ft (3.7 m) to the southwest at Concepción, 15 ft (4.7 m) at Constitución, and approximately 2 ft (0.5 m) at Santiago.

This type of earthquake is illustrated conceptually in figure 5. Overall, a tectonic plate descends, or “subducts,” beneath an adjoining plate in a stick-slip fashion. Between earthquakes, the plates slide freely at great depth, but at shallow depth, they stick together. A key aspect of this type of earthquake is the buildup of stress at the stuck portion of the boundary. As the upper plate attempts to override the lower plate, it deforms and is uplifted until the stress is too great. At that point, the stuck portion of the boundary catastrophically ruptures, allowing the front portion of the upper plate to spring seaward and upward while the rest of the upper plate relaxes, causing subsidence. Field observations reported by GEER indicate that the coastline from the vicinity of the epicenter south to the Arauco peninsula experienced uplift up to approximately 7 ft (2 m), whereas areas north of Constitución to Bucalemu experienced subsidence of up to about 3 ft (1 m).⁽²⁾ Observations made by TIRT at the sites investigated appear to confirm these findings. This type of coseismic deformation has historically been accompanied by the generation of tsunamis. For the offshore Maule earthquake, a tsunami that severely impacted the coast north of the epicenter was produced. As the area to the north of the epicenter also experienced significant coseismic subsidence, tsunami run-up was increased, resulting in greater onshore damage.

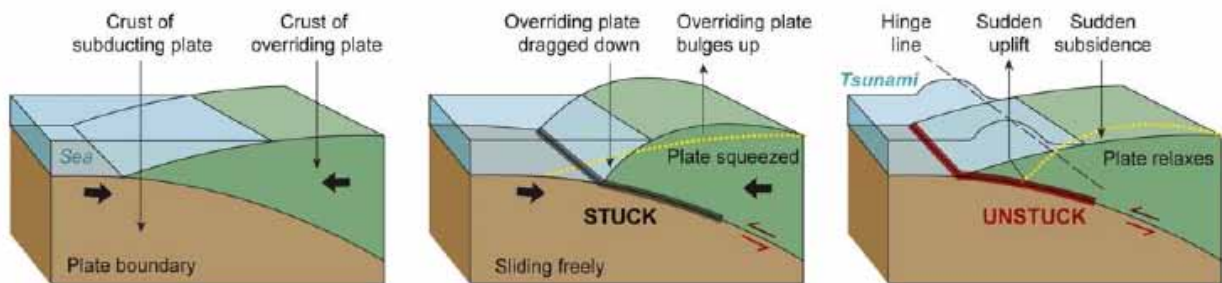
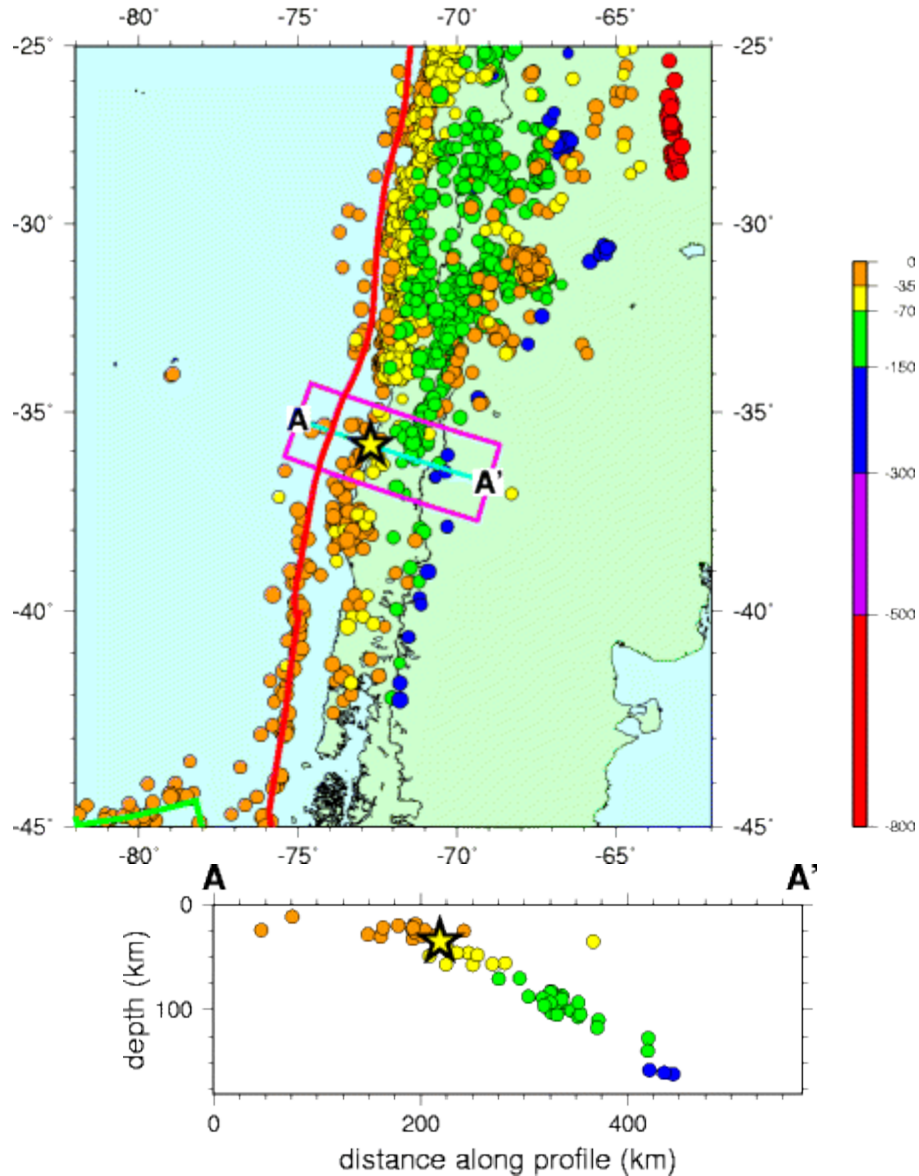


Figure 5. Illustration. Conceptual diagram of a subduction zone earthquake.^(2,4)

Another key aspect of this type of earthquake is the tendency of such an event to produce many strong aftershocks as the plates adjust to the sudden change in stresses following rupture. The aftershocks themselves can produce a significant hazard to the structures and facilities damaged by the main shock, as well as to the people within or near the partially damaged structures. Figure 4 and figure 6 show maps illustrating the number and distribution of aftershocks, some of which approached M7.0. The cross section of the aftershock locations as a function of depth and distance in figure 6 illustrates the location of the rupture surface. The hypocenter of the main shock is marked with a star.



1 km = 0.621 mi

Figure 6. Illustration. Offshore Maule earthquake aftershock distribution with depth.⁽⁵⁾

2.3 GROUND MOTIONS

The actual ground motions experienced at a particular site depend on the soil type and density present, as well as the three-dimensional aspects of the local geologic structure beneath and around the site. In general, as soils become softer or looser, the ground motions tend to increase, especially at longer periods. Basin effects can also amplify ground motions at a particular site. As the team traveled throughout the region impacted by the earthquake, it was apparent that damage to transportation and other structures was concentrated in specific areas, with areas in between showing little or no damage. GEER reported similar observations and attributed the difference to the presence of softer silts and clays at the affected sites and, in some cases, to basin effects.⁽²⁾

At the time of this report, the available ground motion data from the offshore Maule earthquake was limited, and ground motion records were only available from some of the stations identified in figure 3, shown as small rectangles with blue accelerograms. White icons denote stations where no accelerogram was available. Yellow icons denote stations where an accelerogram was available but digital records of the ground motion were not available. Pink icons (only one, in Concepción) denote stations where digital records of the ground motion were available.

The available records, summarized in table 2, are uncorrected and may be influenced by the structures in which the measurements were taken. The ground motion records are from two different sources, Boroschek, et al. and the University of Chile Department of Geophysics.^(6,7) Boroschek, et al. indicated that all ground motion monitoring equipment was in one-story structures, but in some cases, other types of structures were nearby.⁽⁶⁾ All of these records require careful evaluation due to potential soil-structure interaction effects.^(6,7) Specifically, Boroschek, et al. noted that the high accelerations at the Maipú site were being reviewed for soil-structure interaction effects. Soil classifications at each of these monitoring sites were being investigated at the time of this report.⁽⁶⁾ Boroschek, et al. also cautioned that the quake data recorder (QDR) only recorded the first 100 s of motion.⁽⁶⁾ However, the motion actually lasted about 140 s. Therefore, the last 40 s of motion is missing from these records. QDR equipment was used for all of the ground motion records in table 2, except Universidad de Chile Departamento de Ingeniería Civil (interior building); Estación Metro Mirador, Santiago; and Colegio San Pedro, Concepción. Examples of these ground motions and their respective response spectra (where available) are provided in figure 7 through figure 14.

Table 2. Summary of available earthquake records for the offshore Maule earthquake.⁽⁶⁾

Location of Monitoring Station	Source of Information	Maximum Horizontal Acceleration (g)	Maximum Vertical Acceleration (g)
Universidad de Chile, Depto. Ing. Civil (interior building)	RENADIC ⁽⁶⁾	0.17	0.14
Estacion Metro Mirador, Santiago	RENADIC ⁽⁶⁾	0.24	0.13
CRS Maipú RM	RENADIC ⁽⁶⁾	0.56	0.24
Hospital de Tisné RM	RENADIC ⁽⁶⁾	0.30	0.28
Hospital Sótero de Río RM	RENADIC ⁽⁶⁾	0.27	0.13
Hospital de Curicó	RENADIC ⁽⁶⁾	0.47	0.20
Hospital de Valdivia	RENADIC ⁽⁶⁾	0.14	0.05
Vina del Mar, Marga Marga	RENADIC ⁽⁶⁾	0.35	0.26
Vina del Mar (Centro)	RENADIC ⁽⁶⁾	0.33	0.19
Colegio San Pedro, Concepción	Red Sismológica Nacional	0.65 NS, 0.58 EW	0.60
San Pedro de la Paz, Colegio Concepción	USGS ⁽⁸⁾	0.65 NS, 0.61 EW	0.58

NS = North-south.

EW = East-west.

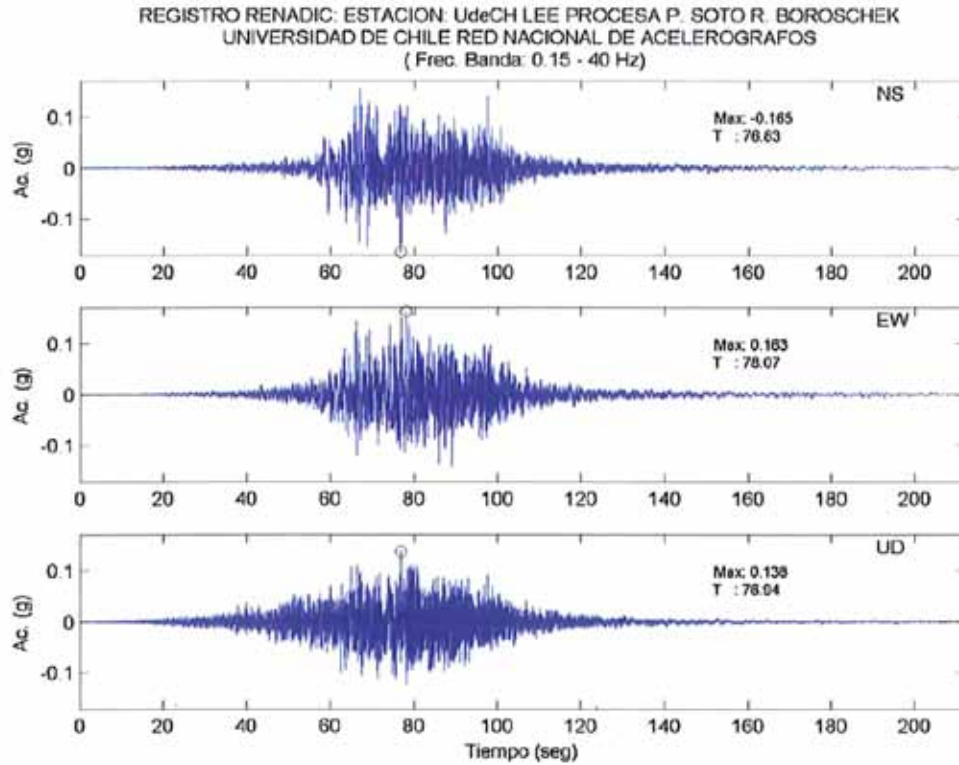


Figure 7. Illustration. Accelerogram from Universidad de Chile, Depto. Ing. Civil (interior building).⁽⁶⁾

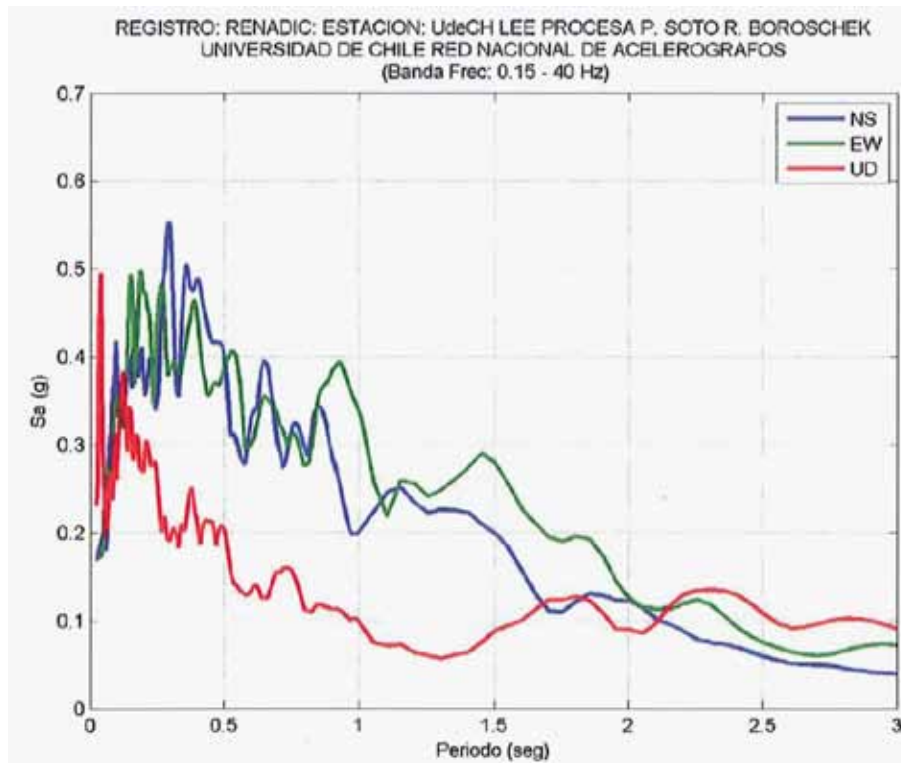


Figure 8. Illustration. Response spectra from Universidad de Chile, Depto. Ing. Civil (interior building).⁽⁶⁾

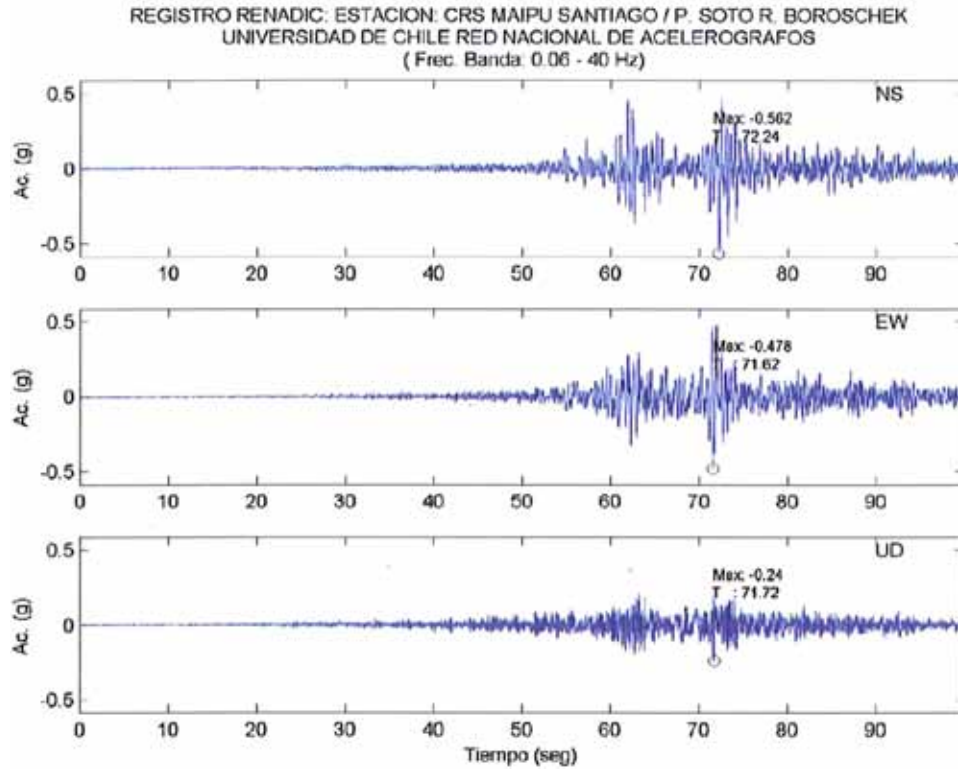


Figure 9. Illustration. Accelerogram from CRS Maipú RM.⁽⁶⁾

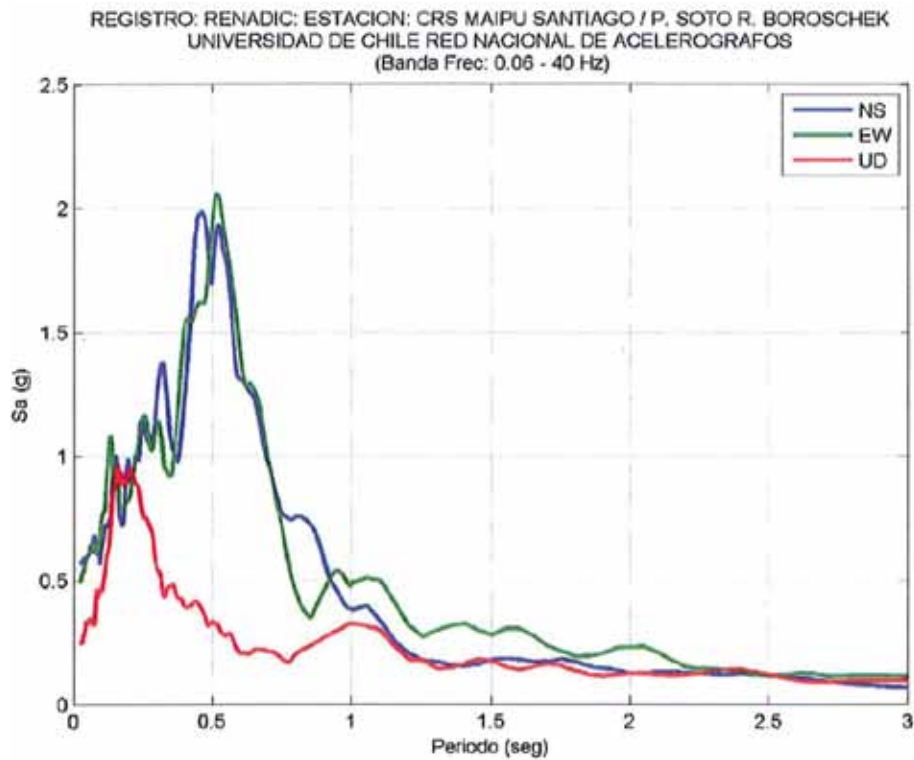


Figure 10. Illustration. Response spectra from CRS Maipú RM.⁽⁶⁾

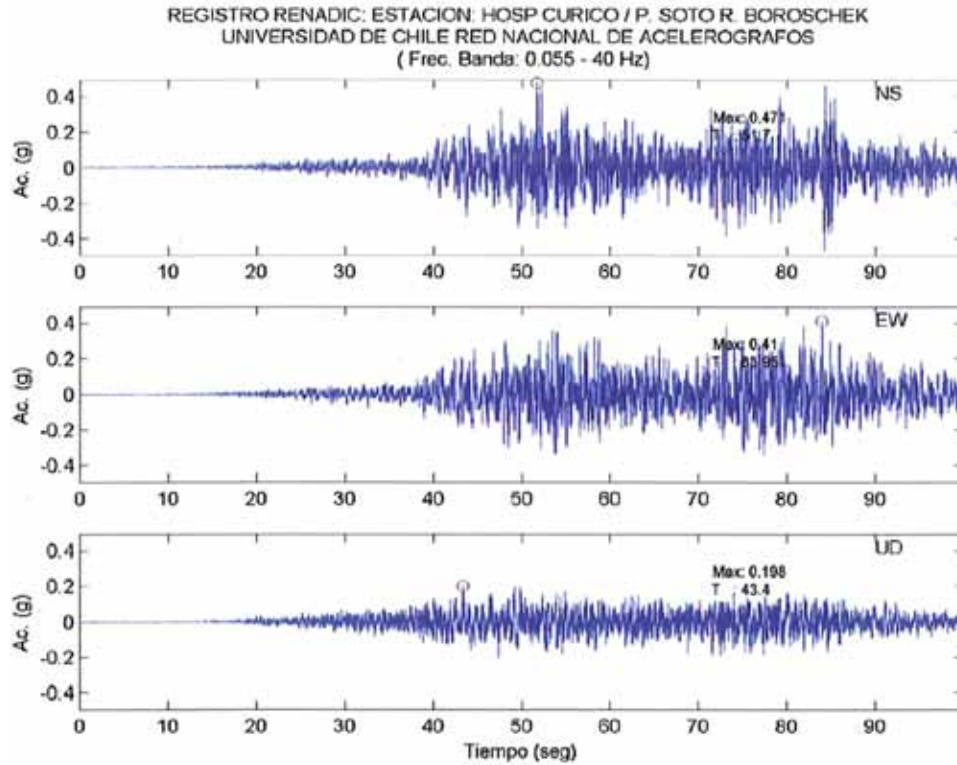


Figure 11. Illustration. Accelerogram from Hospital de Curicó.⁽⁶⁾

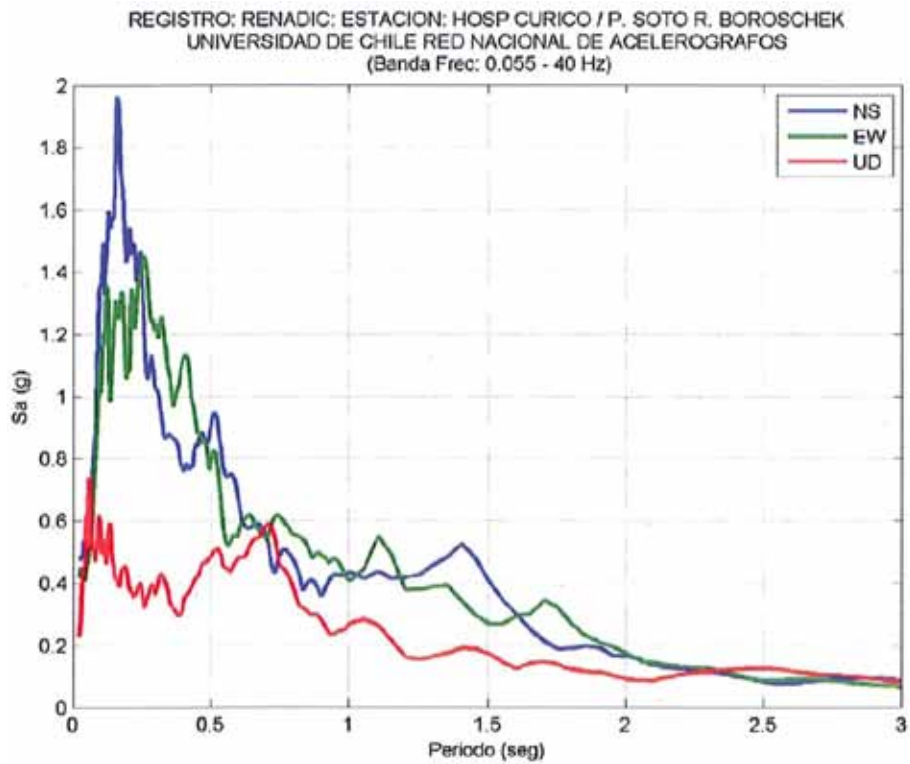


Figure 12. Illustration. Response spectra from Hospital de Curicó.⁽⁶⁾

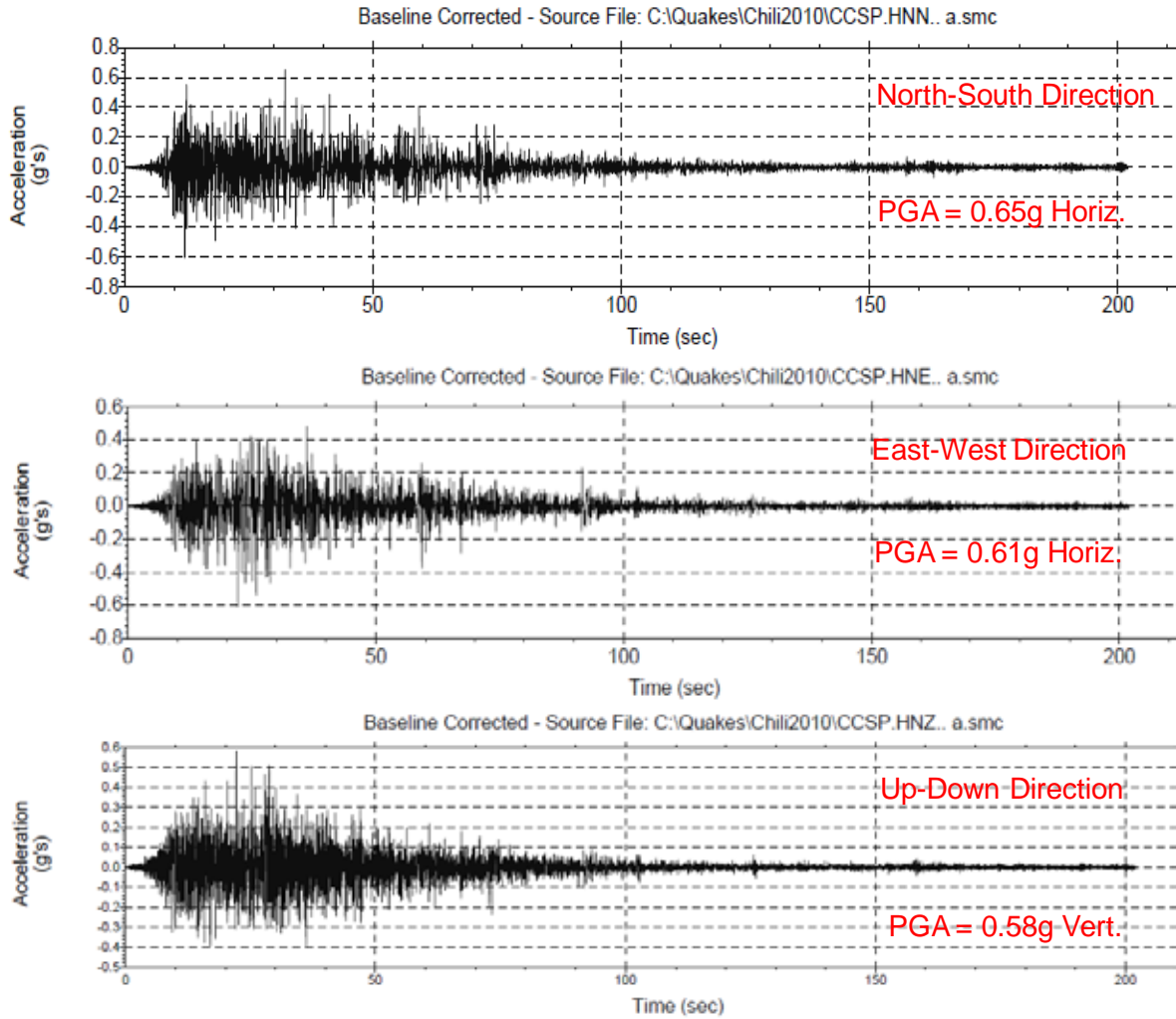


Figure 13. Illustration. Accelerogram from San Pedro De La Paz, Colegio Concepción.⁽⁸⁾

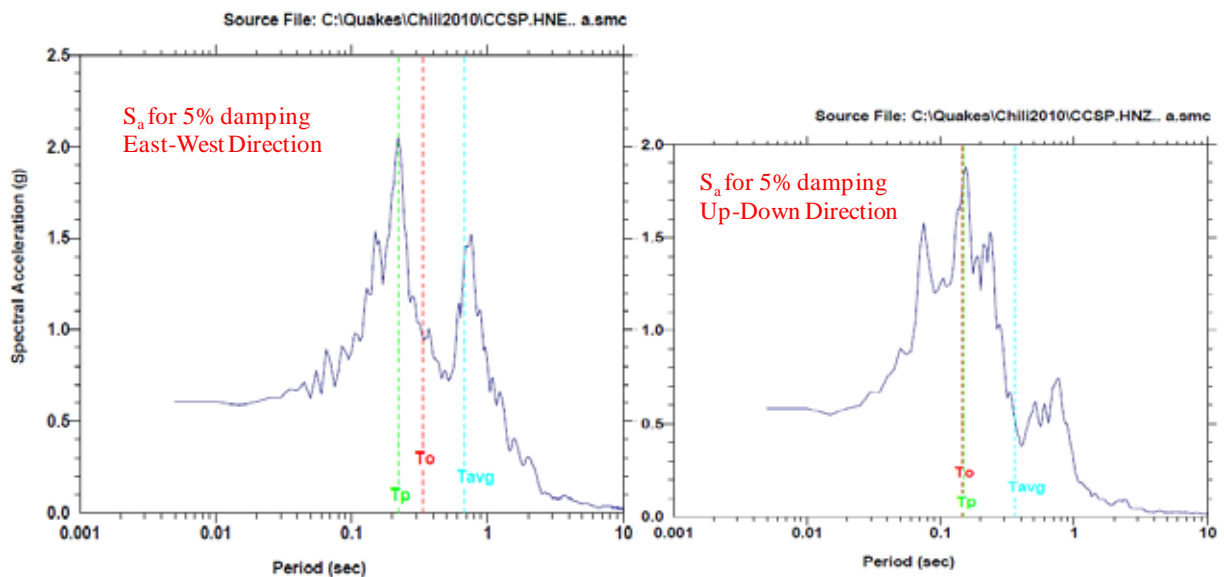


Figure 14. Illustration. Response spectra from San Pedro De La Paz, Colegio Concepción.⁽⁸⁾

Figure 13 is the only time history for which a digital file was available at the time of this report. For the east-west direction in that time history, the bracketed duration (i.e., $A > 0.05$ g) was 152 s and the duration of significant shaking based on normalized Arias intensity was approximately 76 s. Visually and in terms of peak values, this ground motion record is very similar to the one obtained at Colegio San Pedro. Figure 15 through figure 19 are maps marked with accelerograms and TIRT structure sites to show the location of the ground motion recording stations relative to the structure sites visited. The symbols used in figure 3 are also used in these figures. See chapter 1 and chapter 3 for a more detailed description of each structure site.

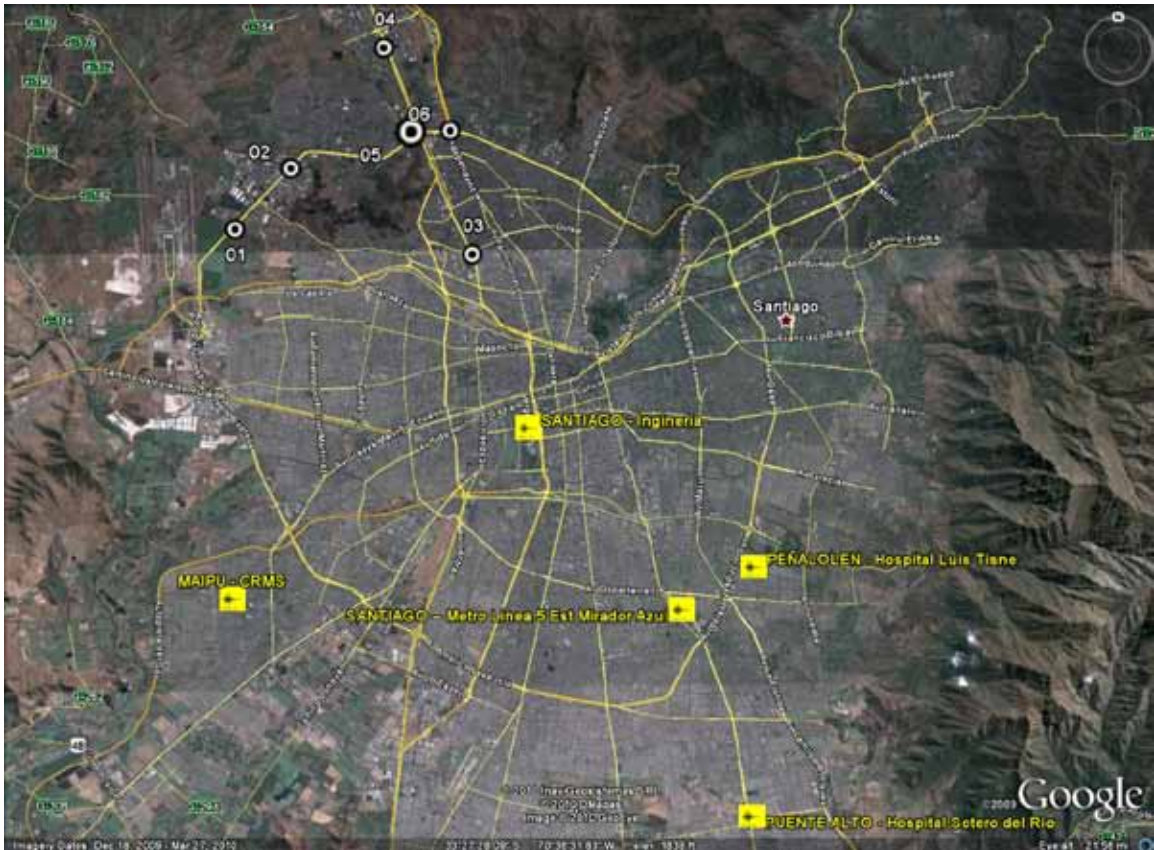


Figure 15. Map. Locations of ground motion sensors and structures visited by TIRT—Santiago vicinity.



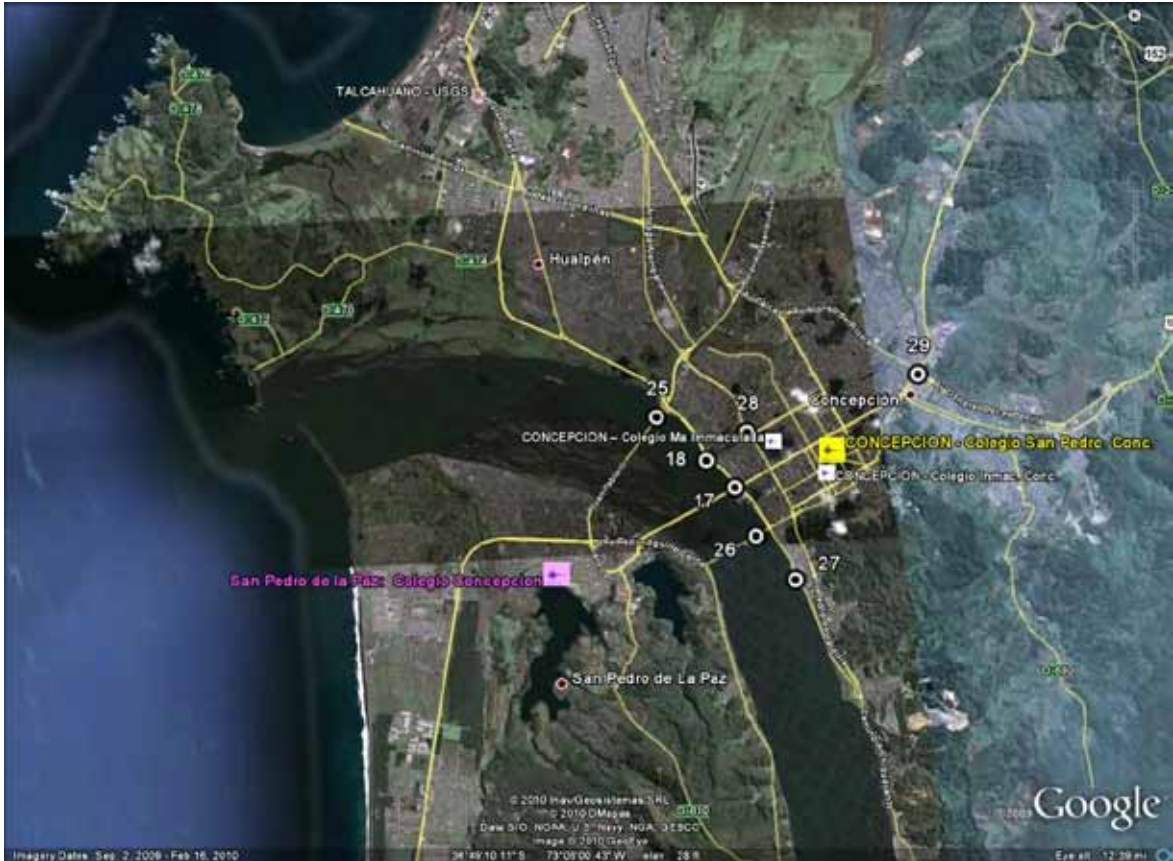
© Google, Inav/Geosistemas SRL, DMapas, GeoEye, and DigitalGlobe

**Figure 16. Map. Locations of ground motion sensors and structure visited by TIRT—
Santiago to Rancagua.**



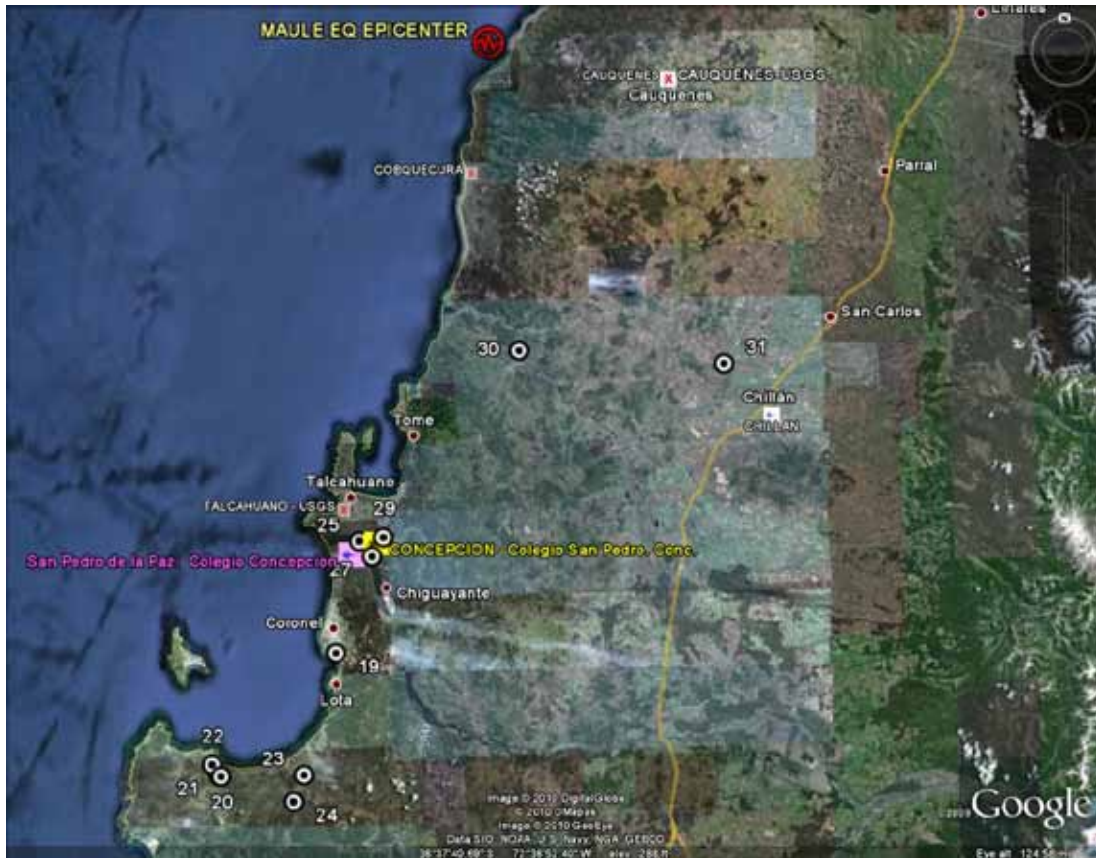
© Google, Cnes/Spot Image, DMapas, GeoEye, and DigitalGlobe

Figure 17. Map. Locations of ground motion sensors and structures visited by TIRT—Curicó, Talca, Iloca vicinity.



© Google, Inav/Geosistemas SRL, DMapas, and GeoEye

**Figure 18. Map. Locations of ground motion sensors and structures visited by TIRT—
Concepción vicinity.**



© Google, DigitalGlobe, DMaps, and GeoEye

Figure 19. Map. Locations of ground motion sensors and structures visited by TIRT—Maule epicenter to Tubul vicinity.

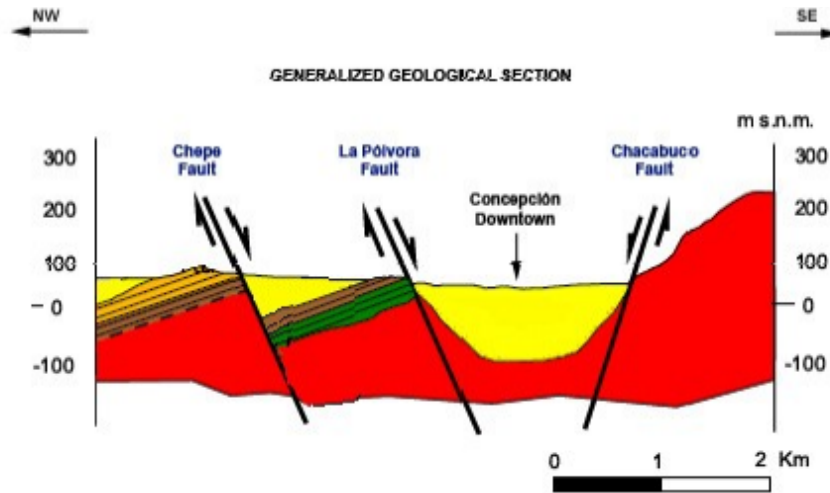
GEER provided geologic information that can be used in combination with the subsurface information gathered by TIRT to preliminarily assess the potential effect subsurface conditions may have had on ground motion severity.⁽²⁾ The subsurface information gathered by TIRT is reported in appendix A. For example, the GEER report indicates that relatively soft silts and clays and, in some cases, ash deposits are likely to be encountered in the western sector of Santiago, where structure sites 1–6 are located.⁽²⁾ A boring log obtained for the original bridge design at sites 1 and 2 indicates that subsurface soils there consist of 16 ft (5 m) of soft to medium stiff clay underlain by more than 33 ft (10 m) of stiff to very stiff silty clay with layers of fine sand. Based on the AASHTO and National Earthquake Hazards Reduction Program (NEHRP) seismic site classification systems, these soils would likely be classified as Site Class E soils, and significant ground motion amplification would be expected. The eastern sector of Santiago, where most of the available earthquake ground motion measurements were taken, generally consists of sands and gravels. It could therefore be expected that, in general, ground motion measurements in the eastern sector of Santiago should be less severe than those obtained in the western sector because of better soil conditions in addition to being farther away from the earthquake epicenter. A comparison of the ground motions in figure 7 with those in figure 9 appears to support this conclusion—the peak accelerations in figure 7 (0.17 g) are considerably less than those in figure 9 (0.56 g). The other ground motion records obtained in the eastern sector of Santiago range from 0.24 g to 0.30 g, still considerably lower than the peak measured at CRS Maipú RM (see figure 9). The response

spectra also seem to indicate the potential effect of softer soils in that the peak spectral acceleration is pushed out to longer periods and the spectral acceleration magnitude is two to four times higher than that of the eastern sites. Based on the location of the first six sites, a reasonable preliminary conclusion is that the acceleration time history and response spectra for CRS Maipú RM, shown in figure 9 and figure 10, are most representative of the ground motions that occurred at the first six bridge sites. Once subsurface geotechnical data for these earthquake ground motion monitoring sites becomes available and the soil-structure interaction effect is fully investigated, these preliminary conclusions can be confirmed.

The next set of structure sites, sites 7–10, are probably on the margin of the poorer soil conditions based on the geologic data published by GEER.⁽²⁾ However, some geotechnical boring information is available at sites 7, 8, and 10 indicating the presence of at least 33 to 49 ft (10 to 15 m) of medium to stiff silty clays or sandy silts, with stiff to hard silts and clays and some dense sand or gravel layers at depth (see appendix A). Based on the AASHTO and NEHRP classification systems, these soils would likely be classified as Site Class D or E soils, and significant ground motion amplification would be expected. Again, the CRS Maipú RM ground motions (shown in figure 9 and figure 10) appear to be the most applicable to these structure sites with due consideration given to the cautionary issues previously discussed.

Sites 11–13 and 32 are far enough away from Santiago that closer ground motion records should be used. The only ground motion record available in this area is the one at Curicó (see figure 11 and figure 12). The GEER report does not provide specific geologic information, but deposits at Talca (south of Curicó) are likely to be alluvial and marine sediments and are probably highly variable.⁽²⁾ Therefore, the strength of the ground motions in this region is likely to be highly variable, as indicated by the inconsistent damage to structures and facilities.

South of Talca and closer to the coast, the ground motion records in the interior may not be representative of the ground motions experienced, considering proximity to the epicenter and subsurface conditions present. Fortunately, two ground motion records are available in Concepción (see figure 13). According to GEER, Concepción has both poor soils (loose alluvial and marine deposits) and a geologic structure, due to major faults running through the area, that could contribute to amplification of ground motion (see figure 20 and figure 21).⁽²⁾ Damage due to the offshore Maule earthquake was particularly severe in Concepción. The spatial distribution of the damage is apparently similar to the damage seen during the 1960 M9.5 event, trending along parallel linear zones. This similarity shows the effect geologic basin structure and soil deposits may have had on the ground motions. The location of the Colegio San Pedro monitoring station is shown in figure 21. This monitoring station is located in between two significantly damaged areas. Therefore, it is not clear if the Colegio San Pedro ground motion record, which is similar to the San Pedro de la Paz record provided in figure 13, represents the most damaged areas. Considering the high peak acceleration of 0.65 g in the horizontal direction and 0.60 g in the vertical direction, the long duration, and the similarity to the San Pedro de la Paz ground motion, a reasonable preliminary conclusion is that these two ground motion records are representative of what occurred in the significantly damaged areas. While it is unknown if there are any geologic basin issues for the sites farther south (e.g., sites near Tubul), the soil conditions are obviously poor and probably similar to conditions in parts of Concepción (see chapter 5). Therefore, this ground motion should be considered applicable to sites 17–29.



1 km = 0.621 mi

Figure 20. Illustration. Geologic cross section of Concepción.⁽²⁾

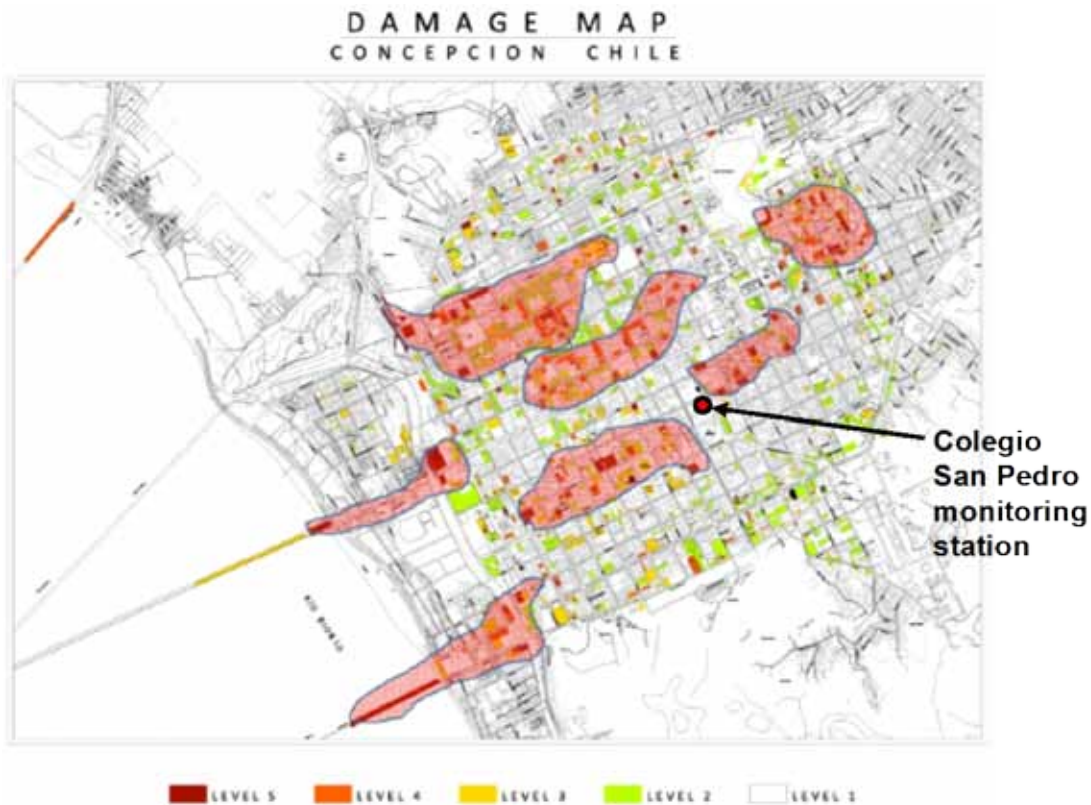


Figure 21. Map. Damaged sections in downtown Concepción.⁽²⁾

Not much information is available on the subsurface conditions of sites 15, 16, and 30–32, and there are no nearby ground motion records for those locations. Until more is known, a compromise between the Curicó and Concepción ground motions could be used for preliminary analyses.

Once more ground motion records and geotechnical subsurface data are available to confirm these conclusions (based primarily on geologic mapping), the ground motions most applicable to each structure site can be better assessed.

CHAPTER 3. OVERVIEW OF BRIDGE PERFORMANCE AND SEISMIC DESIGN REQUIREMENTS IN CHILE

3.1 OVERVIEW OF BRIDGE PERFORMANCE

3.1.1 Damage Statistics

Of the nearly 12,000 bridges in Chile, about 200 were damaged in the offshore Maule earthquake, including 20 structures with one or more collapsed spans. These 12,000 bridges include about 4,750 culverts and pedestrian overcrossings and 7,250 highway bridges. Of the highway bridges, 6,800 are publicly owned by MOP and 450 are owned by private companies called concessions, which have designed and constructed several major toll roads in Chile. Table 3 shows some damage statistics.

Table 3. Number of damaged bridges.

Owner	Number of bridges¹	Number of damaged bridges²	Number of collapsed bridges³
MOP	6,800	103	10
Concessions	450	100	8
Total	7,250	203	18

¹ Excluding culverts and pedestrian overcrossings.

² Including bridges with collapsed spans.

³ Bridges with one or more collapsed spans.

3.1.2 Bridges Visited By Reconnaissance Team

As noted in chapter 1, TIRT visited 41 damaged bridges at 32 sites in Chile from Santiago to Arauco over a 9-day period from April 4 to 13, 2010. Table 4 provides a summary of the bridges visited along with brief notes about the observed damage. The locations of these sites are shown in figure 1 and figure 3.

Table 4. Bridges visited by reconnaissance team.

Site No.	Site Name	Location	Year Built	Structure Description		
				Type	Geometry	Damage
1a	Américo Vespucio/ Miraflores eastbound	Santiago		3 spans, PC-PSC, 5-column bents, seat abutment, MSE walls, tie downs	Skewed	Collapsed
1b	Américo Vespucio/ Miraflores westbound			3 spans, PC-PSC, 5-column bents, seat abutment, MSE walls, tie downs	Skewed	Collapsed
2a	Américo Vespucio/ Lo Echevers eastbound	Santiago	2004	3 spans, PC-PSC, 5-column bents, seat abutment, MSE walls, tie downs	Skewed	Collapsed
2b	Américo Vespucio/ Lo Echevers westbound			3 spans, PC-PSC, 5-column bents, seat abutment, MSE walls, tie downs	Skewed	Moderate
3	I-5/14 de la Fama	Santiago		15 spans, PC-PSC, 5-column bents, seat abutment, MSE walls, tie downs	Straight	Moderate
4	Pedestrian bridge over Route 5	Santiago		3 spans, 2 SG, single columns	Straight	Collapsed
5	Quilicura railway crossing at Avenida Manuel Antonio Matta	Santiago		3 spans, 5 SG, 5-column bents, seat abutment, CIP walls	Skewed	Collapsed
6a	Américo Vespucio/ Independencia westbound	Santiago	2004	6 spans, PC-PSC, 5-column bents, seat abutment, MSE walls, tie downs	Straight	Severe
6b	Américo Vespucio/ Independencia eastbound			4 spans, PC-PSC, flared bents, diaphragms, seat abutment, MSE walls, seismic bars	Straight	Moderate
6c	Américo Vespucio/ Independencia westbound exit ramp			4 spans, PC-PSC, 1-column bent, seat abutment, MSE walls, tie downs	Curved	Minor
6d	Américo Vespucio/ Independencia westbound entrance ramp			3 spans, RC box girder, single-column bents, seat abutment, CIP walls	Curved	Minor
7	Avenida Romero Acceso Sur overpass	Paine	2001	2 spans, PC-PSC, 4-column bents, seismic bars, seat abutment, earth embankment	Skewed	Collapsed
8	Avenida Chada Acceso Sur overpass	Paine	2001	2 spans, PC-PSC, 4-column bents, seismic bars, seat abutment, earth embankment	Straight	Severe
9	Maipú River	Buin	1970	13 spans, RC girders, A-shaped RC piers, diaphragm	Straight	Severe
10a	Route 5 railway crossing at Hospital westbound	Buin	2001	2 spans, PC-PSC, 3-column bents, seat abutment, tie downs	Skewed	Collapsed
10b	Route 5 railway crossing at Hospital eastbound			2 spans, PC-PSC, wall-pier bents, seat abutment, diaphragms, tie downs	Skewed	Minor
11	Estribo Francisco Mostazal (Avenida Independencia)	Santiago	2001	1 span, PC-PSC, seat abutment, seismic bars	Skewed	Minor
12	Las Mercedes Route 5 overpass	Rancagua	2001	2 spans, PC-PSC, 2-column bents, seismic bars, seat abutment, earth embankment	Straight	Severe
13a	Claro River	San Rafael	1870	7 spans, brick masonry arch (1870)	Straight	Collapsed

See notes at end of table.

Table 4. Bridges visited by reconnaissance team—Continued.

Site No.	Site Name	Location	Year Built	Structure Description		
				Type	Geometry	Damage
13b	Claro River	San Rafael		5 spans, RC arch, approach spans seat abutment	Straight	Minor
14	Pichibudis	Iloca		1 span, 2 SG, seat abutment	Straight	Moderate
15	Mataquito	Iloca	2008	4 spans, PC-PSC, 3-column bents, seat abutment, diaphragm, seismic bars	Straight	
16	Cardenal Raúl Silva Henríquez	Constitución	2002	22 spans, 3 SG, multicolumn bents, seat abutment	Straight	Moderate
17	Llacolen	Concepción	2000	Long bridge, PC-PSC, multicolumn bents, seat abutment	Straight	Collapse
18	Chepe railroad bridge over Biobío River	Concepción	1889, retrofitted in 2005	Long bridge, truss, steel-pipe column supports, CIP walls	Straight	Moderate
19a	Puerto de Coronel Muelle Norte	Coronel		Wharf with steel pile bents and RC deck	Straight	Moderate
19b	Puerto de Coronel Muelle Sur			Wharf with steel pile bents, RC deck, LRB base isolation system	Straight	None
20	Raqui 1	Raqui		2 spans, SG, wall-type bents, seat-type abutment	Straight	Minor
21	Raqui 2	Raqui		4 spans, SG, wall-type intermediate bent, seat-type abutment	Straight	Collapsed
22	Tubul	Raqui		8 spans, 3 SG, wall pier bents, seat abutments, diaphragm, seismic bars	Straight	Collapsed
23	El Bar	Arauco		1 span, 2 SG, seat abutments, retrofitted bridge	Straight	Moderate
24a	Ramadillas (west, old)	Arauco		14 spans, pier-wall bent, 4 steel beams, seat abutment	Straight	Collapse
24b	Ramadillas (east, new)			8 spans, 3 SG, wall pier bents, seat abutment, diaphragm, seismic bars	Straight	Settlement
25	Juan Pablo II	Concepción	1964	Multispan bridge, PC-PSC, multicolumn bents, seat abutment	Straight	Settlement
26	Biobío River (old)	Concepción	1943	Multispan bridge, 3 steel beams, pier-wall bents, seat abutment (1943)	Straight	Collapsed
27	La Mochita	Concepción	2005	4 spans, PC-PSC, 2-column bents, seat abutment, seismic bars	Straight	Severe
28	Vía Elevada 21 de Mayo/Cruce Ferroviario	Concepción		2 spans, RC beams, multicolumn bent, seat abutments	Skewed	Collapsed
29	Rotonda General Bonilla	Concepción	2010	5 spans, 5 SG, 6-column bents, seat abutments	Straight	Minor
30	Itata River	Coelemu	1990	22 spans, 2 SG, pier-wall bents, seat abutments	Straight	Moderate
31	San Nicolás	San Nicolás		2 spans, PC-PSC, pier-wall bent, seat abutments	Straight	Severe
32	Muros Talca (SW)	Talca		1 span, PC-PSC, seat abutment, diaphragm, seismic bars	Skewed	Moderate

LRB = Lead-rubber bearing

PC-PSC = Precast prestressed concrete I-girders.

SG = Steel girders.

RC = Reinforced concrete.

MSE = Mechanically stabilized earth walls.

CIP = Cast-in-place RC walls.

Note: Blank cells indicate unavailable data.

3.1.3 Damage Summary

The following principal types of damage were observed:

- Span unseating due to lack of transverse diaphragms and shear keys in precast prestressed concrete superstructures.
- Span unseating due to skew and insufficient support length.
- Span unseating due to ground movement caused by liquefaction-induced spreading.
- Girder distortion, column damage, and heavy scour due to tsunami wave forces.
- Column failure due to ground movement caused by liquefaction-induced spreading.

Detailed descriptions of the damage types are given in chapter 4 and chapter 5.

Many of the bridges built by concessions used precast prestressed concrete girder superstructures without diaphragms or shear keys for transverse restraint. Vertical rods called seismic bars and hold-down ties were used to prevent uplift after high vertical ground accelerations were recorded during the 1985 earthquake. These rods and ties were largely ineffective in the transverse direction, and many spans slid sideways on their cap beams. This lack of restraint also allowed a number of two-span bridges to rotate about a vertical axis through the pier and slide off their abutment seats.

In addition, several skewed spans with diaphragms and shear keys rotated about a vertical axis and were unseated in their acute corners due to insufficient support length. Straight bridges built before the concession era and those with cast-in-place (CIP) diaphragms and concrete shear keys performed well.

Despite higher than anticipated spectral accelerations, column damage was slight, perhaps because the lack of transverse restraint and insufficient support length allowed many superstructures to separate from their substructures, limiting the demand on the columns. When the superstructure did not separate, column damage was more likely to occur, such as with the shear failures due to imposed displacements from liquefaction-induced lateral spreading in several columns under the approach spans to the Juan Pablo II bridge across the Biobío River in Concepción.

In addition to this bridge, liquefaction-induced lateral spreading or settlement is believed to be responsible for the collapse or serious damage of many other structures along the coast, including the Llacolen, Chepe, Ramadillas, and Tubul bridges.

Bridges on coastal highways also sustained tsunami damage, such as the lateral distortion of the superstructure of the Pichibudis bridge just north of Iloca, the undermining of several piers due to scour, and the puncture of steel pile bents by floating debris in the Cardenal Raúl Silva Henríquez bridge across the Maule River at Constitución.

3.2. SEISMIC DESIGN REQUIREMENTS FOR BRIDGES

In Chile, as in other highly seismic countries, earthquake engineering has evolved over time, and advancements can be linked to the occurrence of large earthquakes.

According to Rodrigo Flores, the first step toward modern seismic design in Chile occurred after the 1906 Valparaiso earthquake, when the government created the Chilean Seismological Institute.⁽⁹⁾

After the 1928 Talca earthquake, another important step was taken with the passage of the 1931 Act of Construction and Urbanization, which established basic requirements for the seismic design of buildings. This document evolved over time until the 1972 creation of the Chilean Seismic Code for Buildings, which was based on U.S. and Japanese seismic codes. After the 1985 earthquake, studies were conducted to develop uniform risk maps for the country and three seismic zones were established, with the highest risk occurring along the Pacific Coast. This zoning was reflected in a 1996 update of the seismic building code.

Seismic design methodologies for bridges have also been based on U.S. and Japanese experience. According to Alex Unión and Rodolfo Saragoni, the design of concrete bridges in Chile before 1950 was based on the handbook published by Alberto Claro Velasco, *Normas para el Cálculo y Proyecto de Puentes Carreteros de Hormigón Armado* (Standards for the Design and Protection of Reinforced Concrete Road Bridges). After the mid-1950s, most designs were based on the *AASHTO Standard Specifications for Highway Bridge Design*.⁽¹⁰⁾

Before the mid-1980s, the seismic design coefficient for bridges was 0.12. This coefficient was increased to 0.15 following the 1985 earthquake, and a modified version of Division I-A of the AASHTO Standard Specifications was adopted in 1998. The design coefficient was not changed until 2001 when three seismic zones were introduced with peak ground accelerations (PGAs) of 0.2, 0.3, and 0.4 g (see figure 22). In addition, the soil factors were modified along with the response modification factors, and an allowance for the effect of scour was introduced. Column design was required to be in accordance with the AASHTO requirements for Seismic Performance Categories C and D of Division I-A.⁽¹⁰⁾ These provisions can be found in section 3.1004 of the MOP *Manual de Carreteras* (Highway Handbook) and are summarized in appendix B.⁽¹¹⁾

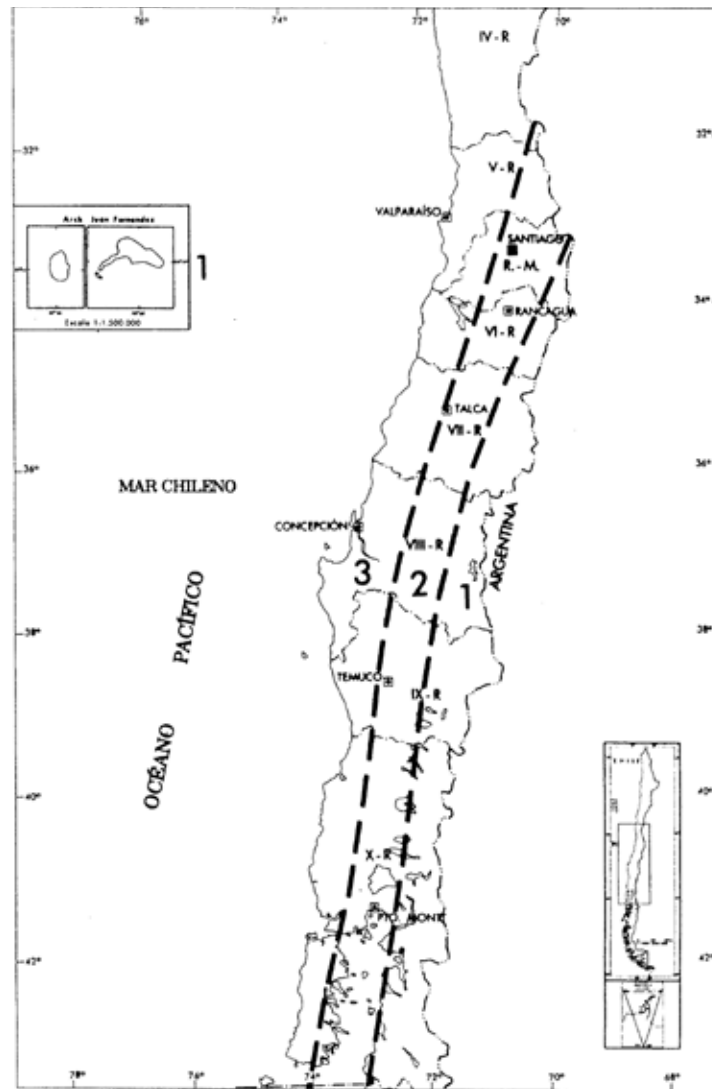


Figure 22. Map. Seismic zone map for central Chile.⁽¹¹⁾

CHAPTER 4. STRUCTURAL PERFORMANCE OF HIGHWAY BRIDGES

4.1 OVERVIEW

General observations of damage to highway bridges are reported in this chapter. The bridges are organized according to bridge type, such as concrete and steel girder superstructures, arches, and trusses. They are further divided into regular and irregular structures in terms of skew angle and curvature. The bridge site numbers are provided for reference.

The following bridges are discussed in section 4.2, Performance of Straight Concrete Bridges:

- Independencia (sites 6a–6d).
- Avenida Chada (site 8).
- Las Mercedes (site 12).
- Llacolen (site 17).
- Juan Pablo II (site 25).
- Ramadillas (sites 24a and 24b).

The following bridges are discussed in section 4.3, Performance of Skewed and Curved Concrete and Steel Bridges:

- Miraflores (sites 1a and 1b).
- Lo Echevers (sites 2a and 2b).
- Avenida Romero (site 7).
- Route 5 railway overcrossing at Hospital (sites 10a and 10b).
- Matta Quilicura (site 5).

The following bridges are discussed in section 4.4, Performance of Straight Steel Bridges:

- Tubul (site 22).
- Cardenal Raúl Silva Henríquez (site 16).
- Biobío River (old) (site 26).
- Pichibudis (site 14).
- El Bar (site 23).

- Itata (site 30).
- Pedestrian bridge over Route 5 (site 4).

Lastly, the following bridges are discussed in section 4.5, Performance of Other Bridge Types:

- Claro River (sites 13a and 13b).
- Chepe railroad bridge over Biobío River (site 18).
- Maipú River (sites 9a–9c).

4.2 PERFORMANCE OF STRAIGHT CONCRETE BRIDGES

4.2.1 Américo Vespucio/Independencia

Two bridges oriented in the east-west direction and two ramps connected to westbound traffic were inspected at this site. The eastbound bridge, built in 2004, is a four-span structure with five discontinuous precast prestressed girders and a continuous deck. It almost collapsed during the earthquake, experiencing a lateral offset of greater than 1.6 ft (0.5 m), as indicated by the use of temporary heavy supports shown in figure 23 through figure 25. The superstructure had steel stoppers but no intermediate or end diaphragms. As shown in figure 24 and figure 25, both the curtain wall of the abutment and the steel stoppers were significantly damaged. Each stopper was anchored with two bolts embedded in the cap beam at a depth of 35 inches (900 mm), as shown in figure 26. Steel stoppers were mainly used to restrain the vertical movement of girders.



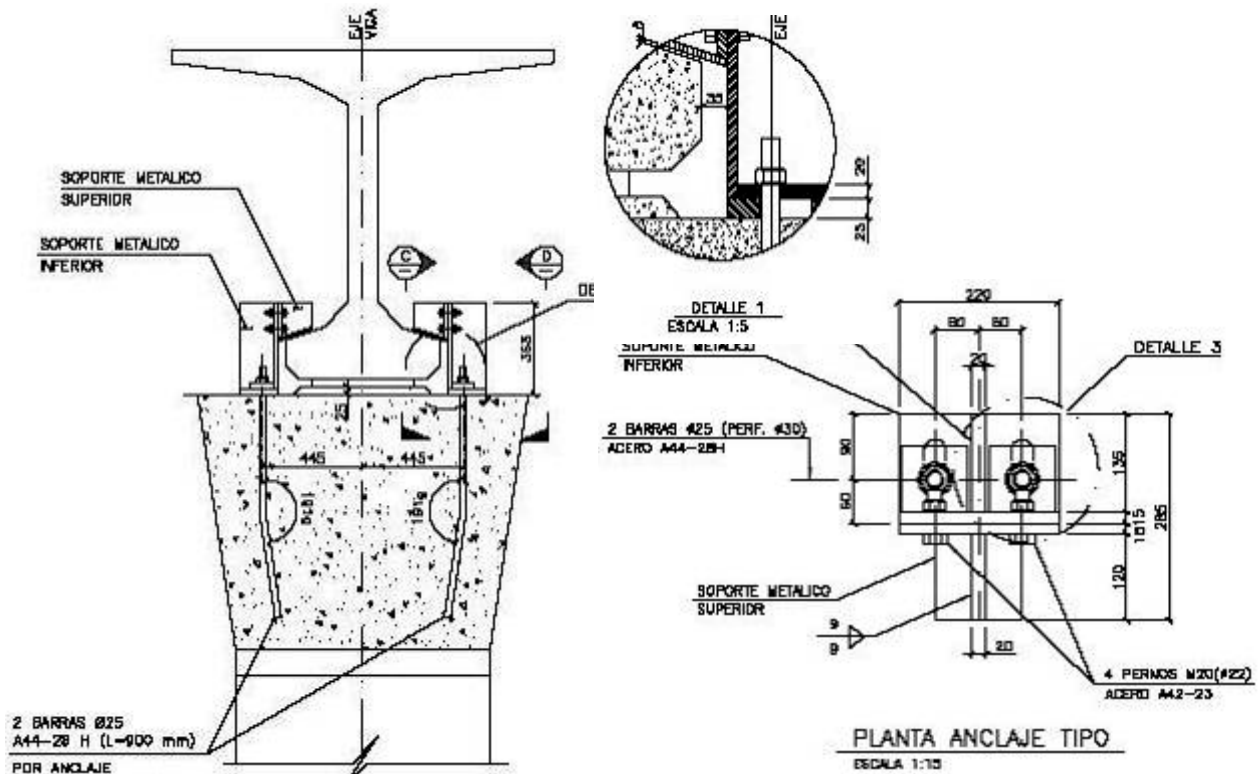
Figure 23. Photo. Damage to eastbound Independencia bridge.



Figure 24. Photo. Curtain wall at east abutment of eastbound Independencia bridge.



Figure 25. Photo. Damage to steel stoppers on eastbound Independencia bridge.



Source: MOP

Figure 26. Illustration. Details of steel stoppers.

The westbound bridge, built in 1997, is a four-span structure with six discontinuous precast prestressed girders and a continuous deck. Each bent has two flared wall piers, as shown in figure 27. The bridge was designed with both intermediate and end diaphragms. The bridge survived the earthquake with excessive deformations in the seismic bars and damage to concrete shear keys at abutments and intermediate bents (see figure 28 through figure 30).



Figure 27. Photo. Typical flared wall pier of westbound Independencia bridge.



Figure 28. Photo. Displaced seismic bar on westbound Independencia bridge.



Figure 29. Photo. Shear key damage at abutment of westbound Independencia bridge.



Figure 30. Photo. Shear key damage at intermediate bents of westbound Independencia bridge.

In comparison to the eastbound bridge, the presence of diaphragms seems to have helped maintain the structural integrity of the westbound bridge. More importantly, the concrete shear keys of the westbound bridge served their design purpose during the earthquake, as opposed to the steel stoppers in the eastbound bridge. No visible foundation damage was observed for either structure.

Additional views of the shear key damage in the westbound bridge and its entrance ramp are shown in figure 31 through figure 33. As shown in figure 31, shear key failures occurred in almost the entire structure. The entrance ramp next to the bridge is supported on two hammerhead piers at

the intermediate bents, as shown on figure 32. The shear keys at the abutment were damaged. Figure 33 shows an approximately 1.5-inch (38-mm)-wide gap between the abutment and the surrounding soil caused by strong ground shaking.



Figure 31. Photo. Westbound Independencia bridge.



Figure 32. Photo. Entrance ramp to westbound Independencia bridge.

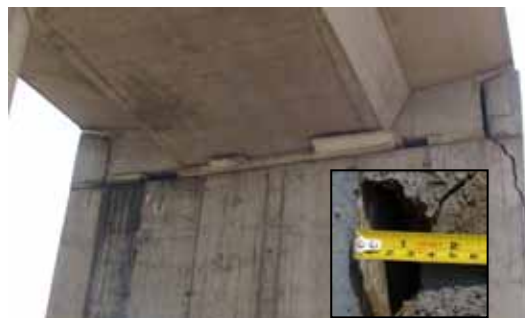


Figure 33. Photo. Shear key damage at entrance ramp abutment.

The exit ramp for westbound traffic remained in service after the earthquake. Minor damage due to pounding in the corner of the beam recess was observed on a flared wall pier close to the westbound bridge, as shown in figure 34 and figure 35.



Figure 34. Photo. Flared wall pier of exit ramp from westbound Independencia bridge.



Figure 35. Photo. Close-up of damage to exit ramp from westbound Independencia bridge.

4.2.2 Avenida Chada Acceso Sur Overpass

The two-span Chada overpass, shown in figure 36 through figure 39, is oriented approximately east-west. The bridge superstructure was displaced significantly and rotated counterclockwise in plan during the earthquake. The transverse offset between the deck and abutment seats ranged from 25 to 30 inches (640 to 780 mm). The longitudinal gap between the end of girders and the abutment was 3.5 inches (90 mm). The bottom flange and web of the exterior precast girder that hit the curtain walls at each abutment failed in shear, as shown in figure 36. The failure of the bottom flange can be seen in figure 37. The two curtain walls at the intermediate bent were both damaged, as shown in figure 38. The bridge experienced strong shaking, indicated by an induced gap around the columns, as shown in figure 39. No structural damage was observed in the bridge columns.



Figure 36. Photo. Curtain wall shear failure at abutment of Chada bridge.



Figure 37. Photo. Bottom flange damage to Chada bridge.



Figure 38. Photo. Curtain wall damage at bent of Chada bridge.



Figure 39. Photo. Soil separation from column of Chada bridge.

Although the bridge is not skewed, significant rotation was observed in its superstructure, as illustrated in figure 40. In the absence of restraint at the abutments (i.e., no diaphragm), the period of the rotational mode of vibration was shorter than the translational modes and appeared to have been strongly excited in the earthquake either by the translational components of the ground motion or by the rotational component. If the former, some degree of eccentricity between the centers of mass and stiffness would need to be present, which is quite likely given the slumping of the abutment fills and the duration of shaking.

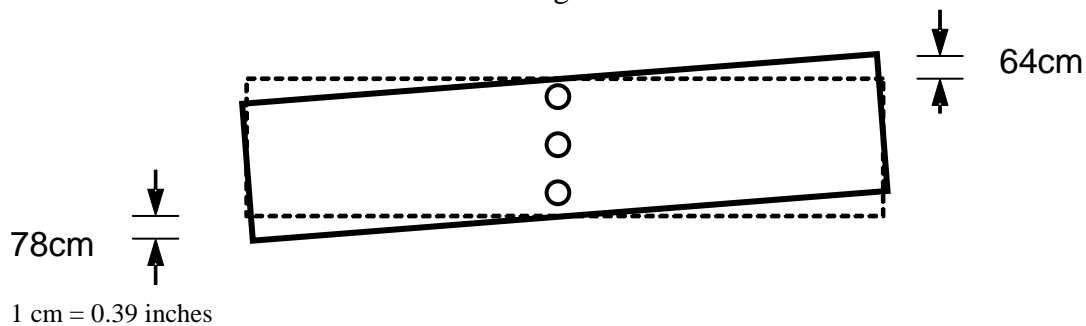


Figure 40. Illustration. Plan view of superstructure rotation of Chada bridge.

4.2.3 Las Mercedes Route 5 Overpass

The two-span Las Mercedes overpass is oriented approximately east-west and is a concrete-girder structure with a slight skew, as shown in figure 41. The superstructure comprises three precast prestressed girders and is supported on a two-column intermediate bent and two seat-type abutments, all resting on drilled shafts. Two seismic bars (deformed rebar) were installed between pairs of adjacent girders at all supports. Like the Chada bridge, the Las Mercedes bridge

experienced a significant counterclockwise rotation during the earthquake. The exterior girders rotated off their abutment seats at both ends, resulting in a longitudinal crack between the exterior and interior girders in the deck slab.



Figure 41. Photo. Las Mercedes bridge and girder unseating at abutments.

In addition, one transverse crack across the bridge deck was observed at the intermediate bent. The curtain walls were severely damaged when struck by the bridge superstructure. Temporary supports were provided for the unseated exterior girders, as shown in figure 41.

4.2.4 Llacolen Bridge Over Biobío River

The Llacolen bridge, a major crossing over the Biobío River in Concepción is oriented approximately northeast-southwest and is a multispan, simply supported concrete girder bridge. Each span consists of a deck slab and six precast prestressed girders that are supported on two five-column bents with an inverted-T cap beam. Two seismic bars are provided between each pair of adjacent girders. Figure 42 shows a general view of the bridge.



Figure 42. Photo. Llacolen bridge looking south-southwest.

As shown in figure 43, a simply supported span in the eastern approach to the bridge dropped from its seat at the river end of the span, and a temporary Bailey bridge was erected to give traffic access to the main crossing. As shown in figure 44, the end bent supporting the unseated span remained intact except for concrete spalling underneath the cap beam, as shown in figure 45. The seismic bars shown in figure 44 were deformed almost 180 degrees as the span collapsed and they were

pulled from the diaphragms. The columns supporting the cap beam experienced flexural cracks at the level of the rock rip rap on the bank below the bridge (see figure 46 and figure 47). The cracks appeared on the river side of the columns, where tension developed as the superstructure held the columns against the lateral movement imposed on the foundations by liquefaction-induced lateral spreading of the banks. The bent and columns at the opposite end of the unseated span were undamaged. However, as shown in figure 48, the nearby ground settled up to 1.3 ft (0.4 m) and experienced significant shaking, resulting in a 0.82-ft (0.25-m) separation between the columns and their surrounding ground.



Figure 43. Photo. Unseated simply supported span in eastern approach to Llacolen bridge.

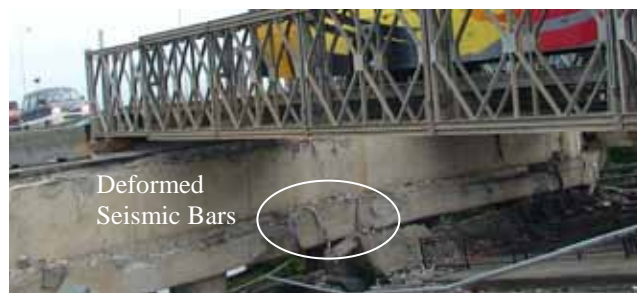


Figure 44. Photo. Abutment at unseated end of span in eastern approach to Llacolen bridge.



Figure 45. Photo. Concrete spalling beneath cap beam of eastern approach to Llacolen bridge.



Figure 46. Photo. Flexural cracks at the level of rip rap on eastern approach to Llacolen bridge.



Figure 47. Photo. Close-up view of cracks at the level of rip rap on eastern approach to Llacolen bridge.



Figure 48. Photo. Ground settlement and lateral movement of eastern approach to Llacolen bridge.

The entrance ramp for westbound traffic is a three-span simply supported box girder bridge. The girders are supported on wall piers with neoprene pads and fitted with seismic bars. The ramp was almost unseated at the river end of the last span, as shown in figure 49 and figure 50. At one intermediate bent, the seismic bars were rusty and the neoprene pads had degraded, as shown in figure 51 through figure 53.



Figure 49. Photo. Exterior face of westbound ramp to Llacolen bridge at the river end.



Figure 50. Photo. Interior face of westbound ramp to Llacolen bridge at the river end.



Figure 51. Photo. Bent of westbound ramp to Llacolen bridge.



Figure 52. Photo. Seismic bar condition on westbound ramp to Llacolen bridge.

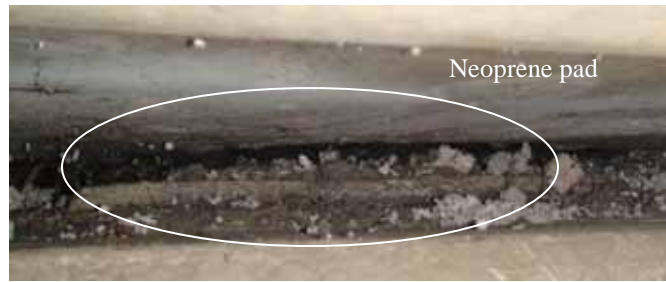


Figure 53. Photo. Neoprene pad degradation on westbound ramp to Llacolen bridge.

At the west end of the Llacolen bridge, soil settlement and liquefaction were observed at multiple locations near the bridge bents, as shown in figure 54 and figure 55. Pounding-induced damage was also observed at the supports of precast girders, as shown in figure 56 and figure 57. Minor damage also occurred when the girders engaged the concrete keys on the west abutment (see figure 58).



Figure 54. Photo. Columns with soil marks indicating ground settlement at west end of Llacolen bridge.



Figure 55. Photo. Sand boils near columns at west end of Llacolen bridge.



Figure 56. Photo. Spalling in deck slab at west end of Llacolen bridge.



Figure 57. Photo. Horizontal crack in web of end girders at west end of Llacolen bridge.



Figure 58. Photo. Spalling of shear key at southwest abutment of Llacolen bridge.

4.2.5 Juan Pablo II Bridge Over Biobío River

The Juan Pablo II bridge is another major crossing over the Biobío River in Concepción. It is oriented northeast-southwest. The northern approach to this bridge is part of an interchange that provides access to the bridge from a riverfront highway, as shown in figure 59. In addition to exit and entrance ramps, the interchange comprises a two-span approach structure and a two-span highway overpass. Each bridge superstructure consists of discontinuous precast prestressed girders and a continuous deck.



Figure 59. Photo. Approaches to Juan Pablo II bridge.

Although the riverfront overpass was generally undamaged, the two-span approach structure was damaged both globally and locally at the intermediate bent. As shown in figure 60 through figure 62, the intermediate bent had settled with respect to the two end bents, leading to a substantial depression in the roadway surface. This intermediate bent comprises two rectangular columns that most likely experienced uneven liquefaction-induced settlement during the earthquake (see figure 63). The consequential change in stiffness between the two columns shifted the longitudinal seismic force from one column to the other, which then failed in shear, as shown in figure 64. The transverse reinforcement of the failed column was spaced at 17.8 inches (457 mm). Figure 65 and figure 66 show the soil surface prior to the earthquake on the face of undamaged column and cracking in the cap beam above.



Figure 60. Photo. Southwest view of northern approach to Juan Pablo II bridge, facing Biobío River.



Figure 61. Photo. Northeast view of northern approach to Juan Pablo II bridge, facing away from Biobío River.



Figure 62. Photo. Intermediate bent of northern approach to Juan Pablo II bridge.



Figure 63. Photo. Column settlement under approach to Juan Pablo II bridge (cracks on far side).



Figure 64. Photo. Reduced column height due to shear failure under approach to Juan Pablo II bridge.



Figure 65. Photo. Soil surface on far side of undamaged column under approach to Juan Pablo II bridge.



Figure 66. Photo. Cracks on far side of undamaged column under approach to Juan Pablo II bridge.

Consistent with the behavior of the approach structure, the spans of the main bridge also appeared to have experienced uneven support settlement, which tilted the columns and rotated the bridge deck about the centerline of the bridge, as seen in figure 67.



Figure 67. Photo. Differential settlement underneath first span over water at northern end of Juan Pablo II bridge.

In addition, lateral spreading of the northeast bank pushed the columns of the bent toward the river. However, this movement was restrained by the superstructure, and the columns were consequently placed in single shear. One failed catastrophically (see figure 68 through figure 70), and the other was seriously damaged (see figure 71). The difference in behavior between the two columns might have been due to the uneven settlement and rotation of the bridge deck. The longitudinal movement of the first column was approximately 21.8 inches (559 mm) at the top of the shear plane and 15.8 inches (406 mm) at the bottom. Similar behavior was also observed in the Llacolen bridge, but the damage to the columns was not as severe.



Figure 68. Photo. Shear failure in upstream column at northern end of Juan Pablo II bridge.



Figure 69. Photo. Front face of failure plane at northern end of Juan Pablo II bridge.



Figure 70. Photo. Back face of failure plane at northern end of Juan Pablo II bridge.



Figure 71. Photo. Shear failure in downstream column at northern end of Juan Pablo II bridge.

4.2.6 Ramadillas Bridges

Two bridges cross the Piteateo River close to the town of Ramadillas in Arauco (see figure 72). The bridges are generally oriented north-south. The east bridge is a relatively new structure with total length of approximately 853 ft (260 m) comprising eight spans spaced at 105 ft (32 m). The superstructure is composed of three parallel precast prestressed girders simply supported between piers and a reinforced concrete deck. The substructure is composed of two seat-type abutments and seven intermediate wall-type piers (see figure 73 and figure 74). Reinforced concrete diaphragms are used at each abutment and intermediate pier with vertical restrainers and shear keys. This structure has two lanes, one for each direction of traffic.



© Google and GeoEye

Figure 72. Photo. Satellite image of Ramadillas bridges.



Figure 73. Photo. Side view of east Ramadillas bridge.

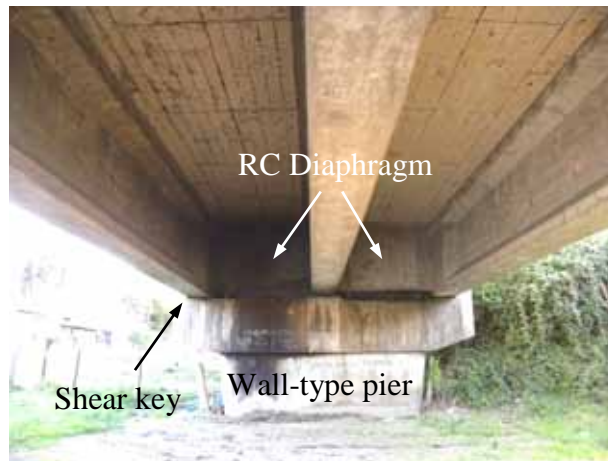


Figure 74. Photo. Wall-type pier beneath east Ramadillas bridge.

During the earthquake, the piers near the river settled due to liquefaction, causing vertical misalignment of the deck, as shown in figure 75. Sand boils appeared at the bottom of some piers, as shown in figure 76.



Figure 75. Photo. Deck misalignment under east Ramadillas bridge.



Figure 76. Photo. Sand boils close to pier under east Ramadillas bridge.

The west Ramadillas bridge is an older structure that was closed to vehicular traffic at the time of the earthquake. The total length is approximately 850 ft (260 m) with 14 spans of about 60.7 ft (18.5 m). The superstructure is composed of four parallel steel girders simply supported at the piers and a reinforced concrete deck. The substructure is composed of two seat-type abutments and 13 intermediate wall-type piers (see figure 77 and figure 78). Steel X-braced cross frames were provided at the ends of each span as well as at midspan locations. The girders were anchored to the piers by two anchor bolts, one on each side of the bottom flange.



Figure 77. Photo. Overview of west Ramadillas bridge.



Figure 78. Photo. Abutment damage beneath west Ramadillas bridge.

In addition to large inertial forces, significant settlement and lateral flow occurred due to liquefaction during the earthquake. As a consequence, one of the wall piers tilted significantly, and the adjacent span was unseated, as shown in figure 79 and figure 80.



Figure 79. Photo. Pier rotation in collapsed span of west Ramadillas bridge.



Figure 80. Photo. Sand boils near collapsed span in west Ramadillas bridge.

The largest settlements and lateral flows were observed in the river bank under the south abutments of both bridges. Figure 81 through figure 83 show the extent of these effects.

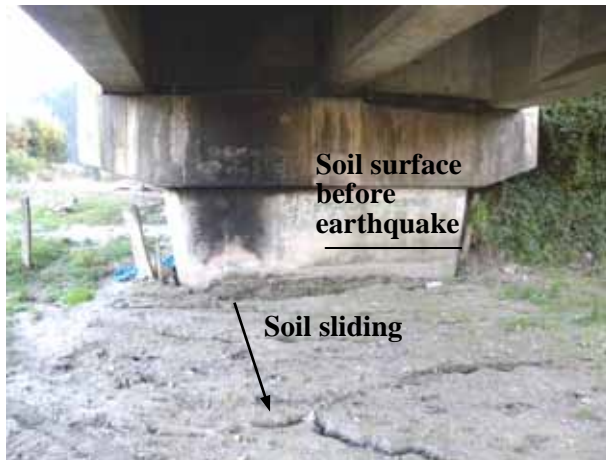


Figure 81. Photo. Settlement at south abutment under east Ramadillas bridge.



Figure 82. Photo. Sliding at south abutment under west Ramadillas bridge.



Figure 83. Photo. Block flow toward river due to liquefaction on south bank of Ramadillas bridges.

4.3 PERFORMANCE OF SKEWED AND CURVED CONCRETE AND STEEL BRIDGES

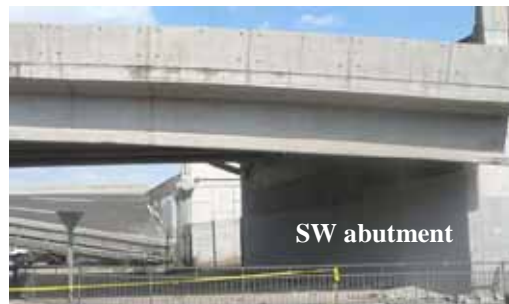
4.3.1 Américo Vespucio/Miraflores

At the Miraflores bridge site, two parallel bridges collapsed, as shown in figure 84 through figure 88. These bridges for southwest-bound and northeast-bound traffic did not have end diaphragms and appear to have had an S-shaped superelevation. Each three-span precast prestressed girder bridge had five discontinuous girders and a continuous deck slab. The abutments and two intermediate piers were skewed to approximately 20 degrees. Each girder was supported on a neoprene pad and a concrete pedestal at both ends. The girders were restrained by a pair of steel stoppers with 0.4- and 2-inch (10- and 50-mm) gaps for vertical and horizontal motions. Details of the steel stoppers are shown in figure 26.



Source: MOP

Figure 84. Photo. Northeast end of Miraflores bridge.



Source: MOP

Figure 85. Photo. Southwest end of Miraflores bridge.



Source: MOP

Figure 86. Photo. Top view of Miraflores bridge from far side



Source: MOP

Figure 87. Photo. Bottom view of Miraflores bridge from near side.



Source: MOP

Figure 88. Photo. Collapsed span of Miraflores bridge.

During the earthquake, one end span of each bridge fell from its seat-type abutment support. The other end span of one bridge was partially unseated. After the spans were removed, it was clear that the entire bridge superstructure rotated clockwise in plan as the acute corner of the bridge moved away from its supporting abutment (see figure 89 through figure 91). As a result, the curtain walls on all abutments suffered damage in the acute corners. The steel stoppers experienced little bending deformation, but their anchor bolts were either substantially deformed or sheared off.



Figure 89. Photo. Miraflores bridge after removal of superstructure.



Figure 90. Photo. Acute corner of southwest abutment of Miraflores bridge.

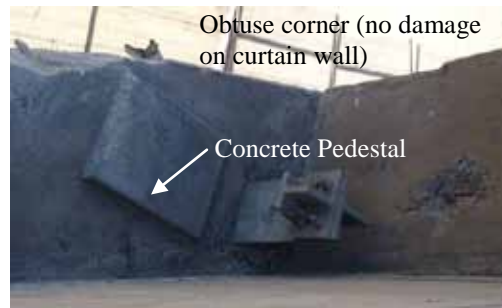


Figure 91. Photo. Obtuse corner of southwest abutment of Miraflores bridge.

4.3.2 Américo Vespucio/Lo Echevers

At the Lo Echevers bridge site, two parallel bridges had spans of 91.3, 119.1, and 91.3 ft (27.84, 36.32, and 27.84 m). As shown in figure 92 and figure 93, the southwest-bound bridge suffered minor damage while the northeast-bound bridge collapsed. The bridges did not have end diaphragms and appeared to have had an S-shaped superelevation. Each three-span precast prestressed girder bridge had five discontinuous girders and a continuous deck slab. The abutments and two intermediate piers were skewed approximately 33 degrees. Each girder was supported on a neoprene pad and a concrete pedestal at both ends. The girders were restrained by a pair of steel stoppers with 0.4- and 2-inch (10- and 50-mm) gaps for vertical and horizontal motions. Details of the steel stoppers are shown in figure 26.



Source: MOP

Figure 92. Photo. Collapsed northeast-bound Lo Echevers bridge.



Source: MOP

Figure 93. Photo. Three unseated spans of northeast-bound Lo Echevers bridge.

During the earthquake, the bridge superstructure rotated clockwise in plan as the acute corners of the bridge moved away from their supporting abutments. Some of the anchor bolts fractured, as shown in figure 94, and the elastomeric bearings seemed to have been displaced during the earthquake, as shown in figure 95. These bearings showed significant lateral bulging and may have been overstressed under gravity loads.



Figure 94. Photo. Failure of a steel stopper on Lo Echevers bridge.



Figure 95. Photo. Displaced elastomeric bearing on Lo Echevers bridge.

Since the two bridges seem identical and experienced similar ground motion, it was unclear from visual inspection why one collapsed and the other did not. A numerical analysis of a complete model of the bridge may better explain the damage pattern.

4.3.3 Avenida Romero Acceso Sur Overpass

The Romero overpass is a two-span bridge with discontinuous precast prestressed girders, a continuous deck slab, and spans of 96.8 ft (29.5 m) each. Oriented approximately east-west, the bridge is similar to the Chada overpass described in section 4.2.2 except that it has a skew angle of 31.3 degrees. The bridge has five girders but no diaphragms. Two seismic bars were provided between each pair of adjacent girders. As shown in figure 96, the intermediate bent has four columns that are supported by four drilled shafts with a pile cap between the columns and the drilled shaft foundation. Each abutment also rests on four drilled shafts. During the earthquake, the superstructure moved toward the west abutment and rotated counterclockwise away from the acute corner of the bridge. Both spans were unseated at their abutments, as shown in figure 97, which also shows lateral shear failures that occurred in the webs of the exterior girders over the bent due to excessive transverse loads.

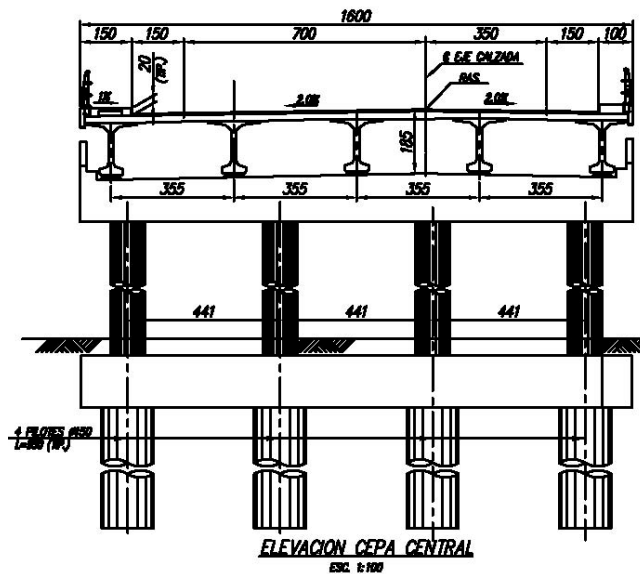


Figure 96. Illustration. Intermediate bent details for Romero bridge.



Source: MOP

Figure 97. Photo. Collapse of Romero bridge.

These observations are supported by the pounding marks on the west abutment, the damage pattern in the curtain walls of the two abutments, and the orientation of the remaining seismic bars at the intermediate bent and two abutments, as shown in figure 98 through figure 100. Figure 101 shows damage to the back wall and wing wall resulting from the girder impact on the west abutment. This damage pattern may have resulted from the combined effects of ground motion characteristics and the skew configuration. More specifically, the rotational mode of vibration of the bridge seemed very sensitive to the ground motions, which can be augmented by the skewed abutments. In addition, rotational ground motion is another plausible reason for superstructure rotation but needs to be verified by examination of the ground motion records.



Figure 98. Photo. Seismic bars at west abutment of Romero bridge.

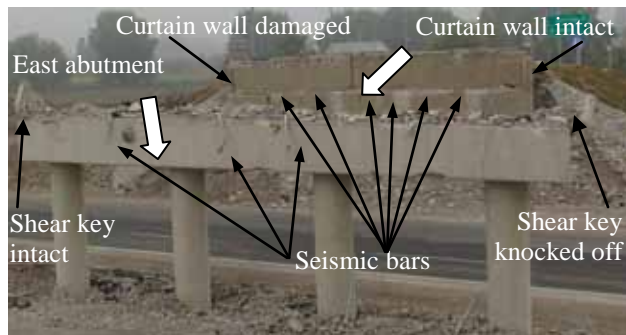


Figure 99. Photo. Seismic bars at east abutment of Romero bridge.

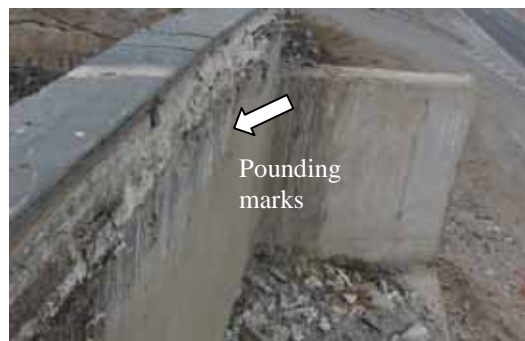


Figure 100. Photo. Pounding at west abutment of Romero bridge.



Figure 101. Photo. Back wall and wing wall damage at west abutment of Romero bridge.

4.3.4 Route 5 Railway Overcrossing at Hospital

The Route 5 railway overcrossing at Hospital comprised three parallel bridges over two railway tracks and a local road. The bridges were oriented northwest-southeast. One bridge had a steel plate girder superstructure, and the other two had precast prestressed girders. The two concrete bridges carried northbound and southbound traffic on Route 5. During the earthquake, the southbound bridge collapsed, as shown in figure 102 and figure 103.

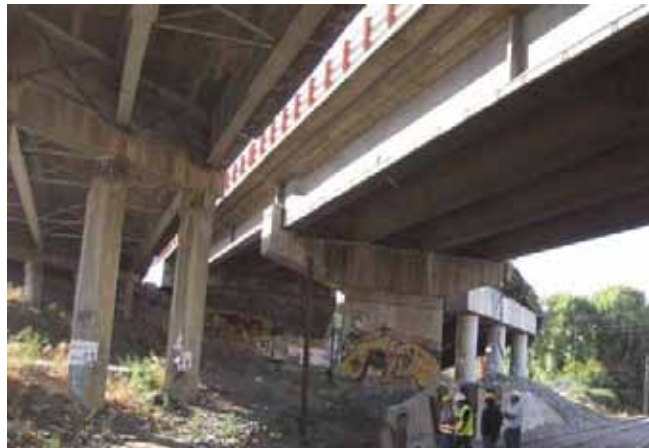


Figure 102. Photo. Three bridges (one demolished) at Route 5 overcrossing at Hospital.



Source: MOP

Figure 103. Photo. Collapse of bridge at Route 5 overcrossing at Hospital.

As shown in figure 102, plastic hinges appear to have developed at the top of the columns of the steel plate girder bridge with cross frames and shear keys. The fact that hinges formed at the top of the columns implies that strong shaking occurred transversely (i.e., in the direction of the skew). This is one of the few bridges for which column damage was observed, but field data is minimal because the bridge was demolished for safety reasons soon after the main shock. The only bridge to remain standing at this site after the earthquake had diaphragms but no skew.

The collapsed concrete bridge was a two-span structure skewed approximately 40 degrees. The superstructure comprised four precast girders but no diaphragms. The intermediate bent comprised three columns that rested on drilled shafts. At the bent and two abutments, the bridge deck was vertically tied to the substructure by seismic bars between pairs of adjacent girders. As shown in figure 103, the south span partially fell from the south abutment. The north span was completely unseated. The superstructure appeared to have rotated clockwise away from the acute corner, an observation confirmed after the bridge deck had been removed (see figure 104 and figure 105).

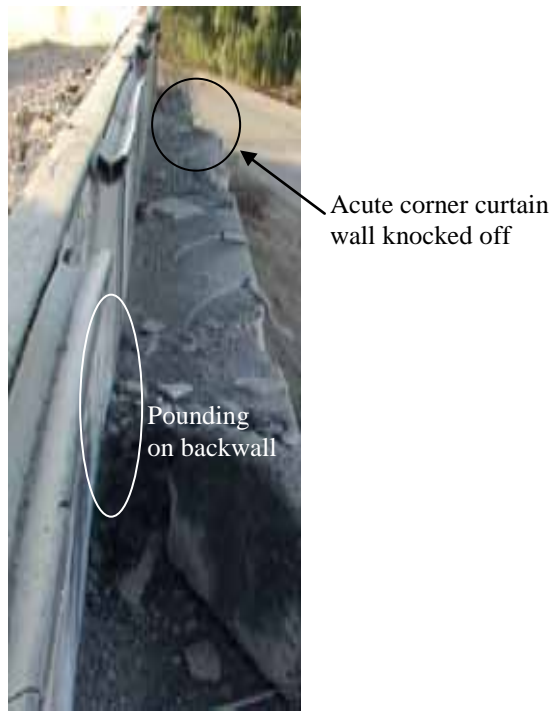


Figure 104. Photo. Damage at north abutment of Route 5 overcrossing at Hospital.

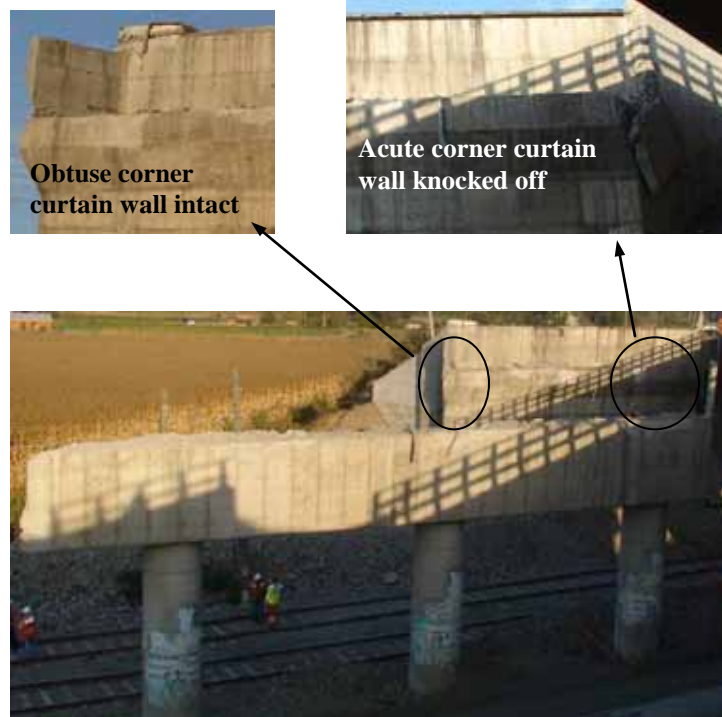


Figure 105. Photo. Damage at south abutment of Route 5 overcrossing at Hospital.

4.3.5 Quilicura Railway Overcrossing at Avenida Manuel Antonio Matta

The Quilicura railway overcrossing at the Avenida Manuel Antonio Matta, located north of Santiago, is a three-span steel bridge with five discontinuous girders, a continuous deck slab, and seat-type abutments, as shown in figure 106. The abutments and two intermediate piers are skewed approximately 45 degrees. Steel diaphragms are provided at each support, and cross frames and stiffeners are evenly spaced along the spans, as shown in figure 107 and figure 108. The intermediate piers have five circular columns and a bent cap where the simply supported girders are anchored.



Figure 106. Photo. Overview of Quilicura railway overcrossing.



Figure 107. Photo. Cross frames on Quilicura railway overcrossing.



Figure 108. Photo. Stiffeners on Quilicura railway overcrossing.

During the earthquake, the superstructure moved both longitudinally and transversely and rotated away from the acute corner of the bridge. The end span on the east side was unseated at the abutment (see figure 109), and the span on the west side was laterally displaced and almost unseated (see figure 110). For safety reasons, this span was lifted off the abutment about a day after the main shock and was lowered onto a bank of sand placed under the bridge, as shown in figure 111.

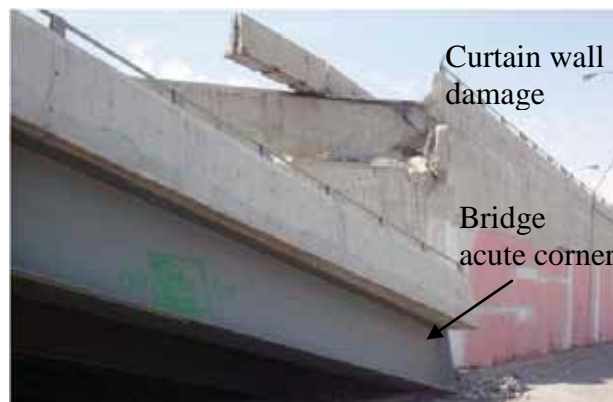


Figure 109. Photo. East abutment of Quilicura railway overcrossing.

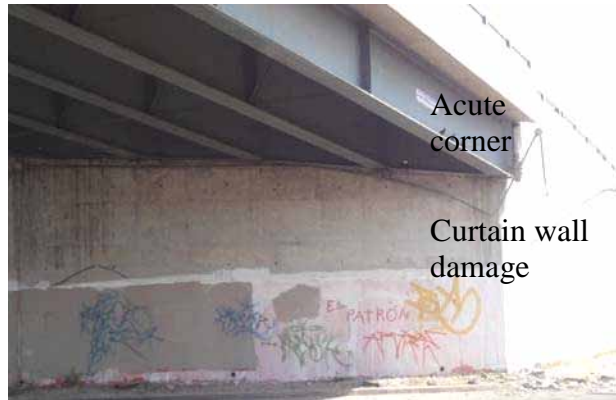


Figure 110. Photo. West abutment of Quilicura railway overcrossing.



Figure 111. Photo. West span of Quilicura railway overcrossing lowered onto sandbank.

Due to the transverse displacement and rotation of the superstructure, the curtain walls at the acute corners of the bridge sustained pounding damage. In addition, the lateral forces on the superstructure damaged the girder anchor bolts and buckled some cross frames, as shown in figure 112 and figure 113.



Figure 112. Photo. Damage to anchor bolts on Quilicura railway overcrossing.



Figure 113. Photo. Damage to cross frame on Quilicura railway overcrossing.

4.4 PERFORMANCE OF STEEL BRIDGES

4.4.1 Tubul Bridge

The Tubul bridge is an eight-span simply supported steel girder bridge oriented north-south with a span length of approximately 92 ft (28 m). Each span consists of three steel girders with concrete end diaphragms, as shown in figure 114. Shown in the inset of figure 114 are four seismic bars between the end diaphragm and the wall pier. The bridge is most likely supported on pile foundations. All the spans were unseated at their south end, resulting in the northern-most span punching into the north abutment and in the buckling of nearby pavement, as shown in figure 115 and figure 116. With the exception of span 6, all the spans were in general alignment in the north-south direction.



Figure 114. Photo. Unseating at southern ends of each span of Tubul bridge.



Figure 115. Photo. Punching of Tubul bridge deck into back wall



Figure 116. Photo. Buckling of pavement at north abutment of Tubul bridge.

Local damage to the various piers and spans was inspected by boat. As shown in figure 114, span 6 lost support at its north end. Local residents confirmed that this span was like the others immediately after the main shock, but the north end collapsed during an aftershock during the first week, probably due to rigid body rotation of the wall pier. This difference in span 6 may be attributable to the fact that the span rotated from the north to the northeast, creating load concentration on the north support. Figure 117 shows watermarks on one of the wall piers. The concrete below the high watermark showed signs of deterioration, probably due to wet and dry cycles, particularly in the mid-height of the wet area at the average watermark.

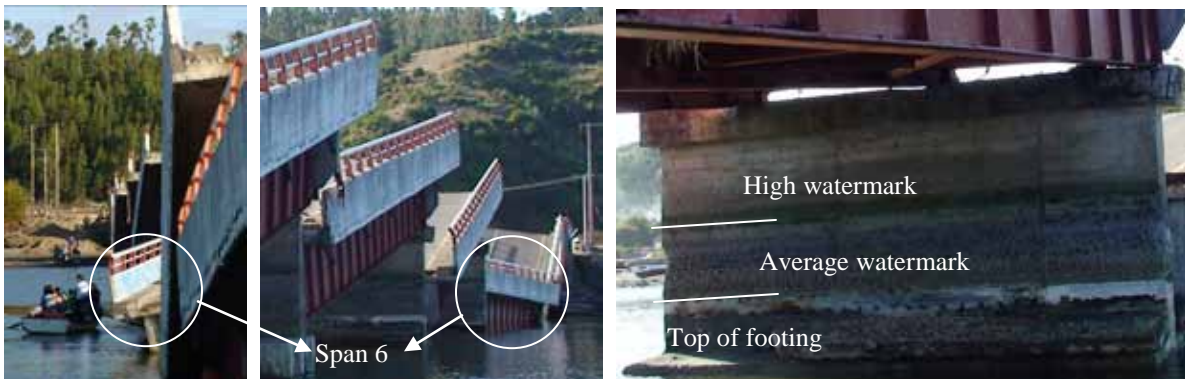


Figure 117. Photo. Span 6 of Tubul bridge, unseated at north end during an aftershock.

In general, the bottom flange of the girders buckled, as shown in figure 115 and figure 118, and the tops of the wall piers were damaged locally, as shown in figure 118 and figure 119. All of the piers were tilted toward the north abutment and were significantly damaged either by flexural effects at the top of the footing due to the maximum moment as the bridge deck pushed against the wall during the earthquake or by shear effects around the average watermark where the concrete was severely deteriorated (see figure 119 and figure 120). Concrete spalling associated with both a shear crack and a vertical crack on the wall pier are shown in figure 121. The pile cap holding the dropped span was cracked, as shown in figure 122, probably due to the impact of the falling span.



Figure 118. Photo. Bottom flange buckling and concrete spalling on Tubul bridge.



Figure 119. Photo. Shear crack in Tubul bridge.



Figure 120. Photo. Tilting wall pier on Tubul bridge.



Figure 121. Photo. Spalling due to shear action and vertical crack in Tubul bridge.



Figure 122. Photo. Crack in footing of Tubul bridge.

4.4.2 Cardenal Raúl Silva Henríquez Bridge

The Cardenal Raúl Silva Henríquez bridge, built in 2002, is a 22-span steel girder structure that crosses the Maule River in the northeast-southwest direction near Constitución. It is supported by 2 seat-type abutments and 21 intermediate bents (see figure 123). The first five bents from the northeast abutment are supported on two reinforced concrete columns and drilled shafts. The next six bents are supported on three reinforced concrete columns and drilled shafts. The following eight bents are steel pile bents with three legs (one vertical and two inclined) and horizontal struts and diagonal braces interconnecting the legs in each bent. The last two bents are supported on three reinforced concrete columns that rest on footings. The superstructure comprises two continuous segments of 11 spans each. There are fixed joints at each abutment and an expansion joint at the middle of the bridge over bent 11. Note that girders with fixed bearings at an abutment seem to defeat the purpose of having expansion joints at the abutment. At each abutment, the bottom flanges of the three girders are welded to masonry plates embedded in the abutment seat. An elastomeric pad is provided over each intermediate bent to permit longitudinal movement. Transverse and vertical movements are restrained by steel stoppers, as shown in figure 124.



Figure 123. Photo. Cardenal Raúl Silva Henríquez bridge looking south.



Figure 124. Photo. Elastomeric pad and stopper over bent on Cardenal Raúl Silva Henríquez bridge.

During the earthquake, the northeast portion of the bridge moved from west to east in the transverse direction. All steel stoppers were deformed, and girders were displaced from their elastomeric pads. The transverse diaphragms at the intermediate bents and abutments buckled, as shown in figure 125 and figure 126. At the northeast abutment, the webs and bottom flanges were fractured in all three steel girders, and both bearing stiffener and web buckling occurred, as shown in figure 127. The exterior girder also experienced web and flange bending about its weak axis, as shown in figure 128. Web buckling was observed in the longitudinal direction in the same girder. This type of damage is evidence of large longitudinal loads in the superstructure being attracted to the fixed bearing at this abutment and that these loads changed sign from tension to compression several times during the long-duration event. The weld between the girders and the masonry plate did not fail.

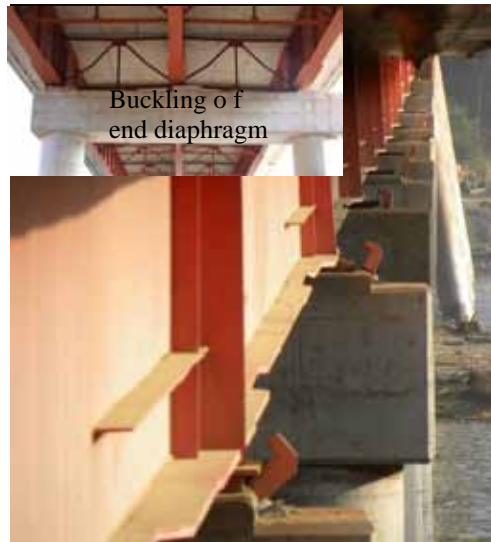


Figure 125. Photo. Girder offset and cross frame buckling on Cardenal Raúl Silva Henríquez bridge.



Figure 126. Photo. Cross frame buckling on Cardenal Raúl Silva Henríquez bridge.



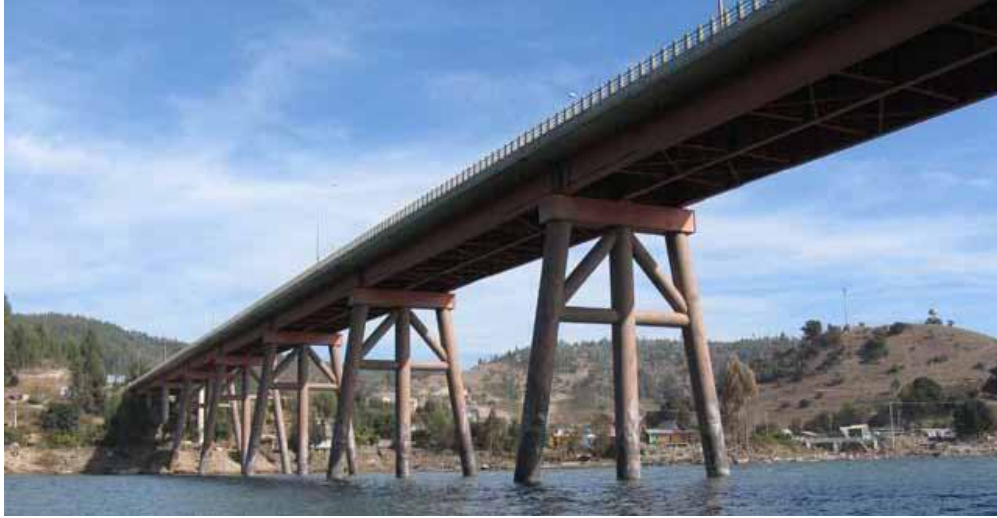
Figure 127. Photo. Girder damage at northeast abutment of Cardenal Raúl Silva Henríquez bridge.



Figure 128. Photo. Temporary repair at northeast abutment of Cardenal Raúl Silva Henríquez bridge

To maintain traffic on the bridge, a temporary cross frame was installed at the northeast abutment, as shown in figure 128. Due to severe damage in the girder webs and flanges, a steel beam was used to transfer loads from the girder flanges to the abutment seat, bypassing the webs.

As previously noted, nine spans of the southwest portion of the bridge are supported on tall steel pile bents, as shown in figure 129. The legs of these bents are fabricated from 4.9-ft (1.5-m)-diameter tubes with a wall thickness of 0.55 inches (14 mm). Their overall heights from pile tip to soffit range from 146 to 169 ft (44.5 to 51.5 m). The maximum clear height above water is about 82 ft (25 m). This portion of the structure appeared to have performed well during the earthquake but suffered local damage at several locations due to tsunamis. Four major waves were recorded nearby, with arrival times ranging from 4 to 5.5 h after the earthquake. Wave heights ranged from 22.6 to 36.7 ft (6.9 to 11.2 m), passing under the superstructure. Nevertheless, the waves eroded river sands and gravels from around the piles to a depth of about 15 ft (4.5 m), and waveborne debris punctured a hole in the wall of one of the legs of one of the bents (see figure 130 and figure 131).



Source: MOP

Figure 129. Photo. Spans and pile bents of southwest portion of Cardenal Raúl Silva Henríquez bridge.



Source: MOP

Figure 130. Photo. Erosion of alluvial material around bent legs of Cardenal Raúl Silva Henríquez bridge.



Source: MOP

Figure 131. Photo. Debris-impact hole in bent leg of Cardenal Raúl Silva Henríquez bridge.

Although the details are similar, the damage to the girders at the southwest abutment was not as severe as at the northeast abutment and was limited to the buckling of the bearing stiffeners. The reason for this difference is probably that the fillet welds connecting the girder flanges and bearing stiffeners to the masonry plates failed during the earthquake and large longitudinal loads were not attracted to this abutment (see figure 132 through figure 134).



Source: MOP

Figure 132. Photo. Fillet weld fractures at the girder-to-abutment connection on the Cardinal Raúl Silva Henríquez bridge.



Source: MOP

Figure 133. Photo. Close-up of girder end on Cardinal Raúl Silva Henríquez bridge.



Source: MOP

Figure 134. Photo. Close-up of transverse stiffeners on Cardinal Raúl Silva Henríquez bridge.

4.4.3 Biobío River Bridge

The first bridge over the Biobío River in Concepción was built in 1925 and consisted of 108 simply supported spans of approximately 49 ft (15 m) each. Each span had a timber superstructure (beams and deck) and rested on concrete piers that were supported on battered timber piles. After 40 years of service, the Chilean Highway Authority decided to replace the bridge with a steel-girder structure of 90 spans (approximately 49 ft (15 m) each), which were also supported on wall piers and timber pile foundations. During the 1960 earthquake, the five spans closest to Concepción collapsed. In 1965, an additional three spans collapsed due to scour effects. As a result, most of the pile foundations were replaced in the mid-1960s with steel pipe piles and concrete cap beams. In 1994, Japanese consultants evaluated the structural integrity of the bridge and investigated various retrofitting options. It was concluded that the bridge should be closed to traffic and was too expensive to retrofit due to the deterioration of many structural components. Nevertheless, local authorities decided to keep the bridge open for limited traffic such as pedestrians and bicycles. After additional studies, the bridge was completely closed in 2002, and all traffic was detoured to the Llacolen bridge, which had been built in 2000. In 2009, MOP contracted the firm Q&R Ingeniería to conduct a preliminary study for the replacement of the Biobío bridge.

The historic multispan bridge over the Biobío River is oriented approximately east-west. As seen in figure 135 and figure 136, the bridge superstructure consists of multiple simply supported spans with four steel girders and a concrete deck. Intermediate and end X-braced cross frames were provided in each span. Each end of a steel girder was restrained by two anchor bolts through the bottom flange, one on either side of the web. As shown in figure 137, lateral spreading due to liquefaction was observed near the north end of the bridge approaches. Many spans moved longitudinally and fell from their seats after shear failure of the anchor bolts. Some piers also collapsed in the longitudinal direction, as shown in figure 138, possibly due to liquefaction-induced vertical settlement in combination with longitudinal seismic forces. These movements may have caused the multiple cracks visible in the pile caps (see figure 139).



Figure 135. Photo. Collapsed spans in Biobío River bridge.



Figure 136. Photo. Unseated spans in Biobío River bridge.



Figure 137. Photo. Lateral spreading near east end of Biobío River bridge.



Figure 138. Photo. Collapsed spans and piers of Biobío River bridge.



Figure 139. Photo. Cracks in pile caps of Biobío River bridge.

4.4.4 Pichibudis Bridge

The Pichibudis bridge is located on a coastal road (Route J-60) in Punta Duao near Iloca. The bridge crosses a stream 980 ft (300 m) before the stream flows into the sea (see figure 140).



© Google, DigitalGlobe, Inav/Geosistemas SRL, and DMapas

Figure 140. Photo. Satellite image of Pichibudis bridge.

The single-span bridge has a total length of approximately 98 ft (30 m). The superstructure is composed of two parallel 62-inch (1,600-mm)-tall plate girders and a reinforced concrete deck slab. The girders are detailed with cross frames and stiffeners evenly spaced along the span, as shown in figure 141 and figure 142. The supports are seat-type abutments, reinforced concrete diaphragms, and concentric braces fabricated from steel reinforcing bars. The bottom flange of each girder sits on rubber pads at each abutment.



Figure 141. Photo. Cross frames in Pichibudis bridge.



Figure 142. Photo. Web stiffeners in Pichibudis bridge.

The bridge was overtopped by one or more tsunami waves, and the deck slab suffered a permanent lateral displacement of about 7 inches (180 mm) at the south abutment (see figure 143 and figure 144). At this abutment, the seaward girder rotated about the bottom flange and suffered flexural and torsional deformations about the weak axis of the section.

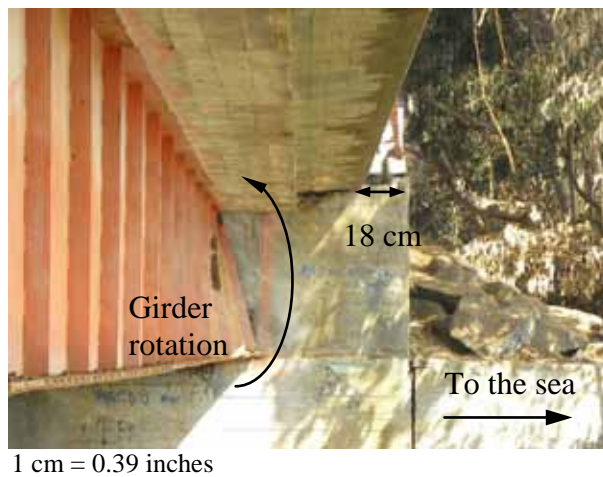


Figure 143. Photo. Offset in girder top flange of south abutment of Pichibudis bridge.



Figure 144. Photo. Offset in handrail on south abutment of Pichibudis bridge.

At the same location, damage was also found in the concrete diaphragm and bracing system, with tension rupture in one bar and compression buckling in the other one (see figure 145 and figure 146).



Figure 145. Photo. X-braces damage in south abutment of Pichibudis bridge.



Figure 146. Photo. Diaphragm crushing in south abutment of Pichibudis bridge.

According to local residents, the tsunami was characterized by three waves starting approximately 10 min after the main shock. Since the clear height of the bridge from the water level is about 4.9 ft (1.5 m), the tsunami waves passed over the bridge, inducing large lateral forces on the girders. In addition, a visual inspection of the connecting elements at the south abutment revealed corrosion in the girders, cross braces, and vertical restrainers in the reinforced concrete diaphragms (see figure 147). Due to the corrosion, the capacity of the structural components of the south abutment was less than at the north abutment, making this abutment more likely to suffer damage.



Figure 147. Photo. Damage on south abutment due to corrosion in Pichibudis bridge.

4.4.5 El Bar Bridge

The El Bar bridge is located on Route 160 in Arauco and crosses a small lake in the province of Carampangue, as shown in figure 148.



© Google, GeoEye, and DMapas

Figure 148. Photo. Satellite image of El Bar bridge.

Originally designed as a single-span bridge with a total length of approximately 98 ft (30 m), an intermediate support had recently been added (see figure 149). Apparently, this bridge suffered structural damage during flooding in 2006 and was retrofitted accordingly. In addition to the midspan support frame, two new plate girders were added parallel and adjacent to the existing girders. The new girders were connected to the existing girders using welded steel angles, as shown in figure 150. The connection between the new beams and the deck slab was made using steel angles and bolts anchored with epoxy, as shown in figure 151.



Figure 149. Photo. Side view of El Bar bridge.



Figure 150. Photo. Retrofit girder connections on El Bar bridge.

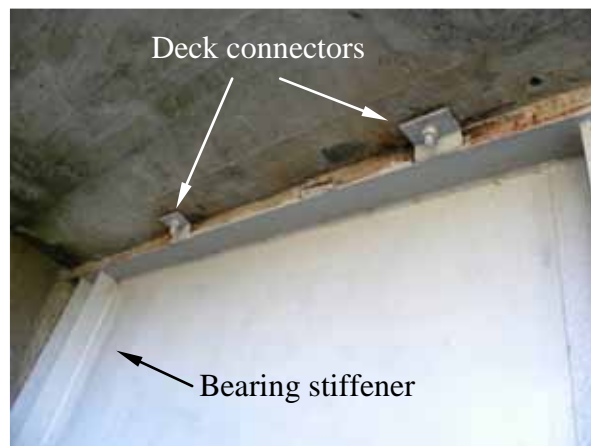


Figure 151. Photo. Retrofit deck connections on El Bar bridge.

Earthquake damage at the south abutment included a lateral permanent deformation of 9.8 inches (250 mm), girders dislodged from their neoprene pads, and damage to the concrete back wall (see figure 152 and figure 153). When the bridge was retrofitted after the 2006 floods, a rebar X-brace system and a new concrete diaphragm were added at the north abutment. The diaphragm was

anchored to the abutment seat using vertical restraining bars (seismic bars). Earthquake damage observed at this support included large deformations in the rebar of the X-brace system (tension yielding and compression buckling), lateral deformation of the seismic restrainers, and concrete crushing of the original abutment back wall (see figure 154 and figure 155).



1 cm = 0.39 inches

Figure 152. Photo. Lateral deformation at south abutment of El Bar bridge.



Figure 153. Photo. Damage at south abutment of El Bar bridge.



Figure 154. Photo. Damage to rebar X-brace system on north abutment of El Bar bridge.



Figure 155. Photo. Damage to north abutment back wall of El Bar bridge.

4.4.6 Itata River Bridge

Built in 1980s, the Itata River bridge crosses the river near Coelemu (see figure 156). The total length of the bridge is approximately 2,160 ft (660 m) made up of 22 98-ft (30-m) spans. The superstructure is composed of two parallel steel plate girders simply supported between piers and a reinforced concrete deck slab. The substructures include two seat-type abutments and 21 intermediate 39-ft (12-m)-tall wall-type piers (see figure 157). The two girders have equally spaced web stiffeners and are interconnected by inverted chevron-type cross frames. Reinforced concrete diaphragms are provided at the abutments and over each pier.



© Google, DMapas, DigitalGlobe, Inav/Geosistemas SRL

Figure 156. Photo. Satellite image of Itata River bridge.

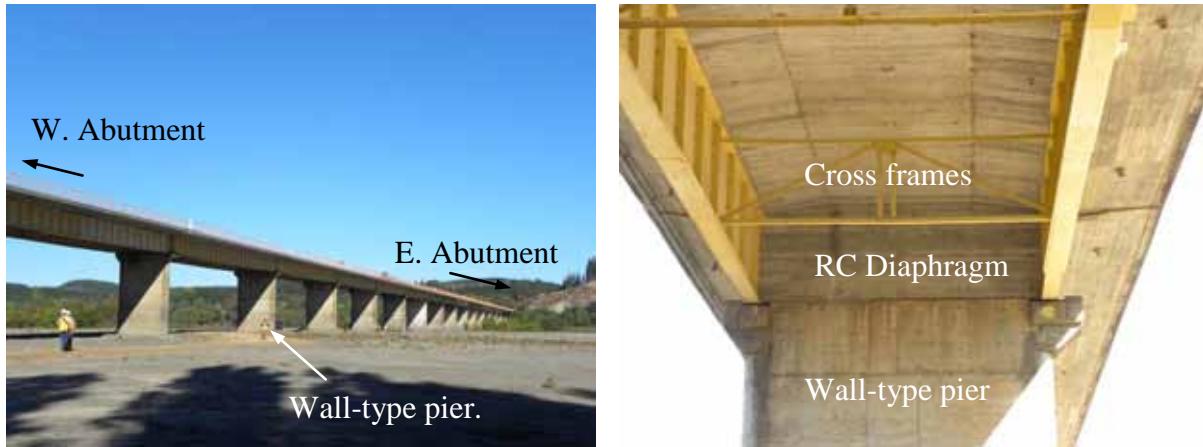


Figure 157. Photo. Side view and superstructure details for Itata River bridge.

Each girder sits on a reinforced concrete bracket at the top of each pier (see figure 158). These brackets were designed to transfer the axial and lateral forces to the piers, which are founded on rectangular pile caps.

During the earthquake, the entire structure moved both longitudinally and transversely, with larger displacements occurring in the transverse direction. As a consequence, many of the concrete brackets suffered damage at their connections to the piers. The damage was characterized by shear cracks, concrete spalling, and bar buckling, as shown in figure 159. At the time of inspection, a temporary steel structure was under construction to retrofit the brackets and allow traffic on the bridge.



Figure 158. Photo. Girder supports at each pier of Itata River bridge.



Figure 159. Photo. Damage to girder supports of Itata River bridge.

4.4.7 Pedestrian Bridge Over Route 5

Several pedestrian bridges over Route 5 collapsed during the earthquake. All appeared to have similar details and to have failed in a similar manner. The collapse of the pedestrian bridge at KM 13.8 of Route 5 North is described in this section. The bridge consisted of two approach ramps on each side of the highway and a two-span overpass oriented approximately east-west. As shown in figure 160, the two spans fell from their supports during the earthquake and were subsequently moved to the sides of the highway. Each 70.1-ft (21.4-m)-long span consisted of a concrete deck supported by two steel plate girders and four uniformly spaced cross frames. The end of each girder rested on a neoprene pad, as shown in figure 161. Each cross frame was composed of X-bracing, a top chord, and a bottom chord, as shown in figure 162. The main span was anchored at each end to a hammerhead pier by two 1-inch (25-mm)-diameter bolts through the flange of the bottom chord. Failure occurred when the anchor bolts pulled out of the bottom chord and there was insufficient seat width to prevent the girders from collapsing (see figure 163).



Figure 160. Photo. Damaged Route 5 pedestrian bridge.



Figure 161. Photo. Steel girder on neoprene pad at abutment of Route 5 pedestrian bridge.



Figure 162. Photo. End cross frame near collapsed span of Route 5 pedestrian bridge.



Figure 163. Photo. Anchor bolt failure (shear and pull out) on Route 5 pedestrian bridge.

4.5 PERFORMANCE OF OTHER BRIDGE TYPES

4.5.1 Claro River Bridges

Three arch bridges cross the Claro River just south of Curicó. Two of these are shown in figure 164: a reinforced concrete highway arch that carries northbound and southbound lanes of Route 5 and a set of unreinforced masonry arches. Built in 1870, the masonry bridge is a historic structure. It has survived numerous strong earthquakes in its lifetime, including the 1960 and 1985 events. The reinforced concrete arch suffered only minor damage during the 2010 earthquake, but the masonry bridge collapsed completely (see figure 165).

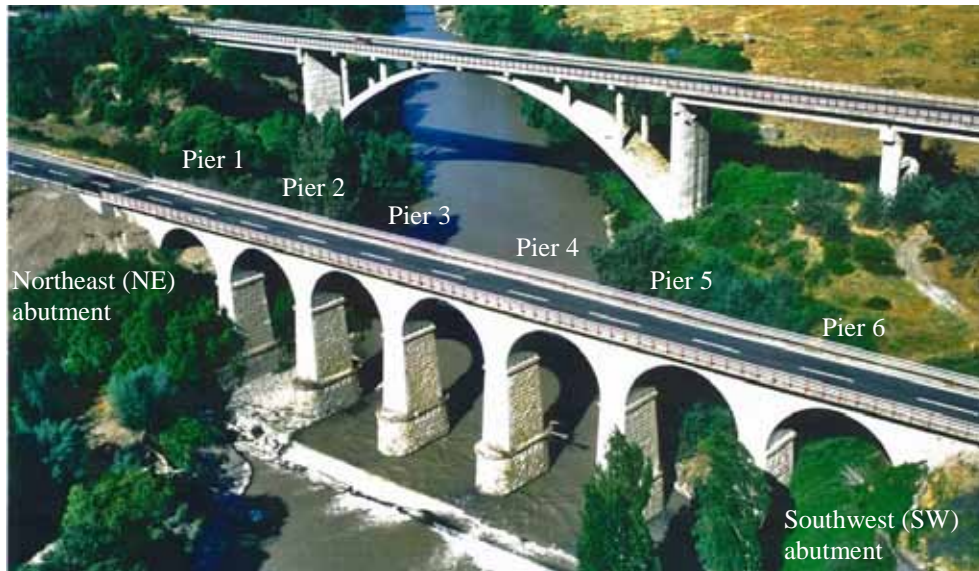


Figure 164. Illustration. Highway bridges crossing Claro River before earthquake.



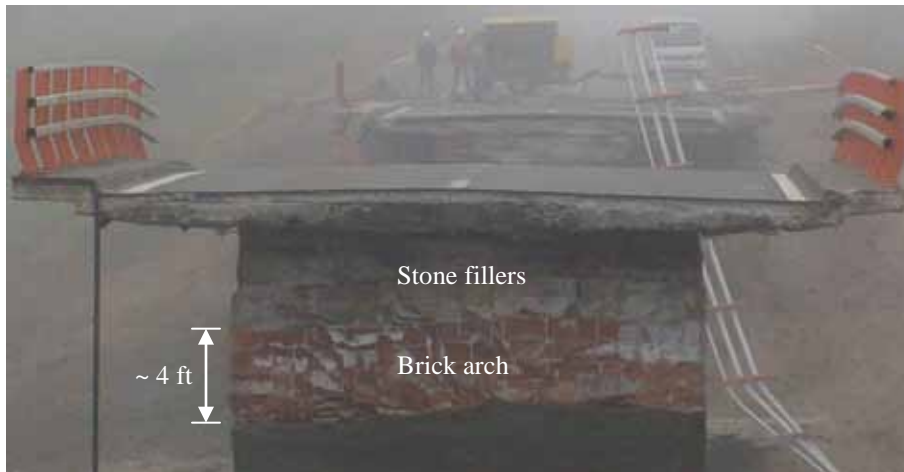
Figure 165. Photo. Collapse of masonry arch bridge at Claro River.

The masonry bridge consisted of a set of seven back-to-back arches oriented approximately northeast-southwest. Two piers survived the earthquake, and all foundations appeared to be intact, as shown in figure 165 and figure 166.



Figure 166. Photo. Close-up view of collapsed bridge at Claro River.

Figure 167 through figure 169 show details of various components of the bridge. The deck slab was approximately 8 to 10 inches (203 to 254 mm) thick, and the arch crown was approximately 4 ft (1.2 m) thick. The ribs and piers were constructed from solid brick with some stone fill above the brick ribs, as shown in figure 167 and figure 168, and faced with stone blocks or plastered with cement to give the appearance of stonework. Close inspection of the piers found some cracks between the bricks and stone facades, possibly due to shaking, but, in general, the masonry was in excellent condition. The foundations of the bridge were most likely made of stone blocks and seemed to have experienced little or no damage during the earthquake (see figure 169).



1 m = 3.28 ft

Figure 167. Photo. Deck slab and crown of arch on Claro River bridge.



Figure 168. Photo. Pier of Claro River bridge.



Figure 169. Photo. Foundation of Claro River bridge.

As shown in figure 166, the collapsed spans and other debris, including arches and piers, fell directly into the river below the bridge and were not thrown sideways, upstream, or downstream. Therefore, one scenario is that the collapse was caused by the failure of a pier with deteriorated masonry during strong shaking along the axis of the bridge. Another scenario is that the elevation difference between the end support of the arch bridge and its nearby pier caused stress concentration in two end spans along the axis of the bridge, resulting in cracks in the ribs and falling of various pieces. The collapse of two end spans reduced the inward thrust of each intermediate arch span and triggered progressive collapse. Since no deterioration of the masonry was observed in the rubble in the river bed, the second scenario is most likely.

Based on field observations, the progressive collapse of the entire masonry bridge could have occurred in four steps, as shown in figure 170. The figure shows the pre-earthquake condition of the bridge, indicating the horizontal inward thrust of each arch under gravity loads. Due to the difference in support conditions in the two end spans, the bending moment distribution along the axis of the arch bridge was quite uneven under the earthquake load. The maximum moment most likely occurred in the end spans. As a result, each end arch was subjected to cracking, leading to loss of various pieces (see step 1 of figure 170). As the end spans collapsed, the sudden loss of thrust for the adjacent spans caused significant force redistribution in a short time, resulting in cracking and collapse of the spans under gravity or earthquake loads, as illustrated in step 2. Similarly, the next spans collapsed, as shown in step 3.

Next, the center span experienced force redistribution due to the collapse of its adjacent spans. However, the change in horizontal thrust for the center span was likely smaller than that in the other intermediate spans. In addition, the earthquake excitation was likely over by that time. Therefore, the arch collapsed mainly due to its own weight while the two piers supporting the center span remained, as shown in step 4. When compared with figure 165, this collapse matches the field observations.

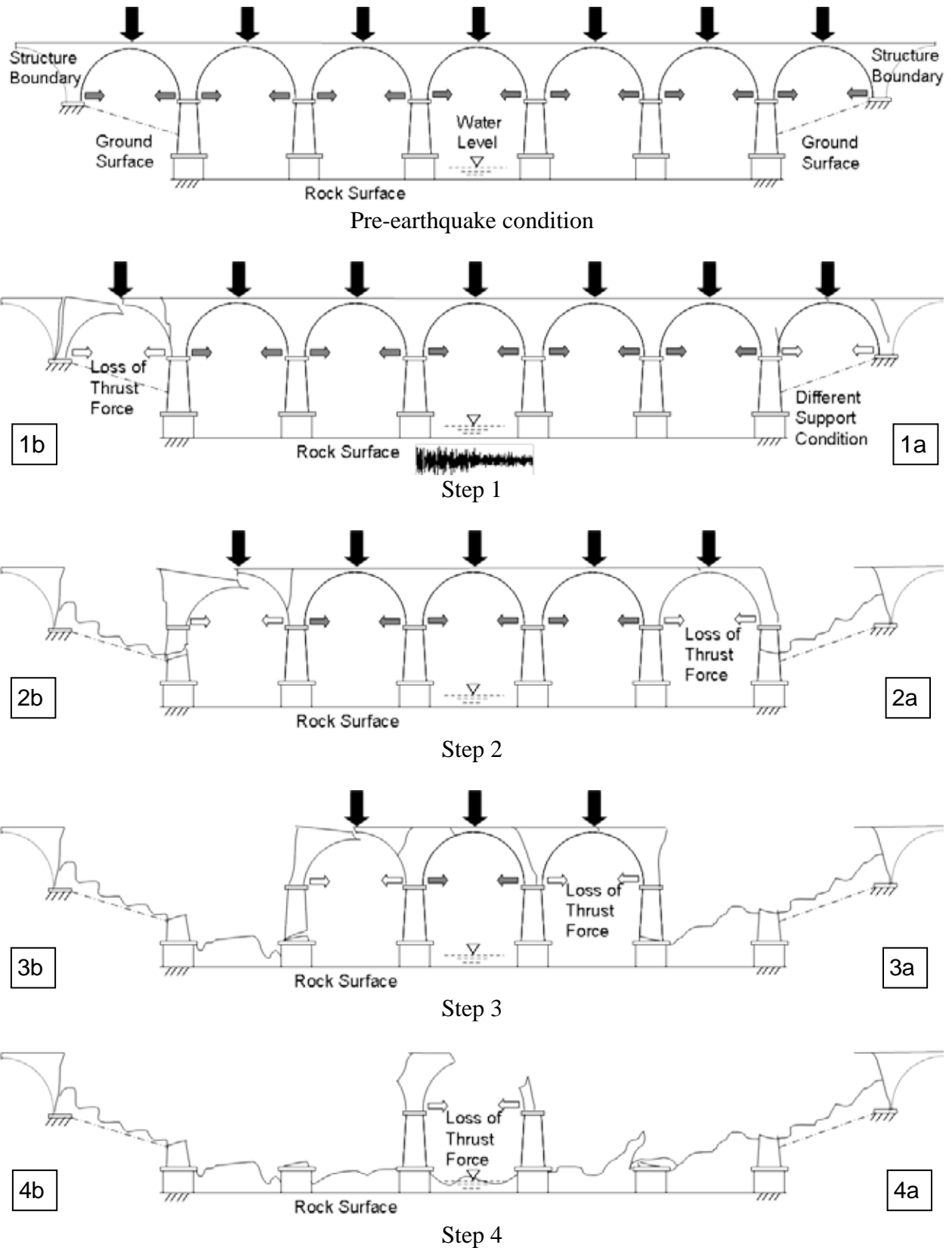


Figure 170. Illustration. Scenario for the progressive collapse of Claro River bridge.

4.5.2 Chepe Railroad Bridge Over Biobío River

The Chepe railroad truss bridge over the Biobío River was built in 1889 and retrofitted in 2005. Oriented northeast-southwest, the bridge has two continuous through-truss spans at the north end and multiple truss spans for the river crossing (see figure 171 through figure 173). The through-truss structure is supported on the north abutment and two intermediate bents. Each bent comprises two concrete-filled steel tubes that are 72 inches (1,807 mm) in diameter, as shown in figure 174. All the river spans are supported on steel towers. Each tower comprises six steel circular piles that are cross-braced for lateral strength and stiffness (see figure 172 and figure 175). A view underneath the through-truss spans and a sectional view of the remaining spans are shown in figure 174 and figure 175.



Figure 171. Photo. North end of Chepe railroad bridge over roadway.



Figure 172. Photo. River spans of Chepe railroad bridge.



Figure 173. Photo. South end of Chepe railroad bridge.



Figure 174. Photo. Bottom view and cross section on north end of Chepe railroad bridge.



Figure 175. Photo. Section on south end of Chepe railroad bridge.

At the northeast end, the bridge spans over Route O-60, which runs in a trench between two retaining walls, as shown in figure 176. The roadway slab is supported by micropiles that are approximately 20 ft (6.1 m) long. During the earthquake, the steel tube bent behind the river-side retaining wall settled approximately 12 inches (300 mm) and moved laterally toward the river for approximately 26 inches (660 mm). It also tilted toward the river about 5 degrees, as shown in figure 177. In the vicinity of the steel tube bent, the soils behind the wall settled approximately 51 inches (1,300 mm) relative to the steel bent, as shown in figure 177. The retaining wall settled over 12 inches (300 mm), as shown in figure 178, and moved laterally toward the river for approximately 26 inches (660 mm), as shown in figure 176. As a result, the seal between the roadway and toe of the retaining wall sustained damage, creating the possibility for water to flood the roadway as the river level rises during the winter. The movement of the steel tubes and retaining wall was due to liquefaction-induced ground spreading.

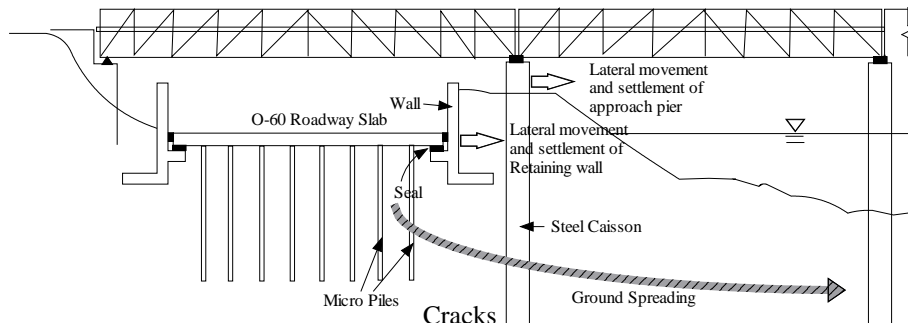


Figure 176. Illustration. Settlement and lateral movement of wall and bent due to ground spreading under Chepe railroad bridge.

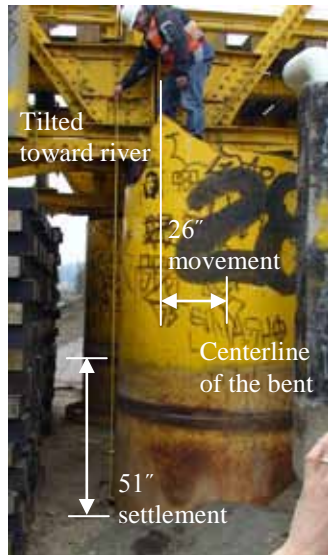


Figure 177. Photo. Settlement and tilting of bent on Chepe railroad bridge.

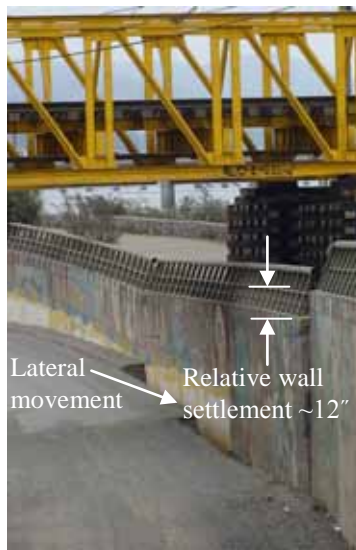


Figure 178. Photo. Settlement behind retaining wall on Chepe railroad bridge.

At the south end of the bridge, several bracing rods were broken, and at least two steel piles were fractured, possibly due to ground spreading, as shown in figure 179 and figure 180. A temporary support comprising a stack of timber ties had been erected near the damaged bent, as shown in figure 173.



Figure 179. Photo. Ruptured cross bracing at south end of Chepe railroad bridge.



Figure 180. Photo. Fractured steel piles at south end of Chepe railroad bridge.

4.5.3 Maipú River Bridges

Three bridges cross the Maipú River just south of Santiago: a railway bridge, a highway bridge (Route 5), and a local access road bridge (see figure 181).



Figure 181. Photo. Three parallel bridges crossing Maipú River south of Santiago.

The railway bridge seemed to be undamaged by the earthquake. Likewise, the Route 5 bridge sustained only minor damage despite being built in 1970. However, the Route 5 bridge is susceptible to scour, and the foundations were being retrofitted at the time of the reconnaissance visit. The local access road bridge was severely damaged in the earthquake.

Built in 1960s, the Maipú River bridge has four continuous segments of 3, 3, 3 and 4 spans, for a total of 13 spans. The segments are separated by expansion joints. Each reinforced concrete span is composed of three girders with end haunches, six intermediate diaphragms, and two end diaphragms. The superstructure is supported by A-shaped reinforced concrete piers, as shown in figure 181.

Oriented approximately north-south, the bridge was used to carry trucks loaded with gravel dredged from the river. Field observations indicated the existence of shear cracks near the ends of many of the girders, probably caused by heavy truck loading (see figure 182 and figure 183). Some of these cracks appeared to have been repaired prior to the earthquake.



Figure 182. Photo. Crushing of haunches at pier 3 of Maipú River bridge.



Figure 183. Photo. Shear cracks at span 1 of Maipú River bridge.

During the earthquake, the haunches of three girders over pier 3 were severely crushed, as shown in figure 182. Some concrete diaphragms, such as those at piers 2 and 3, were also cracked significantly, as shown in figure 184. After the earthquake, two temporary frames were installed underneath span 1, and lightweight traffic was permitted on the bridge. Most likely, the crushing of the girder haunches was mainly due to a combined effect of seismic-induced longitudinal shear force and vertical load, as shown in figure 184.



Figure 184. Photo. Longitudinal and vertical seismic forces in haunches at pier 3 of Maipú River bridge.

CHAPTER 5. GEOTECHNICAL PERFORMANCE OF TRANSPORTATION INFRASTRUCTURE

5.1 OVERVIEW

Geotechnical issues influencing the degree of damage to the transportation infrastructure include amplification of ground motions due to the presence of soft soil or basin effects, excessive lateral foundation flexibility due to soft or loose soil conditions, settlement, lateral ground movement, and ground failure. Settlement, lateral ground movement, and ground failure appeared to be primarily the result of soil weakening due to liquefaction but, in some cases, were due to seismically generated inertial forces acting on the soil mass for existing soil slopes that may have been marginally stable.

A significant portion of this chapter is devoted to the effect liquefaction can have on transportation infrastructure. *Liquefaction* is the significant loss of soil strength and stiffness resulting from the generation of excess pore-water pressure in saturated, predominantly cohesionless soils. Kramer provides a detailed description of liquefaction, including types of liquefaction phenomena, evaluation of liquefaction susceptibility, and effects of liquefaction.⁽¹²⁾

As the pore-water pressure in the soil builds up during liquefaction, loss of soil strength occurs. Then, settlement of the liquefied soil occurs as the excess pore-water pressures dissipate after the earthquake. The potential effects of strength loss and settlement include the following:

- **Slope failure, flow failure, or lateral spreading.** The strength loss associated with pore-water pressure buildup can lead to slope instability. If the soil liquefies, the soil strength reduces to a very low residual value, and the slope can become unstable. The lateral loads due to soil movement created by the unstable soil mass can cause bridge substructure distortion and unacceptable deformations and moments in the superstructure.
- **Reduced foundation bearing resistance.** The residual strength of liquefied soil is often a fraction of non-liquefied strength. This loss in strength can result in large displacements or foundation bearing failure.
- **Reduced soil stiffness and loss of lateral support for deep foundations.** This loss in soil strength can change the lateral response characteristics of piles and shafts under lateral load, making them much more flexible. This increases deformations and forces in the superstructure.
- **Vertical ground settlement as excess pore-water pressures induced by liquefaction dissipate, resulting in downdrag loads on and a loss of vertical support for deep foundations.** When liquefaction-induced downdrag occurs, it can cause significant foundation settlement, depending on the resistance of the soil at the tips of the foundation elements.⁽¹³⁾

In this chapter, these geotechnical issues are addressed for transportation facilities including bridges, pier structures, retaining walls, embankments, and roadway cuts.

5.2 GEOTECHNICAL OBSERVATIONS REGARDING BRIDGE AND PIER STRUCTURES

Of the 32 sites visited, 15 exhibited signs of liquefaction. Bridge performance tended to be poorer when liquefaction occurred than when it did not. The primary cause of transportation infrastructure performance problems resulting from liquefaction is the movement of the ground laterally and vertically in the vicinity of those facilities. However, liquefaction is not the only cause of ground movement during earthquakes. Relatively weak, sensitive clays can also lose strength during earthquakes, resulting in potentially large lateral ground movement that can have an impact on structures, walls, and roadway fills. Severe ground movements due to the presence of weak, sensitive clays were observed at 4 of the 32 sites (i.e., liquefaction was not the cause of the movements). There are still some cases of severe bridge damage or collapse among the 13 sites where neither liquefaction nor ground movement due to weak, sensitive clays appeared to have occurred. This damage was primarily due to structural weaknesses; though in many of those cases, performance problems may have worsened due to the presence of soft or loose soils.

Overall, the breakdown of observed geotechnical problems is as follows:

- **Liquefaction:** 15 sites (sites 15–22, 24–28, 30, and 31).
- **Ground movement due to weak, sensitive clays:** 4 sites (sites 7, 8, 10, and 12).
- **Ground motion amplification likely but no ground movement due to liquefaction or weak, sensitive clays:** 9 sites (sites 1–6, 11, 23, and 32).

The breakdown of the types of geotechnical issues and problems affecting the bridges visited is as follows:

- **Excessive lateral dynamic foundation movements due to the presence of loose or soft soil resulting in structural damage or collapse (without liquefaction):** Evidence was directly observable at 1 bridge site (site 8) but probably occurred at other bridge sites visited.
- **Abutment fill settlement or lateral ground movement due to the presence of weak, sensitive clays:** In all cases, it appeared that the lateral soil movement did not significantly impact the bridge (i.e., the bridge abutments did not move); 4 sites (sites 7, 8, 10, and 12).
- **Abutment fill settlement or lateral ground movement due to liquefaction, but with minimal liquefaction-induced foundation settlement or ground failure-induced foundation lateral displacement and bridge damage:** 8 bridge sites (sites 15, 16, 17 (southwest end), 18 (southwest end), 20, 21, 28, and 30).
- **Bridge pier settlement or lateral movement due to liquefaction and ground failure resulting in significant bridge damage or collapse:** 1 pier (wharf) and 10 bridge sites (sites 17 (northeast end), 18 (northeast end), 19, 21, 22, 24–27, and 31).
- **Other geologic effects potentially impacting bridges, including regional ground uplift or subsidence and tsunami damage:** 5 bridge sites (sites 20–22 for regional uplift and possibly others to a lesser degree, and sites 14 and 16 for tsunami).

5.2.1 Non-Liquefaction Geotechnical Issues Observed for Bridges

Bridge damage was generally more common in areas with poorer soils, resulting in greater amplification of ground motions. Bridges damaged in the Santiago area appeared to follow this pattern, with the heaviest damage observed in the western sector. As discussed in chapter 2, peak accelerations in the ground motions from the eastern side of Santiago were only one-third to one-half the peak accelerations measured in the western sector, based on the preliminary ground motion data available. This observation is similar to those summarized in GEER, not only for the Santiago area but also for other locations.⁽²⁾ Depending on the variability of the soil profile below each bridge, the amount of amplification may have varied from bridge to bridge, even within a given bridge site. Furthermore, the extent of the damage depended on the bridge geometry, details used, and design code followed.

5.2.1.1 Bridge Sites 1–6, North and West Santiago

The bridges located on or in the vicinity of the northwestern portion of the Américo Vespucio, the beltway around the Santiago metro area, are examples of locations where ground motion amplification due to the presence of softer or looser soils was the primary geotechnical issue affecting the damage observed (see appendix A for boring logs that provide examples of subsurface conditions in the area). These include bridges at sites 1–6. Figure 92 and figure 93 show examples in which the superstructure was damaged or collapsed while the substructure was not significantly damaged. In these cases, weaknesses in the superstructure design (lack of shear restraint, inadequate bridge seat width, etc.) helped reduce dynamic stresses and damage in the substructure as the superstructure lost its connection to the substructure during the vigorous shaking.

The bridge design and details were similar for bridge sites 1–3. All of these bridges were likely supported on 4.9-ft (1.5-m)-diameter drilled shafts, with the exception of the footing-supported Lo Echevers bridges (see appendix A). Why some of these bridges suffered severe damage and others did not is unknown at this point, but it is possible that differences in soil conditions beneath these bridges may have resulted in different degrees of ground motion amplification and therefore differences in the observed bridge performance. That is, the stronger the ground motions at a site, the more likely that bridge damage occurred.

5.2.1.2 Bridge Sites 7–10, South Santiago

At the south end of the Santiago area, soft or loose to medium dense soils were present based on the available geologic maps and boring logs (see chapter 2 and appendix A). The boring log obtained at sites 7, 8, and 10 illustrate that the upper 38 to 58 ft (11 to 16 m) of soil consists of soft to stiff clays or loose to medium dense sandy silts and silty sands (AASHTO and NEHRP Site Class D or E), which would provide maximum amplification of ground motions, based on the AASHTO guidelines for seismic load and resistance factor design (LRFD).⁽¹⁴⁾ However, this area is on the margin of a region with better soil conditions (granular medium-dense to dense soils), and therefore, subsurface conditions may be more varied, causing ground motion amplification and bridge performance to be more varied. In general, this applies to sites 7–12. For all of these bridges, the damage observed was primarily in the superstructure, with no apparent substructure damage. The foundations for the bridges at sites 7, 8, and 10 consisted of four 4.9-ft (1.5-m)-diameter drilled shafts extending into the dense soil (about 36 to 98 ft (11 to 30 m) below roadway grade),

based on as-built plans produced in 2000 and 2001 (see appendix A). Figure 185 shows an example in which the substructure was left intact with little or no damage. However, one of the foundations supporting one of the bridge abutments appears to be less vertical than would be expected, though no specific evidence of foundation damage (e.g., cracking) was observed. However, in one of the bridges (site 8, Avenida Chada overpass), dynamic lateral movement of the center pier shaft foundation had occurred (on the order of about 7.8 inches (200 mm)) and lateral foundation movement likely contributed to bridge superstructure damage (see figure 186). Figure 187 shows additional evidence that may point to the transverse rocking that occurred at the Avenida Chada overpass. The pavement crack shown in the figure is directly below the centerline of the bridge. While it is possible that the foundations supporting the bridges at all or most of the bridges at sites 1–10 exhibited significant lateral movement due to the presence of soft soils, it was not directly observable, except at site 8.



Figure 185. Photo. Damage at Romero bridge and shaft foundation supporting abutment (collapsed superstructure removed).



Figure 186. Photo. Interior pier of Chada structure with 5.8- to 7.8-inch (150- to 200-mm) gap in soil transverse to bridge centerline.



Figure 187. Photo. East abutment of Chada structure showing large pavement crack directly below bridge centerline.

Another problem that occurred at these bridge sites was settlement of the approach fills, where total approach fill settlement was on the order of 3 ft (1.0 m). However, for bridge sites 7 and 8, this settlement seems to be entirely from within the fill due to the fill slumping during shaking.

The fill slumping did not appear to be caused by liquefaction. It is possible that during shaking, the base of the fill slid away from the embankment centerline due to some type of block failure, possibly at the boundary with relatively soft clay soils, allowing the embankment to slump. Figure 188 is a diagram of fill slumping, and figure 189 shows one of the actual abutment fills. The type of fill material used here and how well it was compacted is unknown.

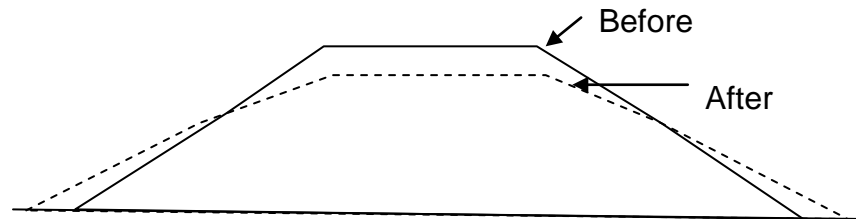


Figure 188. Illustration. Fill slumping observed for bridge sites 7 and 8.



Figure 189. Photo. Fill slumping observed at Romero bridge.

Significant roadway fill settlement and lateral movement also occurred at bridge site 10 (see figure 190). However, the difference between this site and sites 7 and 8 is that at site 10, it appears the soil beneath the roadway embankment failed, possibly in bearing, though the failure appears to be fairly shallow. Lateral movements of over 7 ft (2 m) appear to have occurred, considering the distortion in the sign bridge, and uplift of the soil surface beyond the toes of the approach fill also appears to have occurred (see figure 191). Lateral movement of the fill and soil below the fill at site 10 is rather complex and will require further investigation to determine what really happened. However, based on the available boring log, the upper soils consist of weak and likely sensitive clays (see appendix A). These clays are probably the source of the fill stability problems observed at this site. In any case, the bridge abutment at site 10 appeared to be unaffected by the observed approach fill movement, although the superstructure for one of the bridges at this site collapsed.



Source: MOP

Figure 190. Photo. View of roadway fill failure from abutment of Route 5 railway crossing at Hospital.



Source: MOP

Figure 191. Photo. Close-up of approach fill failure and damaged sign bridge.

5.2.2 Liquefaction Impact on Performance of Bridge and Pier Structures

All of the following general conditions are necessary for liquefaction to occur:

- The presence of groundwater, resulting in a saturated or nearly saturated soil.
- Predominantly cohesionless soil that has the right gradation and composition. Liquefaction has occurred in soils ranging from low plasticity silts to gravels. Clean or silty sands and non-plastic silts are most susceptible to liquefaction.

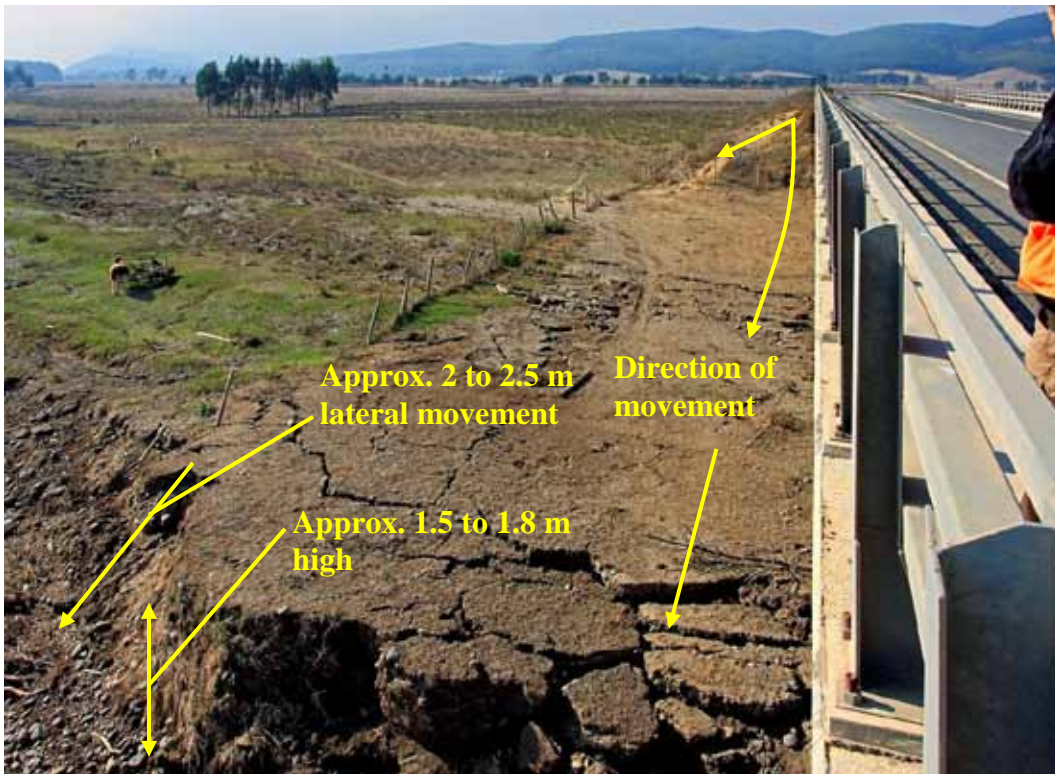
- A sustained ground motion that is large enough and acts over a long enough period of time to develop excess pore-water pressure equal to the effective overburden stress, thereby significantly reducing effective stress and soil strength.
- Soil characterized by a density that is low enough for the soil to exhibit contractive behavior when sheared undrained under the initial effective overburden stress.^(13,14)

Since detailed, site-specific subsurface data were not available for most of the sites visited, heavy reliance was placed upon visual surficial evidence that liquefaction had occurred to help interpret the structure performance observed. This section summarizes examples of those observations, how the liquefaction issue has been dealt with in the past, and the observed performance of various structures. That performance is interpreted with consideration of the local geology (and subsurface and ground water data if available), the likely extent of liquefaction, and the effect of the local topography on soil stability and deformation.

5.2.2.1 Signs of Liquefaction Observed

As previously mentioned, 15 of the bridge sites visited exhibited signs of liquefaction resulting from the offshore Maule earthquake. These liquefaction signs included lateral ground movement and cracking (i.e., lateral spreading or flow failure), ground settlement, and sand boils or otherwise ejected sand or silt in fissures. Structures at such sites tended to display the most damage and the poorest seismic performance due to the heavy demands such conditions placed on them, with a few notable exceptions. In some cases, surface expressions of liquefaction could not be directly observed (e.g., piers located in rivers), so liquefaction had to be inferred based on bridge performance observations such as settlement or tilted piers and columns that could be explained in no other way.

Examples of liquefaction signs and effects are provided in figure 192 through figure 199. Figure 192 shows lateral spreading that occurred at the Mataquito bridge site (site 15). Lateral movements of up to 7 to 8.2 ft (2 to 2.5 m) and vertical settlement of up to 3 ft (1 m) (average of 1.6 ft (0.5 m) across embankment near bridge abutment) appear to have occurred at the northeast end of the structure, involving the abutment fill and over 300 ft (100 m) of gently sloping ground to the river bank. However, as can be seen in figure 193, the lateral deformation directly beneath the bridge was less than the deformation just outside the edges of the bridge, indicating that the bridge foundations may have helped to restrain lateral movement of the soil. This also means that lateral soil loads may have been acting on the bridge foundations. Similar lateral spreading failures were observed at the opposite end of this bridge, although in that case, the abutment fill was not involved in the lateral spreading. Based on surface observations, it appears that these lateral spreading failures at the Mataquito bridge are relatively shallow in depth, probably on the order of 7 to 8.2 ft (2 to 2.5 m). A similar example of relatively shallow lateral spreading failure is provided in figure 194 for Ramadillas bridge (site 24), where the buildup of soil behind the bridge pier can be observed. Based on the pattern in the ground cracks, it appears that the soil was fluid enough to attempt to flow around the pier but was only partially successful in doing so.



1 m = 3.28 ft

Figure 192. Photo. Lateral spreading at Mataquito bridge.



Figure 193. Photo. Lateral spreading at Mataquito bridge with lateral movement beneath and around bridge.



Figure 194. Photo. Lateral spreading and ground failure at old Ramadillas bridge.

Figure 195 and figure 196 provide examples of sand boils and ejected sand from ground fissures due to liquefaction. In figure 195, the southwest end of the Llacolen bridge, the ground water depth is relatively shallow (less than 3 to 7 ft (1 to 2 m)). In figure 196, La Mochita bridge, the ejection of sand through ground fissures due to elevated pore pressures from liquefaction appeared to be more vigorous, considering the greater depth to the water table (approximately 13 to 16 ft (4 to 5 m)).



Figure 195. Photo. Sand boils at southwest end of Llacolen bridge.



Figure 196. Photo. Ejected sand due to liquefaction and ground failure at La Mochita bridge.

Figure 197 and figure 198 provide examples of more severe ground failure caused by liquefaction. In these cases, the ground water needed for liquefaction was 7 to 16 ft (2 to 5 m) below the ground surface, and the remaining soil above that layer was non-liquefied crust. Due to the weakness of the liquefied soil, a slope failure ensued. This type of failure can cause the greatest damage to bridges due to the significant volume of stronger, heavier soil moving laterally into the bridge foundations and vertically along the foundations. Because the non-liquefied crust is stronger than the liquefied soil, it is less able to flow around the foundations and is more likely to force the foundations to bear the full brunt of the lateral soil force.

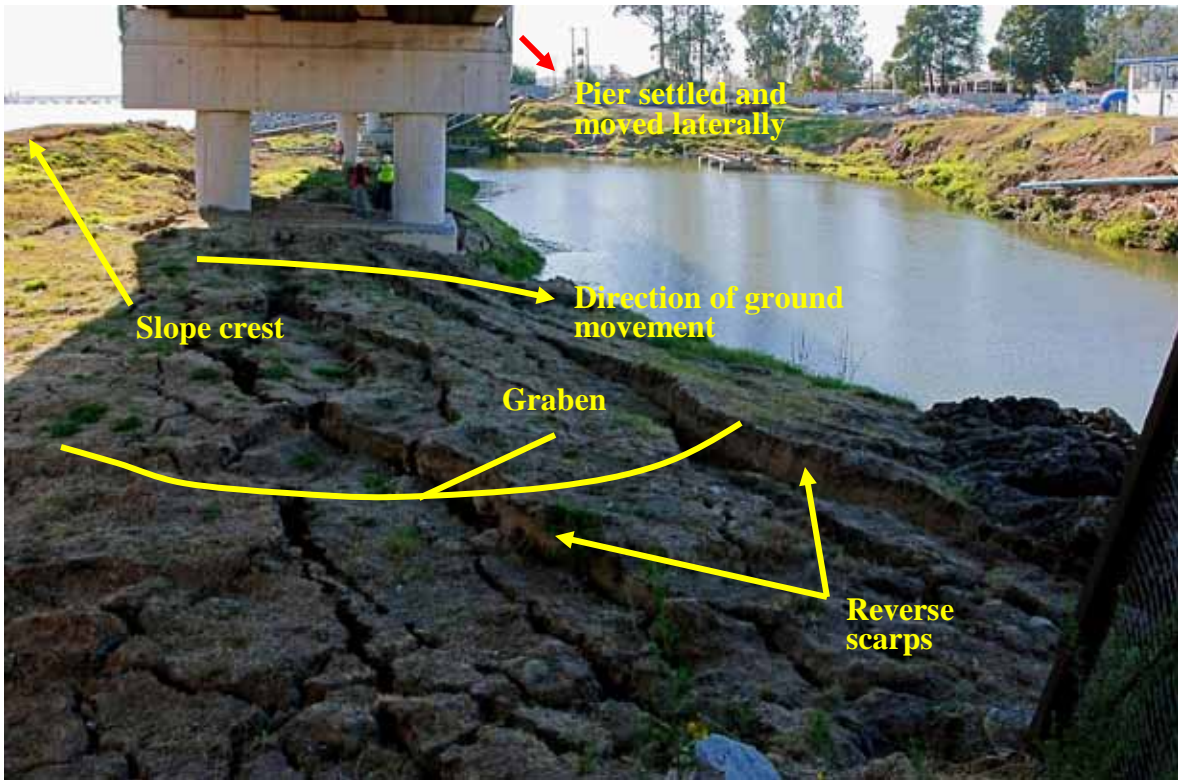


Figure 197. Photo. Severe ground failure at La Mochita bridge.



Figure 198. Photo. Lateral spreading and ground failure at Raqui 2 bridge.

Figure 199 shows an example in which a center pier in the middle of the river settled (about 1.9 to 3.1 inches (50 to 80 mm)), but, because of the water in the river, no specific evidence of liquefaction could be observed. It is likely that liquefaction is the cause of this kind of effect on the bridge, although it is also likely that the liquefied layer is not extensive because the amount of deformation in the foundation is relatively small.



1 cm = 0.39 inches

Figure 199. Photo. San Nicolás bridge center pier settlement probably due to liquefaction of soil layers beneath river.

5.2.2.2 Use and Performance of Ground Improvement to Mitigate Liquefaction Effects

According to engineers at MOP and Chilean universities, bridges and other transportation structures have historically not been designed to resist the effects of liquefaction. Until the 2010 offshore Maule earthquake, liquefaction had only been reported in limited areas of hydraulically placed fill, and the problems resulting from that liquefaction had been minimal. This was not the case for the Maule earthquake. Liquefaction problems were widespread and, in some cases, resulted in significant failures of structures and other facilities (see GEER for additional information).⁽²⁾ The only ground improvement the team was made aware of to address liquefaction was deep dynamic compaction (DDC) conducted beneath some of the approach fills near the north end of the Juan Pablo II bridge in Concepción. Based on field observations at that site, the ground improvement was only partially successful, as shown in figure 200 and figure 201. DDC is generally not very effective for stabilizing deeper liquefaction in soils below the water table (i.e., water is virtually incompressible, and, in finer sandy or silty soils, the water does not have time to escape during DDC impacts, preventing reduction of pore volume). However, the specific limits of the DDC and the subsurface conditions are not known, so the apparent lack of success of the DDC cannot be fully investigated at this time.



Figure 200. Photo. Ramps at Juan Pablo II bridge where existing ground was improved with DDC.



Figure 201. Photo. Lateral movement of fill in ramps at Juan Pablo II bridge.

5.2.2.3 Site-Specific Impacts of Liquefaction on Bridge Performance

Among the sites visited by TIRT, the impact of liquefaction on bridges and their approaches varied from no impact to structure collapse. The specific reasons why some bridges performed reasonably well despite signs of liquefaction cannot be determined without subsurface data to assess the depth of liquefaction and what should have been expected regarding settlement and lateral spreading or flow failure. However, it is possible to summarize the damage trends that are likely the result of liquefaction effects.

Liquefaction can result in vertical and lateral bridge foundation movements that exceed a bridge's ability to tolerate them as well as stresses in foundation and substructure elements that can result

in component damage or failure. Liquefaction can reduce lateral soil stiffness (i.e., p-y curves), create downdrag loads on foundation elements due to liquefaction settlement, cause permanent lateral displacement of foundation and substructure elements, and increase lateral forces acting on foundation and substructure elements, which can cause the element to crack or fail. If ground improvement to prevent liquefaction is not conducted, the foundation elements must be designed to resist the loads placed on them due to liquefaction.

Specific descriptions of the effect liquefaction may have had on bridge performance for several of the sites visited are provided in the sections that follow.

5.2.2.3.1 Mataquito Bridge (Site 15): The Mataquito bridge provides an example of the performance impact caused by a relatively shallow lateral-spreading failure. In this case, the depth of lateral spreading appeared to be approximately 4.9 to 8.2 ft (1.5 to 2.5 m) based on the surficial expression of the soil movement. The bridge substructure/foundations were not significantly pushed laterally, and the affected bridge spans remained intact and functional. The Ramadillas bridge, though not discussed in detail here, provides a similar example of the effects of shallow lateral spreading (see figure 194).

For the Mataquito bridge, it appears that the abutment fill primarily moved parallel to and around the abutment wall rather than applying the full lateral force of the soil directly into the abutment. Ridging along the approach fill slope toe and longitudinal roadway pavement cracking appear to confirm that most of the soil movement was perpendicular to the roadway centerline (also identified in GEER).⁽²⁾ Significant abutment fill settlement (approximately 1.6 to 3 ft (0.5 to 1 m)) also occurred, requiring some easily accomplished repair to the bridge approach fill (see figure 202 and figure 203). It also appeared that the soil was able to partially flow around the pier and foundation elements, possibly reducing the lateral loads enough that the foundations could resist them (see figure 192 and figure 193). As shown in figure 202 and figure 203, the bridge itself was virtually unaffected by the lateral spreading other than some minor abutment wall crushing where the abutment and bridge deck were shoved together either during shaking or as a result of very small lateral movement of the abutment. There was not enough movement or damage to affect bridge operation. Settlement of the soil around the interior piers was also observed (see figure 204) and appeared to be partly due to lateral spreading of the soil down slope as well as to possible deeper liquefaction-induced settlement that contributed only to downdrag forces on the foundations.



1 m = 3.28 ft

Figure 202. Photo. Abutment fill settlement of northeast abutment of Mataquito bridge.



1 m = 3.28 ft

Figure 203. Photo. Soil settlement without bridge settlement at northeast abutment of Mataquito bridge.



1 m = 3.28 ft

Figure 204. Photo. Soil settlement at interior pier at northeast abutment of Mataquito bridge.

Specific details regarding the foundations of the bridges were not available, but considering the recent construction date for the bridge (2007–2008) and the size of its columns, it is likely that the bridge was founded on drilled shafts (typical diameter of 4.9 ft (1.5 m)) that are deep enough to reach denser soil. This may explain why the bridge itself did not settle, but that hypothesis will need to be confirmed once bridge foundation details and soil subsurface information are available.

5.2.2.3.2 Raqui 1 bridge (Site 20): The Raqui 1 bridge is somewhat transitional with regard to the effects of liquefaction. The primary impact of liquefaction for this bridge was abutment fill settlement, though evidence of relatively minor lateral spreading below the abutment fills was present. Figure 205 shows approximately 3 ft (1 m) of fill settlement at the northwest abutment. The southeast abutment shows a similar amount of settlement. However, figure 206 shows that some lateral movement of the northwest abutment may have occurred (approximately 2.9 to 3.9 inches (75 to 100 mm)), severe enough to cause crushing of the abutment wall against the bridge girders and deck but not to shut down the bridge once the abutment approach fills were rebuilt to match the bridge deck elevation. A small concrete gravity wall adjacent to the abutment also displaced and tilted laterally down slope toward the river (see figure 206). It also appeared that more lateral movement occurred on one edge of the northwest abutment than on the other, indicating that some twisting of the abutment occurred. The abutment wall crushing could be partially due to strong shaking of the superstructure, forcing the bridge girders and deck into the abutment. However, the abutment wall crushing, signs of abutment fill displacement, twisting of the abutment, and lateral movement of the gravity wall adjacent to the abutment indicate that abutment movement toward the river occurred, likely due to liquefaction. It appeared that the southeast abutment did not move due to the liquefaction and lateral spreading. The difference in the liquefaction effects at the two abutments may be due to the presence of more gently sloping ground around the approach fill for the southeast abutment than for the northwest abutment (see figure 207). There was some evidence

that the direction of slope movement was perpendicular to the roadway centerline, especially a few meters or more away from the abutment (see figure 208). However, since the approach fills had been restored to the bridge deck elevation before the team's arrival, some of the slope failure cracking and movement patterns had been covered by new fill. The age of the bridge, the subsurface conditions, and the foundation details were not available to TIRT. Therefore, additional investigation is needed to more accurately assess the bridge performance.



Figure 205. Photo. Abutment fill settlement at northwest abutment of Raqui 1 bridge.



Figure 206. Photo. Abutment and girders shoved into each other and deck at the northwest abutment of the Raqui 1 bridge.



Figure 207. Photo. Raqui 1 bridge viewed from north side.

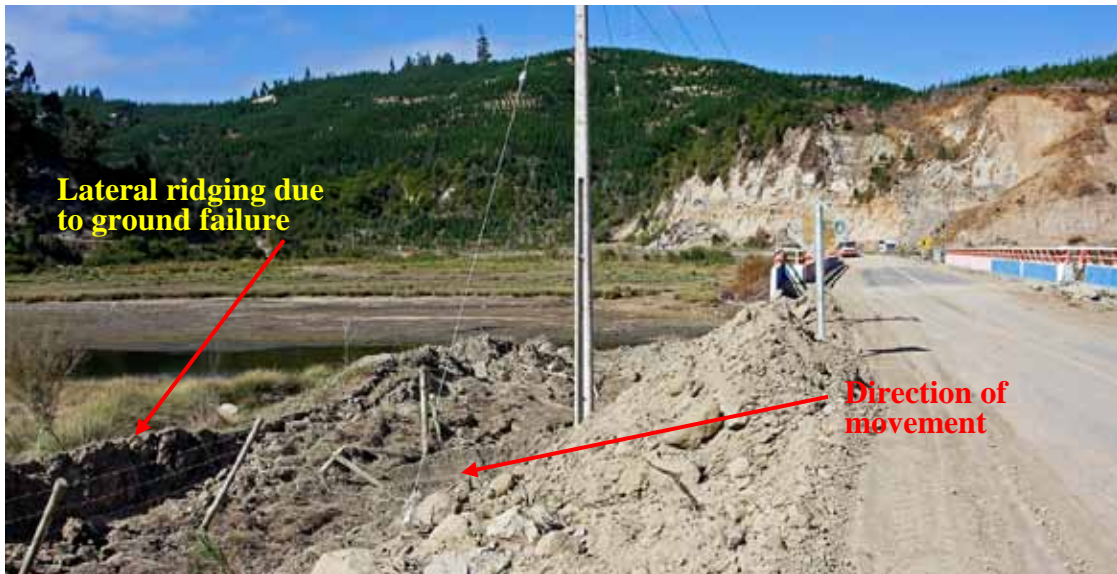


Figure 208. Photo. Evidence of ground failure perpendicular to roadway centerline at northwest approach of Raqui 1 bridge.

5.2.2.3.3 Llacolen Bridge (Site 17): Figure 195 illustrates another case where liquefaction obviously occurred (sand boils and evidence of minor lateral spreading). In this case, the southwest end of the Llacolen bridge, the liquefaction had very little impact on the bridge both in terms of foundation settlement and lateral movement of the foundations and abutment.

At the northeast end of the Llacolen bridge, the liquefaction impacts were far worse. The biggest problem for the Llacolen bridge, as well as for other Biobío River crossings and structures, was lateral movement of the foundations within the liquefaction-induced slope failure areas (see figure 209 for an overview of the river crossings and figure 210 through figure 213 for the Llacolen bridge). In general, most of the liquefaction-induced slope failure problems occurred along the northeast side of the river, where the river channel is incised more steeply. Very few liquefaction-induced problems occurred along the southwest side of the river even though there was clear evidence that liquefaction had occurred, probably due to the very flat ground conditions on that side of the river (see figure 195).



© Google, Inav/Geosistemas SRL, DMapas, and GeoEye

Figure 209. Map. Aerial view of Biobío River and crossings.



Figure 210. Photo. Evidence of slope instability due to liquefaction at northeast abutment and approaches of Llacolen bridge.

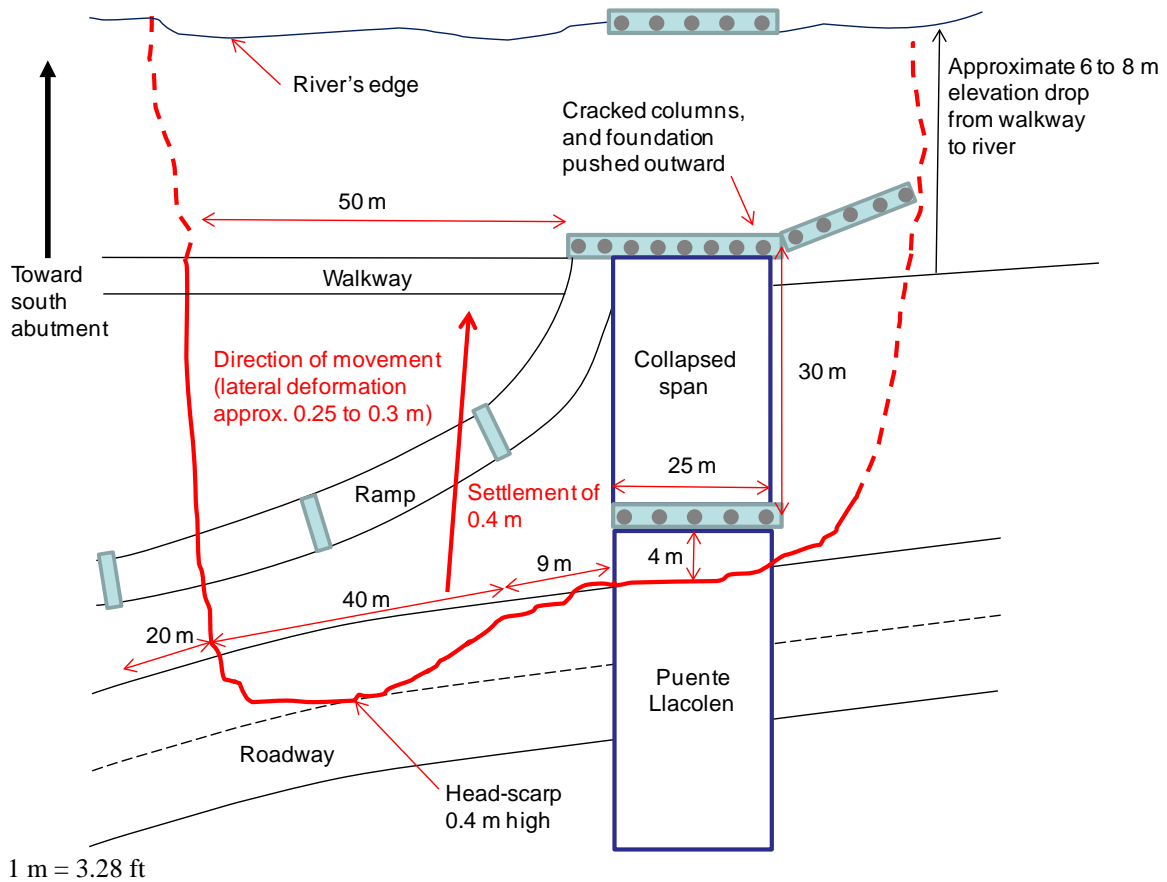


Figure 211. Illustration. Plan view of liquefaction-induced slide at northeast abutment of Llacolen bridge.



Figure 212. Photo. Settlement due to liquefaction-induced slope instability at northeast end of Llacolen bridge.



Figure 213. Photo. Settlement and lateral ground movement of interior pier at northeast end of Llacolen bridge.

At the northeast end of the Llacolen bridge, the liquefiable layer was probably near the river level. As the liquefiable layer weakened during shaking, the weight of the non-liquefiable soil caused the strength of the liquefied soil to be exceeded, resulting in a slope failure. As the soil moved laterally and downhill, it increased lateral stresses acting on the foundations, pushing them downhill and increasing bending stresses in the columns. The lateral movement caused a span to fall off its seat and collapse as well as excessive bending stresses to be placed on the pier columns, causing the columns to crack at a point of maximum stress in combination with weakness caused by a construction joint at that location. Similar observations and conclusions were made by the GEER team.⁽²⁾ This happened for several of the columns shown in figure 214 and figure 215. It is not completely clear whether the columns cracked as a result of lateral movement of the slope caused by liquefaction or if once the pier moved and the span fell, the impact of the falling span on the ground immediately behind the cracked columns was the final effect that cracked the columns. In either case, the lateral ground movement significantly increased the lateral stress on the bridge foundations and columns.



Figure 214. Photo. Lateral ground and foundation movement at interior pier and fallen span at northeast end of Llacolen bridge.



Figure 215. Photo. Close-up of cracked column at northeast end of Llacolen bridge.

The shaft foundations supporting the bridge were approximately 98 ft (30 m) deep and were probably bearing in dense soil. This kept the liquefaction settlement from dragging the foundations down, limiting the liquefaction impact to lateral movement of the foundations. This was not the case for the Juan Pablo II bridge, where shallower (59-ft (18-m)-deep) caisson foundations that

probably did not bear on dense soil were used. Foundation settlement did occur for the Juan Pablo II bridge, though only at specific piers (see discussion in section 5.2.2.3.5).

Additional photos and details regarding the Llacolen bridge and the impacts of liquefaction on that bridge are provided in GEER.⁽²⁾

5.2.2.3.4 Chepe Railroad Bridge Over Biobío River (Site 18): A railroad bridge built in 1889 near and parallel to the Llacolen bridge also suffered damage to one of its piers due to lateral movement and settlement caused by liquefaction in the vicinity of the northeast river bank. It appeared that the 7-ft (2-m)-diameter steel pipe pile concrete-filled foundation and column displaced laterally about 2 ft (0.7 m) and that the ground around the foundation settled approximately 4.3 ft (1.3 m) (see figure 177). The roadway that this bridge crosses also settled approximately 4.3 ft (1.3 m) and moved laterally approximately 1.6 to 2 ft (0.5 to 0.7 m), though the wall top also rotated inward towards the roadway (see figure 216). The wall itself appeared to settle only about 1 to 1.3 ft (0.3 to 0.4 m). The roadway and walls formed a seal to keep groundwater out of the roadway (see chapter 4 for additional details). The liquefaction-caused settlement broke that seal, which will need to be repaired before the river level rises. Even with so much deformation, these structures did not collapse despite being seriously damaged.



Figure 216. Photo. Wall settlement due to slope movement and instability caused by liquefaction at northwest end of Chepe railroad bridge.

5.2.2.3.5 Juan Pablo II Bridge (Site 25): Juan Pablo II bridge, another crossing of the Biobío River parallel to Llacolen bridge in Concepción, was built in 1973. This bridge was also impacted by liquefaction-induced slope failure as well as liquefaction-induced settlement and downdrag. The 1973 bridge foundations consisted of 59-ft (18-m)-deep hand-excavated caissons. Severe liquefaction-induced settlement of foundations occurred at several locations across the length of the bridge (1.6 ft (0.5 m) or more), but many of the piers exhibited no discernable settlement.

Notably, a shaft-supported wall supporting fill between the approach bridge and the main river-crossing structure settled very little, whereas the bridge approach pier settled more than 3 ft (1 m), and the soil surrounding the end of the wall and the bridge pier also settled more than 3 ft (1 m) (see figure 217 and figure 218). This difference is likely due to differences in the two structures and the amount of load they carry. It was noted that the shaft-supported wall is much newer than the bridge ramp structure and therefore may be designed to more stringent standards, as it is unlikely that the soil would be so vastly different over such a short distance. Figure 219 through figure 221 show the bridge settlement.



Figure 217. Photo. Settlement of approach structure for Juan Pablo II bridge.



Figure 218. Photo. Close-up of settlement of approach structure for Juan Pablo II bridge.



Figure 219. Photo. Roadway settlement due to settlement of approach structure pier foundations for Juan Pablo II bridge.



Figure 220. Photo. Roadway settlement due to settlement of mainline pier foundations for Juan Pablo II Bridge.



Figure 221. Photo. Liquefaction-induced differential settlement of mainline pier foundations supporting Juan Pablo II bridge.

The mainline Juan Pablo II Bridge abutment at the river bank suffered damage due to the lateral forces caused by liquefaction-induced slope instability. Figure 222 and figure 68 through figure 71 illustrate the damage that occurred. The damage to the column in figure 68 through figure 71 illustrates the severe bending stresses and lateral force to which the column was subjected when the northeast riverbank slope moved laterally due to loss of soil strength caused by liquefaction.

Although the bridge did not collapse due to these severe differential settlements and lateral slope movements, it was seriously damaged and efforts were already underway to design and build a replacement structure. Preparations for test hole drilling were being made during the TIRT visit.



Figure 222. Photo. Damage to pier columns for mainline Juan Pablo II bridge.

Note that GEER also provided a detailed account of reconnaissance of this structure and the damage that occurred due to liquefaction impacts. Additional photos and measurements for that structure are provided in GEER's report.⁽²⁾

5.2.2.3.6 Old Biobío River Bridge (Site 26): The old Biobío River bridge was built in the 1920s, replaced in 1943, and no longer in service at the time of the earthquake. Spans and some of its substructure units collapsed in the earthquake, probably due to a combination of inadequate structural resistance and shallow foundations (see figure 138, figure 223, and figure 224). Various types of deep foundations were used in various sections of the bridge. It appeared that pile foundations were used for the northeast half of the bridge, although it was not clear if all the original timber pile foundations used to support the 1920s structure were replaced with steel pipe piles in the 1943 replacement structure. Therefore, the northeast portion of the bridge could be supported by both timber and steel pipe piles. Based on input from a Chilean consultant, the piers near the southwest end of the bridge appeared to be supported by twin shaft foundations or twin hand-dug oval caissons (33 to 39 ft (10 to 12 m) deep, although it is possible that the foundations were tipped in relatively dense soils). Scour problems and deep liquefaction or soft soils that allowed more foundation movement during shaking may have contributed to the weakening and collapse of the structure, though the specific role of liquefaction in this collapse cannot be confirmed until more subsurface data becomes available. However, ground failure and lateral soil movement were observed at the bridge abutment for this structure on the northeast bank of the Biobío River, and the abutment pier wall appeared to be tilted toward the river (see figure 137, figure 225, and figure 226).



Figure 223. Photo. View of collapsed spans from northeast river bank of Biobío River.



Figure 224. Photo. Close-up of old Biobío River bridge showing exposed pile foundations.



Figure 225. Photo. Ground failure near northeast abutment of old Biobío River bridge.



Figure 226. Photo. Tilting of northeast abutment pier wall of old Biobío River bridge.

5.2.2.3.7 La Mochita Bridge (Site 27): Significant ground failure due to liquefaction also occurred at the La Mochita bridge, located beside the Biobío River just south of the three Biobío River crossings. The north approach fill to this structure and the soil surrounding the interior piers exhibited the most severe ground failure. Figure 227 through figure 229 show examples of the

north approach fill damage, and figure 196 and figure 197 show ground failure at the interior piers. The presence of ground water is a key ingredient for liquefaction to occur, and the ground water regime at this site was complicated by the presence of a dredging operation that pumped water from the river into a pit adjacent to the north approach fill, possibly raising the ground water levels in that approach fill (see figure 229). Seepage, possibly from water in the dredging spoils pit, was observed in the riverbank slope about 7 to 10 ft (2 to 3 m) above the river level in this area. This may have increased the severity of the ground failure observed in the north approach fill. However, the severity of the ground failure did not seem to be as great at the bridge abutment as it was 82–660 ft (25–200 m) north of the abutment (see figure 227 and figure 228). This may have been one of the reasons why the north bridge abutment was not significantly displaced due to this liquefaction-induced soil movement.



Figure 227. Photo. Ground failure of north approach fill for La Mochita bridge.



Figure 228. Photo. La Mochita bridge north approach fill liquefaction-induced ground failure.



Figure 229. Photo. La Mochita bridge north approach fill and edge of dredging pit.

Ground failure due to liquefaction at the bridge location was most obvious at the interior piers (see figure 196 and figure 197). While it appeared that the direction of movement was generally

eastward, away from the main river channel, the presence of reverse scarps and vertical movement of blocks of soil appeared to indicate the formation of a graben at and just west of the piers. This indicates that most of the ground movement at the interior piers was vertical with limited lateral movement. This may explain the relatively small lateral movement of the interior piers in spite of the apparently larger lateral slope movements. In any case, as can be seen in figure 197, the interior pier settled and tilted eastward, away from the river. The interior piers are believed to be supported on four 4.9-ft (1.5-m)-diameter drilled shafts, but this needs to be verified. Figure 230 shows the effect of the pier settlement on the elevation of the bridge deck.



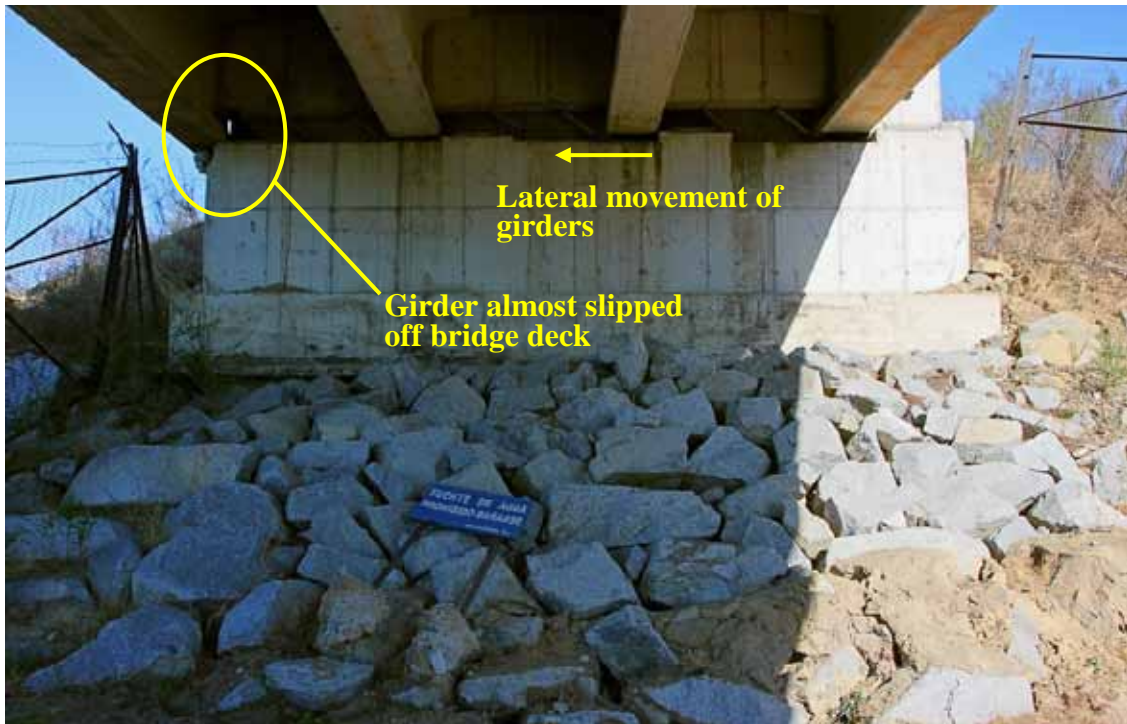
Figure 230. Photo. La Mochita bridge deck and girder lateral movement.

The bridge superstructure (girders and deck) also slid laterally toward the east up to 1 ft (0.3 m), with more movement at the south abutment than at the north abutment, possibly due to a combination of strong shaking and the tilting of the interior pier (see figure 230 through figure 232). It appeared that the abutments did not move. Note that one of the outside bridge girders almost slipped off the abutment seat (see figure 232). Overall, while the ground failure was significant (lots of movement with a thick non-liquefied crust), this bridge did not collapse. However, it was laterally displaced and suffered damage.



Lateral bridge deck movement

Figure 231. Photo. La Mochita bridge deck and girder lateral movement and approach fill settlement.



Lateral movement of girders

Girder almost slipped off bridge deck

Figure 232. Photo. La Mochita bridge lateral bridge deck and girder at south abutment.

Additional observations and measurements regarding the ground failure and bridge movements, including photos, are provided in GEER. The overall conclusions made by GEER are consistent with the observations of TIRT.⁽²⁾

5.2.2.3.8 Raqui 2 and Tubul Bridges (Sites 21 and 22): Examples of severe bridge damage due to liquefaction combined with inadequate structural resistance include the Raqui 2 and Tubul bridges. For the Raqui 2 bridge, damage caused by liquefaction included severe failure and large-scale settlement of the approach fills (see figure 198 and figure 233) and collapse of the interior bridge spans resulting from movement and tilting of the interior pier foundations (see figure 234 and figure 235). It was not clear if the lateral displacement of the interior piers was due to some type of lateral soil movement or permanent displacement due to the combination of weak liquefied soils and lateral inertial forces induced by shaking of the bridge superstructure. Even though severe failure of the abutment fills occurred (likely due to liquefaction), it appeared that the abutments themselves did not move significantly. Based on the lateral ridging observed along the approach fill side slope toes and the roadway cracking pattern, it appeared that most of the lateral soil movement was in the direction perpendicular to the roadway centerline, which could explain why the abutments did not appear to have moved laterally.



Figure 233. Photo. Southeast approach fill damage at Raqui 2 bridge.



Span has shifted to left (SW) while pier wall did not move

Figure 234. Photo. Collapsed and shifted spans at Raqui 2 bridge as viewed from base of southeast abutment.



Tilted substructure pier (may have tilted during shaking due to liquefaction or when span fell)

Figure 235. Photo. Collapsed and shifted spans at Raqui 2 bridge due to liquefaction.

Damage caused by liquefaction for the Tubul bridge was similar to that observed at the Raqui 2 bridge, though more lateral movement of the abutments due to lateral spreading forces appeared to have occurred. Ground cracking and deformation indicative of lateral spreading toward the river

was observed at both ends of the bridge. Damage observed included liquefaction-induced ground failure, large-scale settlement of the approach fills (see figure 236 through figure 240), and shoving of the bridge girders approximately 5.9 inches (150 mm) into the north abutment, resulting in some crushing of the abutment wall at the girder locations (see figure 240 and figure 115). The south abutment pile cap was also damaged (see figure 239). It is possible that the north abutment was pushed into the girder to cause the abutment wall crushing. Alternatively, the girders supported by the interior piers could have been shoved into the north abutment due to a combination of lateral movement of the south abutment and strong shaking (see chapter 4).



Figure 236. Photo. South approach fill damage and collapsed spans at Tubul Bridge.



Figure 237. Photo. Settlement of fill beside the south abutment of Tubul bridge.



Figure 238. Photo. Overview of damage to south abutment of Tubul bridge.



Figure 239. Photo. Close-up of exposed pile and pile cap damage on south abutment of Tubul bridge.



Figure 240. Photo. Overview of Tubul bridge north abutment.

The exposed pile cap of the Tubul bridge south abutment was obviously damaged, possibly due to lateral movement toward the north (see figure 239). It is not clear if the exposed timber pile was embedded in the pile cap as part of the abutment foundation or was a remnant of a foundation from an older bridge that ended up getting included in the pile cap when it was constructed. Specific foundation details for this bridge were not available, although it is likely that this bridge was supported on piles. In any case, it appears that the presence of the timber pile in combination with lateral movement of the abutment due to lateral spreading forces may have forced the exterior concrete pile cap to break and come loose. Additionally, the approach fill settlement and lateral movement appeared to be more severe at the south abutment than at the north abutment, providing further support that the collapse may have initiated at the south end of the bridge. Regarding the interior piers of the Tubul bridge, damage or collapse of the pier walls appeared to be the primary problem. The pile caps appeared to not have moved, at least in the lateral direction. However, some of the pile caps were not visible (they were under water or mud) and therefore could have settled or moved laterally (see figure 241).



Figure 241. Photo. Tubul bridge collapsed spans and substructure.

The age of these bridges, the subsurface conditions, and the foundation details were not available to TIRT. Therefore, additional investigation is needed to more accurately assess the observed bridge performance.

5.2.2.3.9. Puerto de Coronel Muelle (Site 19): Deep liquefaction combined with lateral soil movement can cause severe foundation element bending. This was exemplified at the Puerto de Coronel Muelle, located south of Concepción but north of Arauco. The foundations supporting the pier (wharf) structure were pushed laterally and displaced (see figure 242 and figure 243). Since the foundations were deep (steel 28- to 40-inch (711 to 1,016 mm) open-ended pipe piles driven to a depth of approximately 160 ft (50 m)), the piles were probably fairly well fixed near the bottom. Based on the boring logs available, loose sands are present in the top 49 to 66 ft (15 to 20 m) below the ground surface. Therefore, liquefaction likely occurred to significant depth and contributed to the foundation displacements and degrees of bending observed. The yellow line in figure 243 traces the bending and twisting observed in the girder that was attached to the pile foundation. See GEER for additional details regarding the effect lateral spreading had on these and similar structures in the vicinity.⁽²⁾



Figure 242. Photo. Puerto de Coronel Muelle foundation displacement and bending.



Figure 243. Photo. Close-up of Puerto de Coronel Muelle foundation displacement and bending.

5.2.2.4 Summary of Liquefaction Performance for Bridges and Other Structures: In summary, the primary effects of soil liquefaction on bridges and pier structures included foundation and approach fill settlement, loss of lateral foundation support, and lateral foundation movement due to lateral spreading and liquefaction-induced slope failure. Foundation settlement in particular was highly variable, ranging from 0 to 3 ft (0 to 1 m) or more, even for piers that were next to each other (e.g., Juan Pablo II bridge). Foundation settlement depends not only on the thickness of non-liquefiable crust (affecting downdrag unit friction on the foundations) and thickness of liquefiable soil (affecting magnitude of soil settlement) but also on the ability of the soil at the foundation tips to resist deformation and provide the needed bearing resistance. Note that even with such severe differential settlement, bridge collapse did not occur.

Lateral displacement of abutment walls and interior piers appeared to occur primarily when a significant crust of non-liquefied soil slid on top of a liquefied soil layer and when the slope was wide enough to significantly reduce or eliminate three-dimensional effects. Table 5 summarizes the approximate slope geometry and performance of bridge abutments and interior piers. The table entries are in general order of increasing severity of soil and structure movements and damage. The information in the table demonstrates that abutments that form the terminus of a long, narrow fill tend to be mostly unaffected by liquefaction and lateral ground movement, assuming that the abutment is supported by a reasonably robust foundation. In general, site observations confirmed that most of the soil movement was perpendicular to the roadway fill centerline and not directly into the abutment wall. Overall, bridge abutments did well in this earthquake, even when liquefaction and resulting ground settlement or failure was severe. However, where the bridge abutment, interior pier, or pier structure foundations were located on a broader slope such as would occur adjacent to a river or ocean waterfront, liquefaction-induced ground failure and lateral soil movements did result in lateral displacement or overstress and failure of the foundations and substructure. A possible reason for this difference in performance is the ability of the soil to either flow around the foundations or to otherwise follow the path of least resistance or greatest driving force. This depended on the thickness and fluidity of the failed soil mass and the slope and bridge geometry. The greatest driving force is likely to be in the direction where three-dimensional effects have the smallest influence and smallest contribution to the resistance to movement.

Table 5. Summary of performance for abutments and interior piers on slopes affected by liquefaction-induced ground movement or settlement.

Site No., Name, and Abutment/Pier Location	Estimated Abutment or Slope Height	Estimated Ground Geometry at Abutment/Pier Vicinity	Observed Abutment/Pier Deformation and Performance
17. Llacolen bridge, SW abutment and land side piers	1 to 2 m	~ 3-degree slope (see figure 195)	No movement or significant damage
20. Raqui 1 bridge, SE abutment	3.5 m	Two-lane approach fill on gently sloping ground (see figure 207)	No movement/significant damage to abutment. 1 m of approach fill settlement and lateral spreading perpendicular to the roadway centerline.
15. Mataquito bridge, both abutments	7 to 8 m	Gently sloping to river (~ 5 degrees) (see figure 192, figure 193, and figure 202 through figure 204)	NE abutment shows minor crushing on abutment wall. If lateral movement occurred, it was less than 20 mm. SW abutment did not move
27. La Mochita ridge, both abutments	9 to 12 m transverse to abutment toward river	Steeply sloping (~ 25 degrees) to river transverse to bridge abutment wall; rip-rapped ~ 25-degree slope below abutment to river-level north abutment and to 3 to 4 m high ridge below bridge centerline at south abutment (see figure 197 and figure 228 through figure 232).	No abutment movement or significant damage; fill settlement at abutments varied from 0.3 m to 0.8 m. Lateral movement of approach fills perpendicular to roadway centerline.
20. Raqui 1 bridge, NW abutment	4 m	Moderately sloping to river (~ 7-degree slope) (see figure 207)	Abutment fill settled about 1 m. Abutment may have moved laterally 75 to 100 mm and twisted. Small adjacent wall parallel to abutment wall tilted and moved laterally.
27. La Mochita bridge, interior pier	3 to 5 m	Ground slopes perpendicular to bridge centerline and away from main river channel (see figure 197)	Pier moved laterally about 100 to 150 mm, and vertically about 50 to 100 mm. Movement was down slope away from Biobío River main channel.
19. Puerto de Coronel Muelle, pier on sloping shoreline	4 to 5 m	General slope toward ocean at ~ 10 degrees	Pile foundations moved laterally down slope about 0.5 to 0.7 m.
21. Raqui 2 bridge, both abutments and interior piers	4 m	Two lane approach fill on gently sloping ground (see figure 198, figure 233, and figure 234)	No abutment movement but some minor damage, approach fill settlement up to 1.5 m, and lateral spreading perpendicular to the roadway centerline. Interior spans collapsed and piers tilted laterally.
18. Chepe railroad bridge over Biobío River, NE river bank pier	7 to 8 m	Pier located at top of river bank; geometry is complex (see figure 176 and figure 216)	Pier moved laterally 0.7 m; ground around pier settled 1.3 m.
26. Old Biobío River bridge, NE abutment and interior piers	6 to 7 m	Abutment on river bank slope (~ 25 degrees) (see figure 225 and figure 226)	Abutment wall tilted down slope about 150 mm. Direction of ground movement is toward river. Some interior piers collapsed.
17. Llacolen bridge, pier on slope below NE abutment	5 to 6 m at 20-degree slope, then less than 10 degrees with 2-m drop to river edge	Ground slopes down to river (see figure 210 through figure 214)	Pier on river bank moved laterally about 0.25 to 0.3 m and vertically about 0.3 to 0.4 m, causing columns to crack all the way through and approach span to move off bridge seat and collapse.

See notes at end of table

Site No., Name, and Abutment/Pier Location	Estimated Abutment or Slope Height	Estimated Ground Geometry at Abutment/Pier Vicinity	Observed Abutment/Pier Deformation and Performance
22. Tubul bridge, north abutment and interior piers	4.5 to 5 m	Fill behind abutment extends out from edges of bridge (wider than needed for two lanes); slope is 25 to 30 degrees (estimated) then flattens to 10 degrees or less in short section to river (see figure 240)	Abutment may have moved laterally about 150 mm, but it is also possible that girders were shoved into abutment due to a combination of pier wall failures, strong shaking, and lateral movement of south abutment. Approach fill settled over 1 m. Interior piers collapsed.
22. Tubul bridge, south abutment	5 m	Two-lane approach fill on ~ 10-degree sloping ground (see figure 236 through figure 240)	Approach fill settled up to 1.5 m with lateral spreading primarily perpendicular to the roadway centerline, but turning toward river away from the abutment. Front of pier cap was damaged at timber pile location, possibly due to lateral abutment movement of 100 mm or more. Interior spans collapsed.
25. Juan Pablo II bridge, pier on slope below NE abutment	6 to 7 m	Pier is located mid-slope; slope drops steeply to river (~ 30 degrees) (see figure 222 and figure 68 through figure 71)	Pier column on river bank slope moved laterally 0.3 m or more and column failed, but span did not collapse. Interior piers suffered severe differential settlement of up to 1 m.

1 m = 3.28 ft

1 mm = 0.039 inches

The current design philosophy in North America is to stabilize bridge abutments to prevent liquefaction, especially for the case of bridge abutments that form the terminus of relatively long approach fills not located on top of a broader slope (e.g., a riverbank). This design philosophy may be overly conservative and costly if large approach fill settlement can be tolerated for a no-collapse scenario. The approach fills can be simply and quickly rebuilt, as was done at several bridges observed by TIRT. It appeared that three-dimensional effects had a significant impact on the stability and movement of bridge abutments and piers subjected to liquefaction. Of course, these conclusions about liquefaction effects are preliminary until more subsurface and structure/slope geometry data are available and analyzed. The conclusions provided herein are based on surficial observations, limited information about the subsurface conditions, and limited or visually estimated ground slope geometry.

5.2.3 Effect of Regional Ground Uplift Observed for Bridges

As discussed in chapter 2, one result of subduction zone earthquakes is regional uplift and subsidence. The effects of regional uplift were especially prevalent south of Concepción, in the vicinity and south of Arauco, where regional uplift of approximately 7 ft (2 m) was observed. This especially affected harbors and waterways, leaving ships on sand and gravel bars. It also left beaches, estuaries, and wetlands without the water necessary to support plant and aquatic life. Fishing villages that had close access to navigable waterways lost access, requiring new access ways to be built.

Examples of the impact of rapid uplift are shown in figure 244 and figure 245. These figures show dry ground that was once wet and boats hung up on old timber pilings that were once almost fully submerged. However, the team was not able to confirm that these boats ended up on the pilings as the result of the earthquake. Figure 117 shows additional evidence of the pre-earthquake water level. One possible effect of the rapid uplift was to create rapid drawdown conditions, increasing the instability of sloping ground that was once partially or fully underwater. These remnant pore pressures could have combined with liquefaction effects to further decrease the stability of affected slopes, making them more likely to fail and to experience greater lateral deformations. This scenario needs further study once more subsurface data is obtained. The effect of rapid uplift on the bridge itself is unknown at this point. However, if the rapid uplift created the potential for differential movement between piers, the rapid uplift could have created additional problems for a bridge already in distress due to strong ground motions and liquefaction-induced forces or loss of foundation support. These near-fault effects need further consideration.



Figure 244. Photo. View northeast from Tubul bridge south abutment showing areas left dry and boats left above the new mean water level.

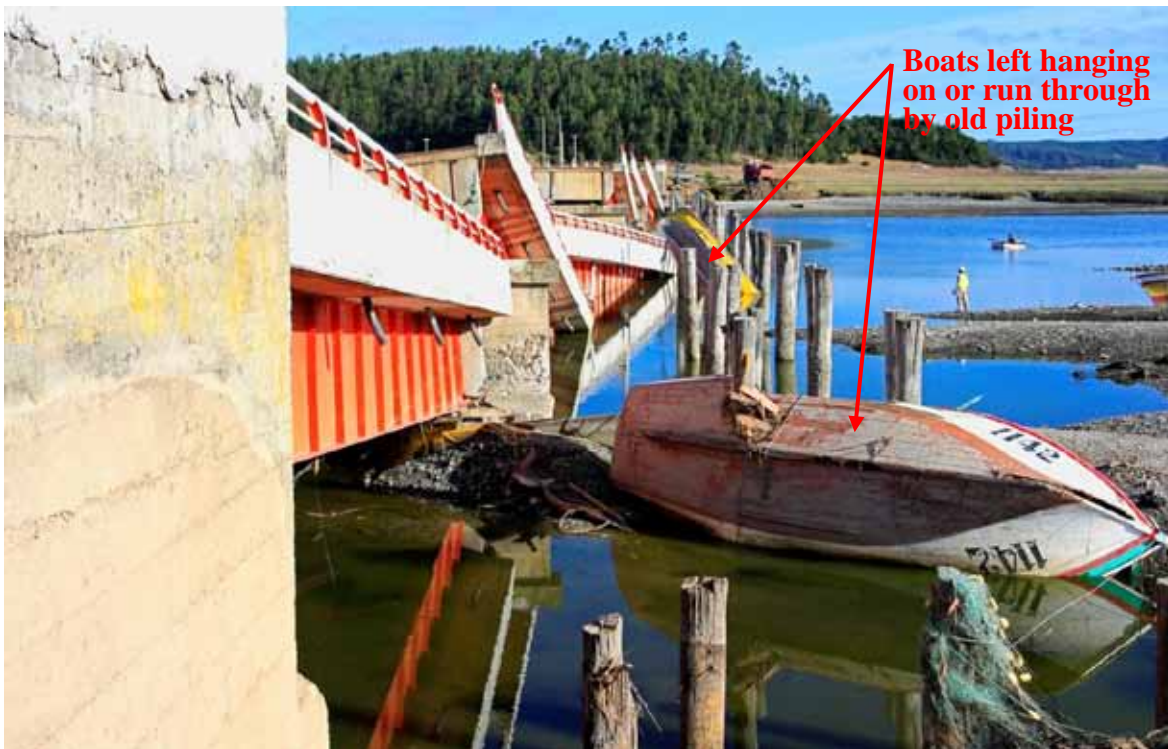


Figure 245. Photo. Tubul bridge with boats run through by old timber pilings.

5.3 GEOTECHNICAL OBSERVATIONS REGARDING RETAINING WALL PERFORMANCE

In general, walls have performed very well in past earthquakes. Examples include soil nail walls and mechanically stabilized earth (MSE) walls in the 1989 Loma Prieta earthquake in California, MSE walls in the 1994 Northridge, CA, earthquake, and MSE walls and modern reinforced concrete gravity walls the 1995 Kobe, Japan, earthquake. (See references 15–18.) Koeski, et al. provide a summary of the performance of various types of walls, focusing on geosynthetic reinforced structures, in these and more recent earthquakes.⁽¹⁹⁾ The largest earthquakes have shown some differences in performance between relatively rigid walls such as concrete gravity walls and more flexible, MSE-type walls, with the MSE type structures tending to outperform the concrete gravity structures, especially older concrete gravity structures. While some damage to walls has occurred in past earthquakes, the damage has typically included minor movement (4 inches (100 mm) or less) or outward tipping of the wall, cracking of wall facing elements, wall corners or full-height joints opening up and allowing backfill to spill through, unsecured blocks at the wall top toppling off, and on rare occasions, collapse. Instances of wall collapse in past earthquakes were almost always limited to older walls that would not meet current design standards (especially unreinforced masonry and concrete walls) and, in a few cases, newer walls that were not designed to standards or were already in serious distress before the earthquake due to design or construction problems.

This section presents observations regarding the performance of retaining walls. Many of the 32 sites visited had bridge embankment approaches that were either sloped embankments or retaining walls. In addition, many sites used retaining walls to confine the soil under the bridge abutment. For the most part, the retaining walls observed consisted of either CIP concrete cantilever walls or MSE walls. The MSE walls observed were constructed of either precast panels with metallic reinforcement or dry cast modular blocks with geosynthetic reinforcement.

Traditionally, CIP walls have been used to confine the approach fill near a bridge abutment. MSE construction is a newer technology that has been used around the world since the 1960s as an alternative to CIP walls. The advantage of MSE walls include cost, rate of construction, and tolerance to settlement. In Chile, MSE walls have been used since 1995 (site 28 includes the first MSE walls built in Chile). The team observed a combination of CIP and MSE walls at many of the sites visited. In most cases, MSE walls were only used to retain the embankment approaches and not under the abutment. Under the abutment, CIP concrete walls were typically used. Table 6 lists the sites where retaining walls were observed and includes brief descriptions. Figure 246 through figure 260 show photos of each of the walls.

Table 6. Summary of sites with retaining walls.

Site No.	Site Name	Wall Description	Wall Height (m)
1	Américo Vespucio/ Miraflores	MSE wall (steel reinforcement, precast panel faced) approaches with CIP abutment wall	6 to 7
2	Américo Vespucio/ Lo Echeveres	MSE wall (steel reinforcement, precast panel faced) approaches with CIP abutment wall	6 to 7
3	14 de la Fama	MSE wall (steel reinforcement, precast panel faced) approaches with CIP abutment wall	6 to 7
5	Quilicura railway overcrossing	CIP concrete abutment and approach walls	5 to 6
6a	Américo Vespucio/ Independencia eastbound	MSE wall approaches with CIP abutment walls, both precast panel with steel reinforcement and modular block with geogrid reinforcement	6 to 7
6b	Américo Vespucio/ Independencia westbound	CIP concrete back-to-back semi-gravity walls for approach ramps	6 to 7
9	Maipú River bridge	Concrete block gravity wall	9 to 11+
11	Estribo Francisco Mostazal (Avenida Independencia)	MSE (modular block and geogrid reinforcement) abutment walls. Walls directly support abutment loads from the bridge.	6.5 to 7.5
18	Chepe railroad bridge over Biobío River	CIP concrete wall supporting cut for depressed roadway	5
21	Raqui 2	Approach ramps use CIP walls for the embankment and abutment	4
25	Juan Pablo II	Shaft-supported CIP walls retaining embankment fills	2 to 3
28	21 de Mayo	MSE wall (steel reinforcement, precast panel faced) approaches and CIP abutment walls	8 to 10
29	Rotonda General Bonilla	MSE wall (modular block face with geogrid reinforcement) approaches and CIP abutment wall	4.5 to 5
32	Muros Talca (SW)	MSE wall (modular block facing and geogrid reinforcement) approaches and CIP abutment wall	8 to 9.5

1 m = 3.28 ft



Figure 246. Photo. Retaining wall at Américo Vespucio/Miraflores.



Figure 247. Photo. Retaining wall at Américo Vespucio/Lo Echevers.



Figure 248. Photo. Retaining wall at 14 de la Fama.



Figure 249. Photo. Retaining wall at Quilicura railroad overcrossing.



Figure 250. Photo. Retaining wall at Américo Vespucio/Independencia eastbound.



Figure 251. Photo. Retaining wall at Américo Vespucio/Independencia westbound.



Figure 252. Photo. Retaining wall at Maipú River bridge.



Figure 253. Photo. Retaining wall at Estribo Francisco Mostazal (Avenida Independencia).



Figure 254. Photo. Retaining wall at Chepe railroad bridge over Biobío River.



Figure 255. Photo. Retaining wall at Raqui 2.



Figure 256. Photo. South retaining wall at Juan Pablo II.



Figure 257. Photo. North retaining wall at Juan Pablo II.



Figure 258. Photo. Retaining wall at 21 de Mayo.



Figure 259. Photo. Retaining wall at Rotonda General Bonilla.



Figure 260. Photo. Retaining wall at Muros Talca (SW).

In general, all of the observed retaining walls performed well. There was little to no wall movement or damage, with the exception of sites 6, 18, 25, 28, and 32. Other than these sites, the wall facing, top-of-wall details, pavement, and other ancillary components showed no signs of distress due to the earthquake, even though some of the bridges associated with these walls experienced significant damage or even complete collapse of the superstructure. Although the retaining walls at sites 6, 18, 25, 28, and 32 experienced deformations or damage, they continued to perform their function of retaining soil and maintaining a grade separation. It is expected that these walls could be rehabilitated and placed back into service. A specific description of the problems observed at these five sites and their probable causes are provided in the paragraphs that follow.

The retaining walls at Américo Vespucio/Independencia (site 6) performed very well except for the detailing at the top of the modular block walls. The top two to three block layers and the cap block appeared to have been placed as a parapet above the ground surface at the wall top to hide a surface water drainage ditch (see figure 261). These blocks were unsupported and therefore only had self weight and the connection system to resist the horizontal loads. The horizontal force generated due to the earthquake and possibly from the concrete barrier behind the drainage ditch pushed the blocks and caused them to topple.

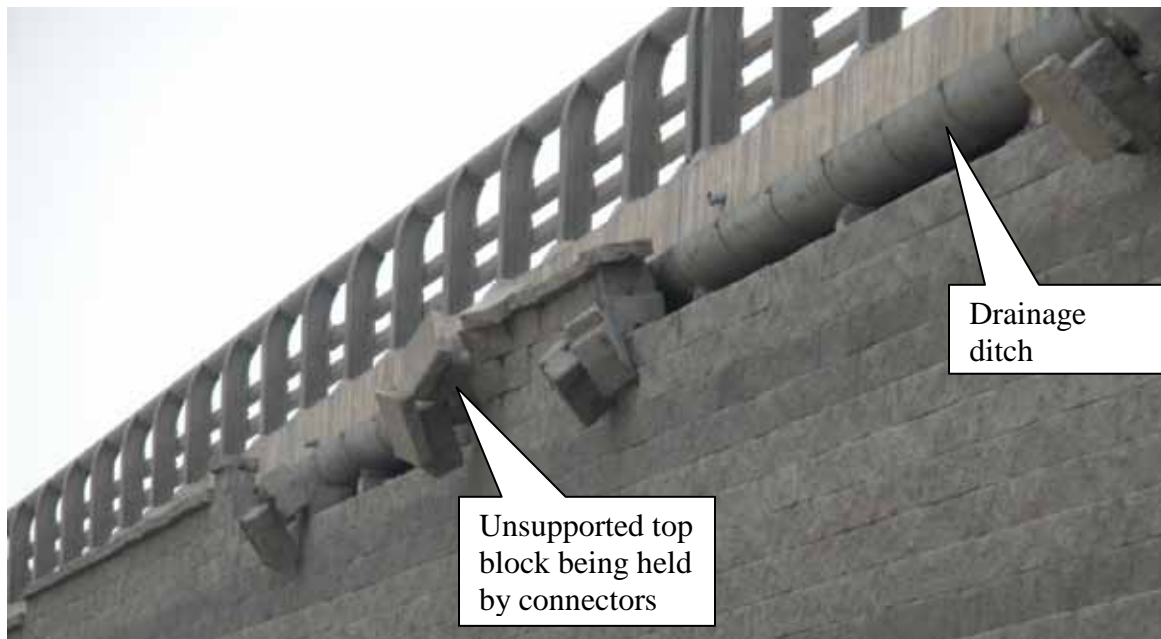


Figure 261. Photo. Toppling of coping at Américo Vespucio/Independencia.

The Chepe railroad bridge over the Biobío River (site 18) is a complex system, as shown in figure 176. A CIP cantilever wall supports a cut to form a depressed roadway. The ground water level is above the depressed roadway elevation at times, depending on the water level in the river. In effect, the roadway and walls in this section form a tub to keep the ground water out of the roadway. The soil below and behind the wall settled and moved toward the river, probably due to liquefaction-induced slope failure (see figure 262 and figure 263). This condition is consistent with observations at other sites along this side of the Biobío River. Due to the liquefaction-induced soil movement, the wall moved downward approximately 1 to 1.3 ft (0.3 to 0.4 m) and the top of wall rotated into the depressed roadway section. Furthermore, the seal between the roadway and wall was broken, which will allow water into the depressed roadway when the river rises.



Figure 262. Photo. Wall movement near Chepe railroad bridge due to lateral spreading and settlement.



Figure 263. Photo. Wall settlement and rotation due to lateral spreading and settlement.

While the wall was in immediate need of repair, it is notable that the wall was still performing its function of retaining the soil from impacting the depressed roadway despite the severe movement caused by liquefaction. This demonstrates that even in the severe case of liquefaction below the wall, the wall can still function and not collapse. Note that the temporary support of the bridge superstructure placed after the earthquake may be contributing to the lateral loading of the wall. This indicates that even though the wall was damaged, it has some reserve capacity.

The approach for the Juan Pablo II bridge (site 25) was discussed in section 5.1 and illustrated in figure 217 through figure 219. In addition to bridge damage, there were two CIP walls retaining the embankment fill between bridge spans (identified as north and south walls in figure 256, figure 257, figure 264, and figure 265). The embankment between bridge spans settled due to

liquefaction, and the bridge pier near the south wall also settled approximately 3 ft (1 m). The slopes in front of these walls moved laterally, likely due to liquefaction (see figure 200 and figure 201). It appears that the north wall and the embankment settled together more than 3 ft (1 m). Although the soil in front and behind the south wall settled, the wall itself did not settle because it was founded on deep foundations. This wall was built during a later construction project that added the entrance and exit ramps heading east. The north wall was completed in the original construction. Both walls continue to perform as intended after the earthquake, though the north wall would likely need to be replaced to raise the roadway back to its original grade.



© Google, GeoEye, and DMaps

Figure 264. Map. Retaining walls near Juan Pablo II bridge.



Figure 265. Photo. Wall settlement near Juan Pablo II bridge due to liquefaction-induced settlement.

The retaining walls at Vía Elevada 21 de Mayo (site 28) are a combination of MSE walls used to retain approach and embankment fills and CIP concrete abutment and curtain walls. These walls were built in 1995 and are probably the first MSE walls built in Chile. These MSE walls were used as a substitute for CIP concrete walls included in the construction contract through a value engineering proposal made by the contractor prior to construction.

The MSE walls are composed of precast concrete panel facing and steel bar mat soil reinforcement. There are a total of five walls on this site, and with the exception of the wall corners and full-height joints between the MSE walls and the curtain walls, they performed very well.

Three wall locations within Vía Elevada 21 de Mayo experienced deformation and are highlighted in this discussion (see figure 266). All three wall locations exhibited damage associated with wall top, full-height joint, and corner details. Corner details for MSE walls are an issue because they tend to attract seismic loads and ensuring that the joint will stay together can be difficult. The performance issues were primarily with the joints opening up and fill escaping. Both bridges associated with the walls at this site also experienced damage but did not collapse. However, an older bridge parallel to these bridges did collapse.



© Google, GeoEye, DMapas, Inav/Geosistemas SRL, and Europa Technologies

Figure 266. Map. Vía Elevada 21 de Mayo.

Based on the design calculations available, the MSE walls at this site were designed using a horizontal acceleration coefficient of 0.4 g and were designed in general accordance with the AASHTO Standard Specifications available at that time. The high acceleration coefficient used to design these walls was a bit surprising because the official implementation of the 0.4 g ground acceleration for coastal areas did not occur until 2002. It is not known if the adjacent bridges were designed for 0.4 g. Based on the wall calculations, the soil reinforcement length used was approximately 90–100 percent of the wall height, likely the result of using a 0.4 g acceleration coefficient. The corner and full-height joints where the walls connected to the bridge curtain walls were not designed as robustly for connectivity between adjacent panels as would typically be done today; this appears to have contributed to the performance problems observed.

Wall site 28A is a 30-ft (9-m) wall tiered perpendicular to the road alignment (see figure 267). The wall appears to have rotated out, allowing backfill to escape out of the reinforced fill at the full-height joint between the curtain wall and the MSE wall. Potential issues could be related to

inadequate soil reinforcement embedment lengths or poor placement and compaction of fill due to the tight geometry caused by the presence of the wall corner, abutments, and foundation elements. The uniform rounded nature of the sand backfill used (a coefficient of uniformity of less than 2 based on available laboratory test data on the backfill) may also have contributed to reduced pullout resistance, especially during shaking. Based on eye-witness accounts of the wall construction in 1995, the backfill soil was extremely difficult to compact to a firm condition because of the uniform nature of the soil. Although tiered walls are aesthetically pleasing and can help reduce stress on the lower portion of the wall, the use of such complex wall geometry can lead to poor performance if not designed, detailed, and constructed correctly.



Figure 267. Photo. Tiered wall corner tilting outward at wall site 28A.

Wall site 28B, a 33-ft (10-m)-high wall, is similar to wall site 28A in that the wall rotated outward, although not as severely (see figure 268). The cause of the problem is also similar to wall site 28A, a combination of inadequate soil reinforcement embedment due to the severe bridge skew (the acute enclosed angle between the abutment wall and MSE wall is approximately 25 degrees) and the use of uniform rounded sand. The combination potentially resulted in reduced pullout resistance, especially near the wall top where soil confining stress is relatively low, and in lack of a positive connection at the full-height joint between the curtain wall and the MSE wall panels. Modern technique to design such acute corners is to create a bin structure, making sure that the soil reinforcement is tied across to both sides of the acute angle. Since that was apparently not done, the soil reinforcement near the acute corner was too short, allowing pullout failure to occur and the panels to move during the earthquake.



Figure 268. Photo. Wall corner tilting outward at wall site 28B.

The deformation at wall site 28C was the most severe of the three (see figure 269 through figure 272). Similar to wall site A, the wall is tiered, but instead of rotating, the lower wall slid and rotated, moving laterally outward near the lower wall top approximately 1 to 1.3 ft (0.3 to 0.4 m) (see figure 269) and possibly 0.49 to 0.7 ft (0.15 to 0.2 m) near the wall base (estimated based on tilt of wall face). This is the only wall observed by TIRT that exhibited signs of translational movement, with the exception of the wall at site 18 that moved laterally due to liquefaction-induced lateral spreading of the soil it retained. Because the upper tier was founded on the fill of the lower tier, the upper tier moved downward once the fill retained by the lower wall spilled out through the gap between the lower wall and the curtain wall. Figure 270 shows the back side of the upper wall, where the loss of the fill exposed the soil reinforcement behind the panels. The reinforcement, panel connection, and lack of geotextile between the MSE wall and curtain wall can be seen. The function of the geotextile is to prevent fill from escaping through the joint. In this case, the gap was probably too large for the geotextile to keep the fill from spilling. The geotextile was used at the panel-to-panel joints. The movement of the corner panels was observed at the other corners of these walls, although to a lesser degree.



Figure 269. Photo. Lateral movement of lower wall top at wall site 28C.



Figure 270. Photo. Back side of upper wall at wall site 28C.



Figure 271. Photo. Fill material from tiered wall at wall site 28C.



Figure 272. Photo. Differential settlement at wall site 28C.

As shown in figure 271, the fill was a uniform medium-coarse sand with an angle of repose of approximately 32 degrees. This type of material may have contributed to poor soil-structure interaction with the reinforcement. If this was not considered in the wall design, it may have caused a lower pullout resistance than anticipated.

Figure 272 shows the wall at the opposite abutment. In this case, the wall appears to have differentially settled, causing the panels to shift and separate and allowing some backfill soil to spill out.

The specific cause of the excessive lateral movement and differential settlement at this location may have been the liquefaction of the loose sandy soil below the wall. The available borings at the site indicate that the water table is approximately 7 ft (2 m) below the ground surface and loose, liquefiable sand extends to a depth of approximately 16 ft (5 m) (see appendix A). Soft organic silt extends another 3 to 7 ft (1 to 2 m) below the loose sand, below which the sands become dense to

very dense. What appeared to be ejected sand (sand boils) was present near these walls as was some localized ground cracking and cracks in the roadway pavement, as shown in figure 273. With regard to lateral movement on the lower wall, the width of the reinforced soil zone (approaching 100 percent of the wall height) was likely more than adequate to resist the seismically induced lateral earth pressures behind the wall. Therefore, liquefaction is the most likely explanation for the lateral movement. During wall construction, 7.8 inches (200 mm) of settlement of the walls and fill occurred due to the loose sand and organic silt layer below the walls. Construction photos of the walls show what appear to be gaps in the panels that were likely caused by differential settlement that occurred during construction. However, it is also likely that liquefaction settlement below the wall may have worsened the panel distortion.



Figure 273. Photo. Possible liquefaction features near wall site 28C.

The Muros Talca site (site 32) consists of four geogrid reinforced modular block MSE walls approximately 30 ft (9 m) high with a 1.5H:1V to 2H:1V unreinforced slope on top. The MSE walls abut to a CIP concrete abutment wall. A plan view of the bridge and walls is provided in figure 274. The northeast corner wall experienced severe cracking of the facing blocks and an outward lateral deformation of approximately 4 inches (100 mm). The face block cracking pattern is shown in figure 275 and figure 276, with a linear distribution of the cracks on a 45-degree angle. The southwest corner also had some cracked blocks with a similar pattern but to a much lesser degree. This appears to be another example of a wall corner (or very tight radius in the wall alignment) having problems resisting seismic loading. The significant wall height, especially for a vertical wall, puts a lot of demand on the blocks even for static loading. Combining the wall height plus soil surcharge with a tight radius in the wall alignment and severe seismic loading

caused a severe demand on the facing blocks. Some additional evaluation of this wall is needed to fully understand the effect that seismic loading had on this wall and the mode of facing failure. However, even though the wall facing was sheared by the demands placed on it, the wall did not collapse and is still functional, though facing repair will be needed.

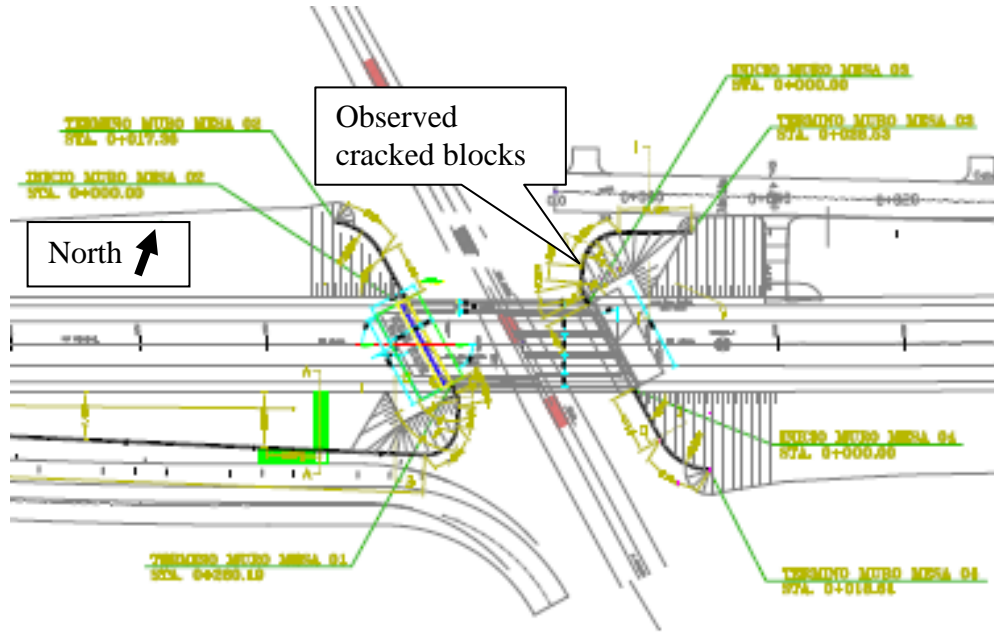


Figure 274. Illustration. Plan view of wall at Muros Talca.



Figure 275. Photo. Wall with steep top slope at Muros Talca.

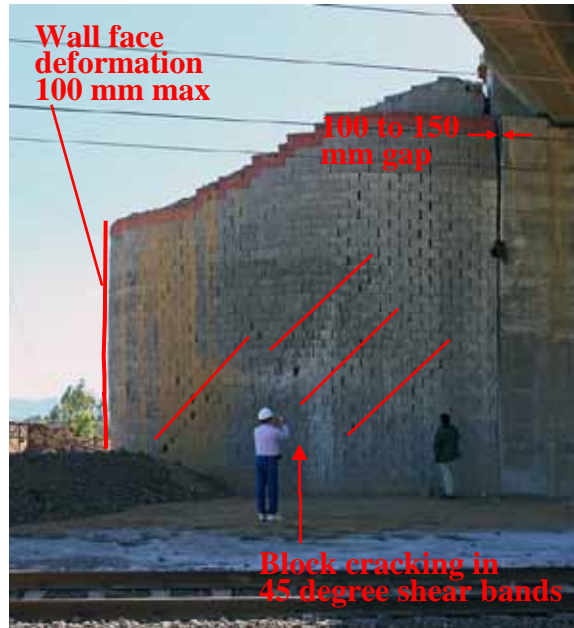


Figure 276. Photo. Wall with cracked block pattern at Muros Talca.

Finally, it should be noted that the wall at Estribo Francisco Mostazal (site 11) is a geogrid reinforced modular block wall directly supporting the abutment and bridge foundation loads (see table 6). This type of abutment wall is what is referred to as a “true” MSE bridge abutment. The MSE abutment walls at site 11 performed very well, exhibiting no signs of lateral or vertical movement due to the earthquake. While the bridge suffered some relatively minor damage (see figure 277), the damage was not caused by the walls but was probably due to the severe bridge skew angle (similar to other bridges observed by TIRT and described in chapter 4) combined with the bridge tending to slide down hill, as it was located on a downhill roadway grade.



Figure 277. Photo. Bridge supported on footing on top of block-faced geogrid wall at Estribo Francisco Mostazal.

In summary, the walls observed at the 32 sites visited by TIRT performed well, although a few walls did suffer some damage. In most cases, damage was minor and repairable. Of the walls that deformed laterally, movement tended to be greatest near the wall top with little, if any, lateral movement at the wall base, indicating that resistance to sliding is likely much greater than assumed in design. The most significant wall performance problems were primarily the result of inadequate details at the corners and full-height joints and at the wall top due to inadequate coping details. These performance problems point to the importance of using details that ensure good connectivity between adjacent panels across a joint, which, for even current design codes such as the AASHTO LRFD bridge design specifications, should be better described. However, in spite of these performance problems, all of the walls met the no-collapse criterion typically applied for seismic design, including those walls that were subjected to the effects of liquefaction.

CHAPTER 6. LESSONS LEARNED FROM THE EARTHQUAKE

6.1 GENERAL

This chapter summarizes the overall performance of various bridge components, retaining walls, and bridge sites based on the observations detailed in chapter 4 and chapter 5. The observed performance leads to various lessons learned from the 2010 offshore Maule earthquake. It forms the basis for several conclusions drawn from the postearthquake reconnaissance regarding recommended seismic design and retrofit improvements and future research needs.

6.2 SUPERSTRUCTURE ROTATION

6.2.1 Skewed Bridges

The direction of bridge skew is illustrated in figure 278 for clarity in the following discussions. Skew is defined as the direction of rotation from the transverse line (perpendicular to the bridge centerline) to the skew side or abutment back wall of the bridge. For example, figure 278 indicates a clockwise skew and a counterclockwise skew.

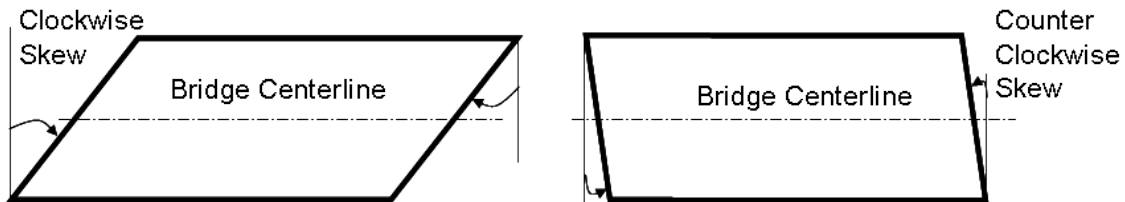


Figure 278. Illustration. Notations on skew direction.

Table 7 summarizes the characteristics and earthquake-induced damage patterns of bridges with a skew angle of 20 degrees or more. It lists the bridge name, bridge orientation, skew angle, skew direction, material used in girder, presence of diaphragms, transverse displacement at intermediate bents, and direction of deck rotation. The combination of these parameters helps determine the mechanism of bridge deck rotations.

Table 7. Summary of bridges and bridge damage.

Bridge Characteristics					Damage Pattern	
Site	Name	Orientation	Skew and Direction	Girder/End Diaphragm	Transverse Movement at Intermediate Bents	Rotation
1a 1b	Miraflores	NE-SW	20 degrees counterclockwise	Concrete/No	Negligible	Clockwise
2a	Lo Echevers	NE-SW	33 degrees counterclockwise	Concrete/No	Negligible	Clockwise
5	Quilicura	E-W	45 degrees counterclockwise	Steel/Yes	Negligible	Clockwise
7	Romero	E-W	31 degrees clockwise	Concrete/No	Negligible	Counterclockwise
10b	Hospital	NW-SE	40 degrees counterclockwise	Concrete/No	Significant	Clockwise

All of the bridges in table 7 consistently rotated about the centroid of the bridge superstructure in the opposite direction of their skew, regardless of the bridge orientation, magnitude of the skew angle, or presence of diaphragms. The fact that most of the bridges experienced negligible transverse displacements also indicates that the rotation effect was dominant in these bridge superstructures, with the acute corners of each bridge moving away from their abutments at both ends.

Based on the observations, the movement of a bridge superstructure can be illustrated in four steps, as shown in figure 279. Under the earthquake excitations (steps 1a, 1b, and possibly 3), the bridge superstructures first moved toward one abutment (left in figure 279) and impacted against the abutment back wall (step 2). The reaction from the back wall then turned the superstructure in a direction opposite to the skew direction (counterclockwise in figure 279). The rotational motion (step 3) was amplified due to the fact that the rotational vibration mode of the bridge superstructure is more sensitive to the ground motions, as illustrated with the acceleration response spectra recorded at Hospital Station in Curicó, since all the concrete girder bridges listed in table 7 have superstructures supported on neoprene pads and restrained with vertical seismic bars (see figure 280).⁽⁶⁾ The superstructures are weakly restrained in plan with the fundamental vibration mode in translation. With continuing deck rotations, the acute corners at two ends of the bridge finally moved away from the abutments, knocking off the curtain walls and becoming unseated (steps 4a and 4b). Note that the possibility of having significant rotational ground motions at the bridge site can further amplify the rotational motion (step 3).

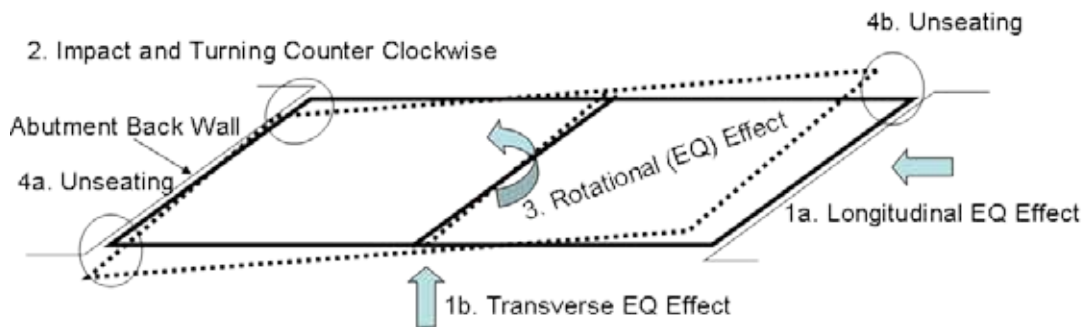


Figure 279. Illustration. Deck rotation of a representative bridge (two spans shown).

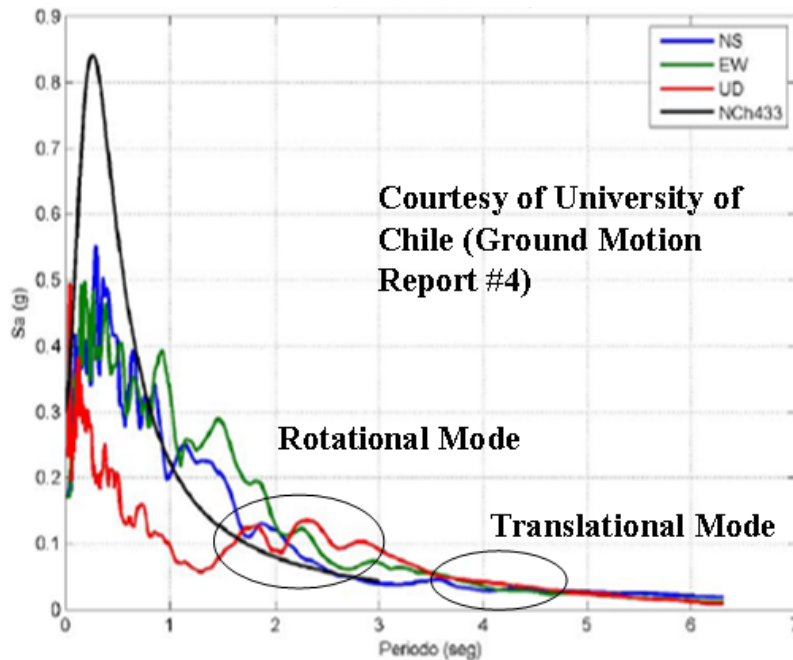


Figure 280. Illustration. Rotational and translational mode responses to ground motions.

6.2.2 Straight Bridges

The bridges with little or no skew (Chada and Las Mercedes bridges) rotated counterclockwise, as discussed in chapter 4. Unlike the skewed bridges, the deck rotation of the straight bridges cannot be explained by the skew effect. The possible factors contributing to significant rotations in these bridges are as follows:

- The rotational mode of vibration of those bridges was very sensitive to ground motions. Any accidental eccentricity between the center of mass and the center of rigidity of the superstructure of a bridge could lead to substantial rotations.
- The rotational component of ground motions could be significant.
- The fault directivity effect could be significant because both bridges are approximately oriented along the east-west direction.

Considering both the skewed and straight bridges, observations can be made on the overall reasons for bridge deck rotation. Skew of bridges is a significant but not necessarily decisive factor contributing to the bridge rotation. The high sensitivity of the rotational vibration mode of the bridge to ground motion, particularly rotational excitations, could have been dominant. The fact that all bridges experiencing significant rotations were not far from Santiago, where soil conditions are relatively stiff, supports the possibility of rotational ground motions at the bridge sites. Further analysis is required to understand the significance of this phenomenon.

6.3 GIRDER DAMAGE

6.3.1 Fracture of Steel Girders

The superstructure of the Cardenal Raúl Silva Henríquez bridge is divided into two parts by the center expansion joints at bent 11. The northeast portion of the bridge is supported by a concrete substructure, and the southwest portion is mainly supported on a steel substructure. Most of the bridge bents are supported on drilled shafts. During the earthquake, the two parts most likely vibrated separately.

The most plausible reason for the girder damage at each abutment, as discussed in chapter 4, is excessive longitudinal force applied on the end support. During the earthquake, the majority of the inertia force on half of the bridge superstructure was resisted by the end support at each abutment. The excessive force resulted in either fillet weld fractures at the southwest abutment or steel girder fractures in web and bottom flange at the northeast abutment.

6.3.2 Failure of Concrete Girders

The exterior prestressed concrete girders of the Chada and Romero bridges, which were constructed without diaphragms, experienced out-of-plane block shear failures due to transverse impact loads from shear keys, as shown in figure 281. When partial diaphragms were used between the girders, such as in the San Nicolás bridge, the bottom portion of the exterior girder still experienced significant shear cracking, as shown in figure 282. However, with the use of even partial concrete teeth between girders, as shown in the Llacolen bridge in figure 283, both exterior and interior prestressed concrete girders suffered no visible damage. One interior girder in the west portion of Llacolen bridge experienced a horizontal crack, as shown in figure 57. This was because the concrete teeth provided sufficient lateral restraints on most of the girders, making them work together and share the transverse seismic force.



Figure 281. Photo. Exterior girder damage at Chada bridge, no diaphragms.



Figure 282. Photo. Exterior girder damage at San Nicolás bridge, partial diaphragms.



Figure 283. Photo. Exterior girder damage at west abutment of Llacolen bridge, concrete teeth.

6.4 CONNECTION BETWEEN SUPERSTRUCTURE AND SUBSTRUCTURE

6.4.1 Shear Key and Steel Stopper Failures

Concrete shear keys or shear keys in integral construction with curtain walls fulfilled the function of sacrificial devices to protect the substructure of bridges. Their failures were observed regardless of the presence of bridge deck rotations during the earthquake (e.g., Independencia, Chada, Romero, and Hospital bridges).

Steel stoppers used in several bridges (e.g., Independencia, Miraflores, and Lo Echevers bridges) failed prematurely. The Independencia bridge with steel stoppers was taken out of service following the earthquake, but the parallel bridge with concrete shear keys and diaphragms survived the earthquake with repairable damage. It was concluded that the two-bolt connections from each steel stopper to the cap beam was too weak to resist any significant bending moment. However, once welded to steel girders, the steel stoppers prevented lateral movement of girders, as observed in the Quilicura railway bridge shown in figure 112.

6.4.2 Vertical Seismic Bars

Vertical seismic bars were used in a number of bridges (e.g., Chada, Las Mercedes, Llacolen, Romero, Hospital, and Pichibudis bridges). In general, they were flexible and underwent significant deformations during the earthquake. All were well anchored into the cap beams and decks. Field evidence only indicated bar pullout in bridges with fallen spans. It is uncertain

whether the seismic bars provided vertical restraints to the bridge girders because there was no evidence of vertical up-and-down movements of the girders. This observation may be clarified after analyses using recorded ground motions.

6.4.3 Bridge Bearings

In general, bridge bearings functioned well during the earthquake. Several of them were displaced significantly, such as in the Lo Echevers bridge shown in figure 95 and in the Cardenal Raúl Silva Henríquez bridge shown in figure 125.

6.5 GIRDER SEAT LENGTH

The superstructure of a number of concrete and steel girder bridges (e.g., Llacolen, Miraflores, Lo Echevers, Romero, Hospital, Tubul, Biobío, and pedestrian bridges) dropped off their supports during the earthquake. In general, the support seat length is insufficient.

6.6 COLUMN SHEAR FAILURE

The pier caps and piers in all but the Llacolen and Juan Pablo II bridges received virtually no damage during the earthquake. This represented successful design of these bridge components. Several columns in the Llacolen and Juan Pablo II bridges failed in shear due mainly to the ground settlement and lateral spreading.

6.7 FOUNDATION MOVEMENT AND DAMAGE

6.7.1 Overview

In general, bridge foundations performed relatively well in the earthquake. With the exception of cases where liquefaction-induced vertical or lateral soil movement was severe, foundations did not appear to suffer significant permanent deformations or significant damage, based on surficial observations. Most of the newer bridges visited were supported by shaft foundations (typically 4.9 ft (1.5 m) in diameter and less than 98 ft (30 m) deep). These foundations appeared to be relatively light compared to bridge foundations currently used in areas of high seismic hazard in the United States. However, the foundations performed well in most cases.

To identify lessons learned regarding bridge foundations, two broad categories of geotechnical performance issues must be considered: foundation performance when liquefiable soils were probably not present and foundation performance when liquefiable soils were present. For those sites where liquefaction probably occurred, geotechnical performance issues are further divided between the effects of liquefaction-induced settlement and liquefaction-induced ground failure and the effects of lateral movement. The observations of geotechnical performance of foundations in the sections that follow are made within this context.

6.7.2 Sites Not Affected by Liquefaction

Seventeen of the 32 sites visited did not appear to have significant liquefaction. However, poorer soil conditions (e.g., soft to still clays or loose sands) appeared to contribute to the amplification of ground motions (see chapter 2) and increased foundation deformation (see chapter 5), possibly

increasing stress or deformation in the superstructure. In general, sites where better soil conditions were present performed better and showed minimal damage. Near-surface soft to stiff clays appeared to be especially troublesome, especially in terms of their effect on approach fill stability (e.g., sites 7, 8, and 10), but did not cause movement of or damage to the bridge abutments.

6.7.3 Sites Affected by Liquefaction

None of the sites where liquefaction likely occurred (15 of the 32 sites visited) were specifically designed to mitigate the effects of liquefaction through use of ground improvement or foundation strengthening (see chapter 5 for additional background on this issue). This affords the opportunity to observe the effect liquefaction can have on foundation and abutment performance for structures that are otherwise designed using the AASHTO or similar specifications, depending on the age of the structure.

6.7.3.1 Effects of Liquefaction-Induced Ground Failure

What was most surprising was the good performance of bridge abutments retaining 13- to 26-ft (4- to 8-m)-high approach fills over gently sloping ground, even when severe vertical and horizontal approach fill deformation (1.6 to 3 ft (0.5 to 1 m) or more) occurred due to liquefaction of soil below the approach fill (see table 6, specifically sites 15, 20, 21, 22, and 27). Although there were a few cases where 1.9 to 5.8 inches (50 to 150 mm) of lateral movement of the abutment appeared to have occurred, in most cases, no discernable movement occurred. This may be the result of three-dimensional effects reducing the lateral forces acting on the abutment foundations relative to what would be predicted assuming two-dimensional (i.e., plane strain) conditions. Furthermore, the liquefaction-induced slope failure tended to follow the path of least resistance (i.e., in the direction perpendicular to the roadway and bridge centerline). For those cases where either the abutment or an interior pier was located on a general slope, such as at a riverbank, the beneficial three-dimensional slope geometry was not present and foundation and substructure movement and damage due to liquefaction-induced ground failure was more likely (e.g., sites 17, 18, 19, and 25; see chapter 5 for details). These observations may have important implications for the strategy used for liquefaction design of bridges both in Chile and the United States.

6.7.3.2 Effects of Liquefaction-Induced Settlement and Downdrag

Liquefaction-induced ground settlement was observed at many of the bridge sites where liquefaction occurred. However, settlement of the bridge foundations only occurred for a few of those sites (sites 25, 27, and 31). In general, regardless of the amount of liquefaction-induced ground settlement that occurred, the foundations did not settle significantly if tipped in a reasonably good bearing layer. However, if the foundation was relatively shallow and not tipped in a relatively dense bearing layer, significant settlement of the foundation did occur.

6.8 RETAINING WALLS AND ROADWAY FILL

Three types of walls were inspected by TIRT: panel-faced MSE walls using bar mat or steel strip soil reinforcement, modular block high-density polyethylene geogrid reinforced walls, and concrete gravity walls. Overall, retaining walls performed well during the earthquake. Tieback and soil nail walls appeared to suffer little or no damage based on observations made by others. True MSE abutments, where the bridge footing foundation was directly supported on top of the MSE wall

(e.g., site 11, see chapter 5), also performed well with no apparent deformation or damage to the walls. Note that most of these walls were designed using the AASHTO Standard Specifications (see chapter 3). The observed wall performance appears to indicate that the AASHTO specifications as applied in Chile provide a safe design for seismic loading conditions.

There was no evidence of lateral sliding of the walls, the limit state that often controls wall design for seismic conditions in North American design practice (see chapter 5). Where wall face lateral movement was observed, the movement was primarily rotational, with the maximum movement near the wall top. It appears that the passive resistance at the wall toe in combination with friction along the wall base prevented significant translational movement.

Minor damage observed in several walls was due mainly to poor detailing. Inadequate coping details allowed a few of the top blocks to topple off the wall (modular block walls). Poor wall corner details or vertical full-height joint details (such as between the curtain wall and MSE wall retaining the approach fill sides) allowed panels to separate and wall backfill to spill out through the gaps in the facing. Stresses during seismic loading, especially for relatively tall walls (30 ft (9 m) or more) appeared to be more pronounced at abrupt changes in wall geometry (e.g., corners and small radius changes in alignment), indicating the need for more robust wall facing designs in that type of situation. Soil reinforcement that is too short, especially near the wall top or where uniform low shear strength medium sand is used as backfill, can contribute to excessive wall or panel movement.

CHAPTER 7. CONCLUSIONS AND RECOMMENDATIONS

7.1 GENERAL

Based on the overall performance of various bridge components, retaining walls, and other structures summarized in chapter 6, conclusions can be drawn about the seismic performance of the transportation infrastructure in Chile during the offshore Maule earthquake. Considering the geologic conditions, earthquake settings, ground motions, and geotechnical and structural performance of the infrastructure, recommendations are made in this chapter for both immediate implementation and future investigation. In addition, research needs are identified for the improvement of seismic design of bridges, walls, and other structures used in transportation facilities. These recommendations may also be applicable for seismic retrofit purposes.

Some of the lessons learned require additional study to specifically assess how such lessons should be implemented. Toward that end, immediate needs are identified to gather more information and confirm assumptions and interpretations made in this report.

7.2 CONCLUSIONS ON TRANSPORTATION INFRASTRUCTURE PERFORMANCE

Less than 0.15 percent of the bridges in the MOP inventory collapsed or suffered damage that rendered them unusable. Considering the magnitude of the earthquake, the transportation infrastructure in Chile performed relatively well and was able to support postearthquake emergency response and recovery. Even so, improvements can be made to further enhance the seismic performance of the infrastructure both in structural and geotechnical terms.

Many spans of precast prestressed discontinuous girder bridges with continuous decks fell from their supports, probably due to the significant in-plane rotation of their superstructures due to severe shaking. Lateral steel stoppers used to provide both vertical and lateral restraint to the girders were largely unsuccessful due to their inadequate connection detail to cap beams or abutments. Conversely, reinforced concrete shear keys served their design purpose, transferring lateral loads to the substructures. Vertical seismic bars were widely used to restrain the vertical motion of the spans, and they also performed well. Bridge substructures (foundation, column, and cap beam) generally behaved satisfactorily (undamaged cover concrete and no evidence of yielded reinforcing steel) except that several columns suffered shear failure due to ground settlement and lateral spreading. However, the satisfactory performance of the columns generally occurred in bridges with failed superstructure-to-substructure connections, and it is not clear whether this superior performance was due to overdesign of the columns or to the failure of the connections, which limited the forces in the columns to less than yield. All retaining walls exceeded performance expectations.

7.3 RECOMMENDATIONS FOR IMMEDIATE IMPLEMENTATION

7.3.1 Diaphragms in Concrete Girder Superstructures

In past earthquakes, full-depth diaphragms between girders have been very effective in distributing earthquake loads among the girders and to the bearings and substructure below. Bridges with full-depth diaphragms again performed well in Chile, whereas those without diaphragms

performed poorly. To minimize the possibility of lateral shear failure and transverse unseating of girders, it is recommended that full-depth diaphragms be installed in all bridges and implemented in all future designs

7.3.2 Support Length

Adequate support length is a proven countermeasure to the unseating of bridge spans. It is recommended that generous seat lengths be provided in all new designs based on seismic hazard, soil type, column height, distance between movement joints, and angle of skew. Both the AASHTO specifications and Caltrans' seismic design criteria have examples of such requirements. Existing bridges with inadequate support lengths should be retrofitted with seat extenders or longitudinal restrainers as a matter of priority

7.3.3 Lateral Seismic Restraints

Lateral steel stoppers of girders were typically anchored to their supports with two anchor bolts aligned in the direction of the span. In this case, only one bolt was available to transfer the overturning moment when the seismic load from the girder was applied to the stopper some distance above the cap beam or abutment seat. This situation is quite ineffective. It is recommended that at least four anchor bolts be used to anchor each stopper to the cap beam in a configuration that provides both transverse and span-wise resistance to shear and overturning moments.

Unless specifically designed to fail at lateral load that is less than the capacity of the column below (thus protecting the column), all shear keys (both steel and concrete) should be designed against failure. This can be done in one of two ways: either the key or stopper is designed to resist the unreduced load from an elastic analysis (strength reduction factor = 1.0 or 0.8), or it is designed to resist the maximum shear the column can generate in its fully yielded state (i.e., with fully developed plastic hinges and including overstrength effects). Regardless of the method, the strength of any shear key should not be less than a specified minimum, usually expressed as a percentage of the tributary weight at the key.

Shear keys are not necessary if the bearings are engineered to take the lateral loads and uplift forces. In such cases, the bearings need to have sufficient internal strength to transfer the forces without rupture and remain functional. They also need to be anchored accordingly. If it is uneconomical to provide bearings of this type, shear keys are required. However the bearings should be anchored to the cap beams or abutments to prevent being dislodged during shaking.

7.3.4 Substructure Design

Confinement has been demonstrated to be an effective means for preventing shear failure in reinforced concrete columns. It is recommended that columns with inadequate transverse reinforcing steel be retrofitted with external concrete, steel, or polymer jackets to prevent brittle shear failures and to help ensure flexural ductile yielding.

7.3.5 Retaining Wall Design

Since retaining walls performed very well in general, new design specifications could be developed to provide a no-analysis seismic design option for internal and external wall stability (i.e., for

sliding, eccentricity, and bearing). Such an option might only be applicable within certain limits of ground acceleration, wall height, and surcharge conditions and would require minimum wall details (e.g., engineered connectivity of vertical joints in the face of the wall, especially at the corners; use of well-graded granular backfill; and good coping details on top of the wall).

The minimum wall details developed for the no-analysis option should also be required for walls that do not qualify for this option such as those in high seismic zones and should be considered for inclusion in the AASHTO specifications.

Bridges supported on MSE walls also appeared to have performed well in this earthquake. It is recommended that this cost-effective technology be investigated as an alternative to conventional, CIP, reinforced concrete abutment walls.

7.4 RECOMMENDATIONS FOR FUTURE WORK AND RESEARCH NEEDS

7.4.1 Structural Engineering Recommendations

Conduct a rigorous study of earthquake ground motion records to look for evidence of a rotational component in ground motion that could explain the in-plane rotation of non-skewed symmetric bridges.

The ground motions recorded during the offshore Maule earthquake can be characterized by long duration and multiple pulses, particularly at those stations near Santiago where soils are relatively stiff compared to other regions such as Constitución and Concepción. Although farther from the epicenter of the earthquake, the bridges near Santiago exclusively experienced significant in-plane rotations in their superstructures during ground shaking. The reason for this rotation is unclear, but one possibility is that the stiffer soils near Santiago favored the propagation and amplification of rotational ground motions.

To the authors' knowledge, the occurrence of rotational components in earthquake ground motions and their effect on bridge response and safety has not been previously studied. It is recommended that the ground motions recorded during this earthquake be rigorously analyzed and that case studies be undertaken for the non-skewed bridges that exhibited strong rotational response.

Study the relationship between the strength reduction factor, ductility, and period of vibration during long-duration ground motions with multiple pulses. Also study the influence of these characteristics in the ground motion on the in-plane rotation of non-skewed symmetric bridges. Prepare recommendations for AASHTO consideration regarding long-duration effects and potential changes to response modification factors.

It is known that long duration and multiple pulses can have a significant effect on the inelastic response of a bridge and can directly impact the integrity of the load path, especially if the bridge behaves as a pure elastoplastic system. In these circumstances, the relationship between the strength reduction factor, ductility, and period of vibration may differ from that obtained under more conventional ground motions and may warrant the use of a different set of response modification factors. The unique long-duration and multipulse feature of the ground motion may also affect the rotational response of bridge superstructures. These unique features in the ground motion and the

corresponding inelastic response in the structure and approach fills may also explain the in-plane rotation of the superstructures in non-skewed bridges.

Considering the similarities in geologic and tectonic conditions, design specifications, and construction practices between the Chile and the United States, indepth studies on the effect of long-duration ground motions (with and without multiple pulses) on bridge behavior during this earthquake would be of immediate relevance to U.S. practice, particularly in Oregon and Washington. Research outcomes are likely to affect ground motion provisions as well as design requirements for bridges in these states.

Validate the support length requirements in the AASHTO specifications for skewed bridges.

Many spans of skewed bridges were unseated, confirming the sensitivity of this kind of bridge to collapse. The minimum requirements in the AASHTO specifications are based on engineering judgment rather than rigorous analysis, and this earthquake provides the opportunity to check the validity of these requirements, particularly for skew. Research outcomes would likely affect the support length requirements for bridges throughout the United States.

Study the implications of combining the scour and earthquake load cases for coastal bridges located in tsunami inundation zones

The earthquake-induced tsunami generated significant waves and currents that added both horizontal and vertical loads on some coastal bridges and caused the erosion of soils around bridge foundations. These additional loads may further damage a bridge that has already been damaged by earthquake shaking. Structures may collapse and low-lying bridges may be lifted off their substructures and swept upstream. Although designing for scour is required in U.S. specifications, the combination of the effect of scour and earthquake effects is not required, as in the Chilean code (see appendix B). These combined effects warrant further investigation

Conduct feasibility studies of bridges without diaphragms for potential application in accelerated bridge construction.

Concrete blocks (or shear keys) on each side of cap beam girders are an alternative to diaphragms for the distribution of transverse loads between girders and from the deck slab to the cap beam. They can effectively prevent the girders from shear failure by reducing the maximum load on each individual girder. If the joint between the top flange of the girder and deck slab can be economically designed to transfer significant moments without distress, this alternative may be an attractive strategy in accelerated bridge construction

Conduct case studies on the AASHTO global design strategy that permits fusing of the super-to-substructure connection and protection of the substructures and foundations from seismic damage.

Adjusting the strength of the shear keys in a bridge superstructure is an alternative strategy for managing the load path and energy dissipation, thus enabling cost-effective designs that ensure bridge substructures suffer little or no damage. This strategy is permitted in the new AASHTO specifications for seismic design, but no comprehensive study has been done to date to prove its viability. This earthquake provides the opportunity to fill this gap.

Study the trade-off between lower maintenance costs with fewer joints and reduced redundancy for longitudinal seismic loads in continuous bridges.

Jointless bridges are widely favored for their lower corrosion-related maintenance costs and the increase in redundancy for gravity loads. However, the longitudinal distribution of load in these continuous bridges can be a challenge, especially in those cases where the superstructures are not monolithic with their piers (i.e., supported on bearings that allow thermal expansion). In long, multispan bridges, very large loads can be attracted into a few structural elements, and, unless designed for this heavy demand, failure can occur in the super-to-substructure connections at these elements. Studies are required to understand the trade-off between lower maintenance costs (with fewer joints) and the increased demand on a few substructures (i.e., the reduced redundancy for lateral loads),

7.4.2 Geotechnical Engineering Recommendations

As previously noted, geotechnical conclusions in this report are based on surficial observations and approximate geometry. Subsurface data and foundation and geometric details are required for most of the sites visited to confirm these preliminary interpretations. These data are a necessary first step towards deriving the most benefit from the investigation of this earthquake. Digitized ground motion records are also required if the more detailed modeling necessary to confirm the preliminary conclusions is to be achieved. Once site-specific data are obtained, future efforts in the geotechnical area should focus on the following:

Develop the ground motion records from this earthquake for use in seismic design when long-duration subduction zone records are needed and add them to databases used by designers for conducting site-specific seismic analyses.

Achieving this goal will involve obtaining subsurface information and other site information where the ground motions were recorded so that they can be deconvolved to base rock motions, cleaned up, baselined, etc. in order to make them most useable. Such digital records would also be extremely useful for design where subduction zone earthquakes must be considered (e.g., the west coast of North America).

Conduct research to better quantify the beneficial effect of three-dimensional geometry issues on abutment performance when liquefaction occurs.

For example, how wide does the fill need to be to eliminate the three-dimensional benefit identified in chapter 5 and chapter 6 such that the use of a two-dimensional slope stability or lateral spreading analysis in the direction toward the bridge is not too conservative? The case histories summarized in this report should be used to calibrate three-dimensional numerical models to investigate this issue more fully.

Conduct research to improve the quantification of lateral and vertical (downdrag) forces on foundations and abutments induced by liquefaction.

Based on the foundation performance observed in this earthquake, liquefaction lateral spreading and downdrag design with regard to their effect on foundations may be too conservative.

Conduct research to improve the estimation of lateral and vertical ground deformation caused by liquefaction using measured deformation data from the 15 bridge sites where liquefaction occurred as a result of this earthquake.

Methods currently available for estimating these deformations are relatively crude. In addition, a reasonable estimate of both vertical and horizontal ground movements due to ground liquefaction and lateral spreading should be made available to practitioners who will implement the displacement-based design methodology to ensure that undesirable structural failure and damage modes of bridges are removed. The fact that most liquefied sites during the Chile earthquake were not treated for improved performance offers a good opportunity to improve the engineering estimate of liquefaction-induced vertical and horizontal ground movements.

Use the liquefaction performance research identified above to develop a strategy from a no-collapse design objective perspective to focus liquefaction mitigation efforts on only the more severe cases.

Judging what should be considered severe may be a challenge and may be very site-specific. Even if such a strategy could be formulated and implemented, thorough site- and project-specific geotechnical analyses would still be needed to assess the severity of the likely effects of liquefaction at a given site.

Conduct research to develop more accurate lateral deformation models for walls under seismic loading considering the likelihood of rotational rather than translational movement.

Since very little evidence of the translational movement of a wall as a rigid body was found, the theoretical approach typically used to perform seismic deformational analysis of walls (Newmark analysis) may not match reality.^(14,20) However, the good seismic wall performance observed still provides justification for using a reduced horizontal acceleration coefficient for design, even considering the lack of translational movement.

Conduct research to investigate the effect of high vertical acceleration on the performance of selected bridges and walls.

Vertical accelerations are often ignored in current seismic design practice. The effects of these relatively high vertical accelerations on bridge and wall performance should be further investigated and their implications to design practice determined.

APPENDIX A. SUBSURFACE DATA

A.1 SUBSURFACE DATA

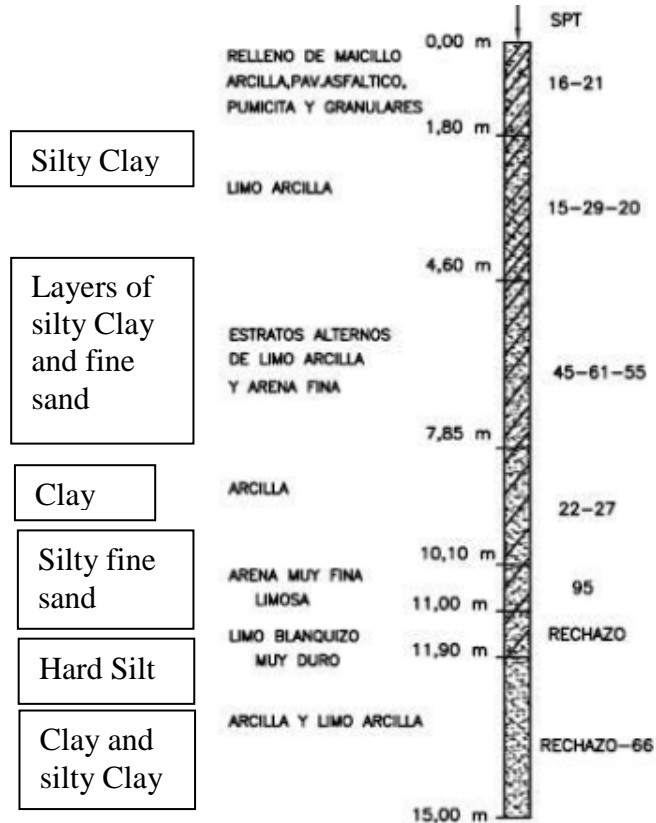
A.1.1 Subsurface Data for Américo Vespucio/Miraflores (Site 1)

One boring log was available at site 1. The specific location is not known, but its general location is within the circle in figure 284. A copy of the boring log is provided in figure 285.



© Google, Europa Technologies, Inav/Geosistemas SRL, and GeoEye

Figure 284. Map. Image of site 1 taken prior to earthquake.



Source: MOP

Figure 285. Illustration. Boring log at site 1.

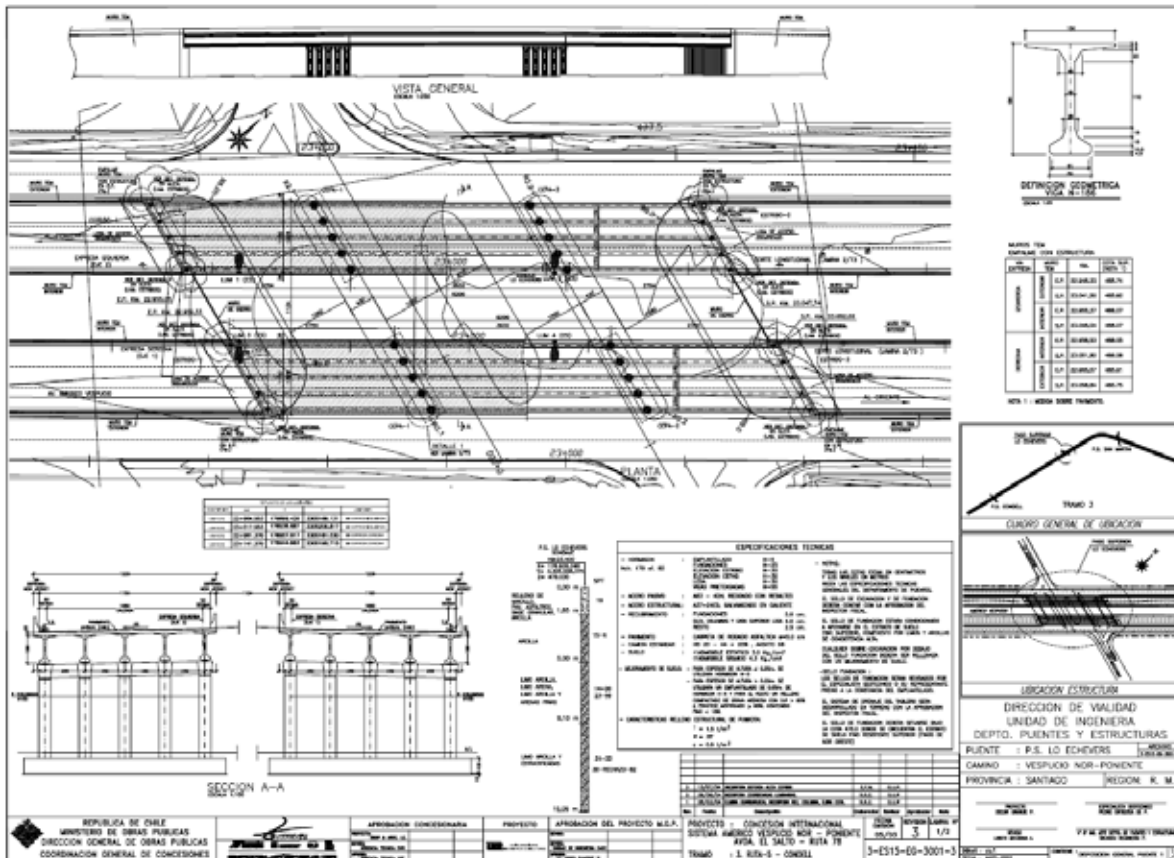
A.1.2 Subsurface data for Américo Vespuccio/Lo Echevers (Site 2)

The location of the site 2 bridge is shown in figure 286. A copy of as-built bridge plans and one boring log at site 2 are provided in figure 287 through figure 289.



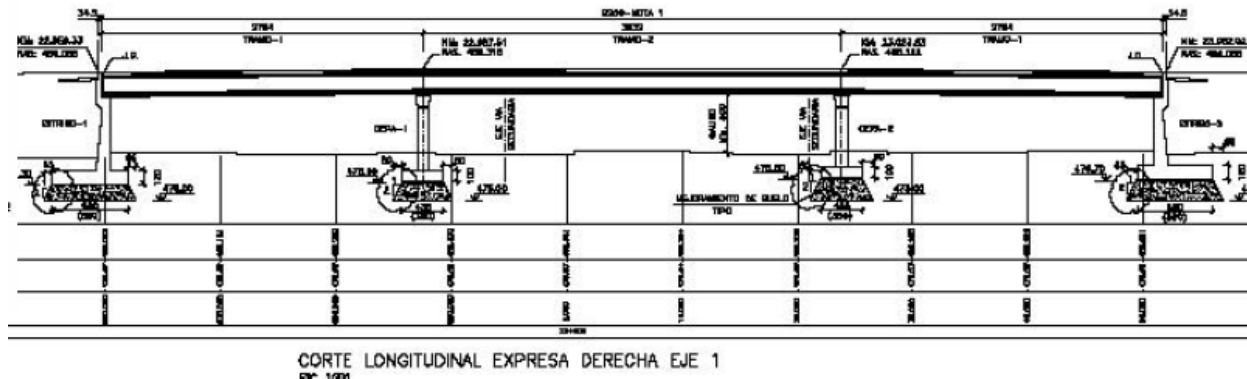
© Google, Europa Technologies, Inav/Geosistemas SRL, and GeoEye

Figure 286. Map. Image of site 2 taken prior to earthquake and showing approximate location of test hole.



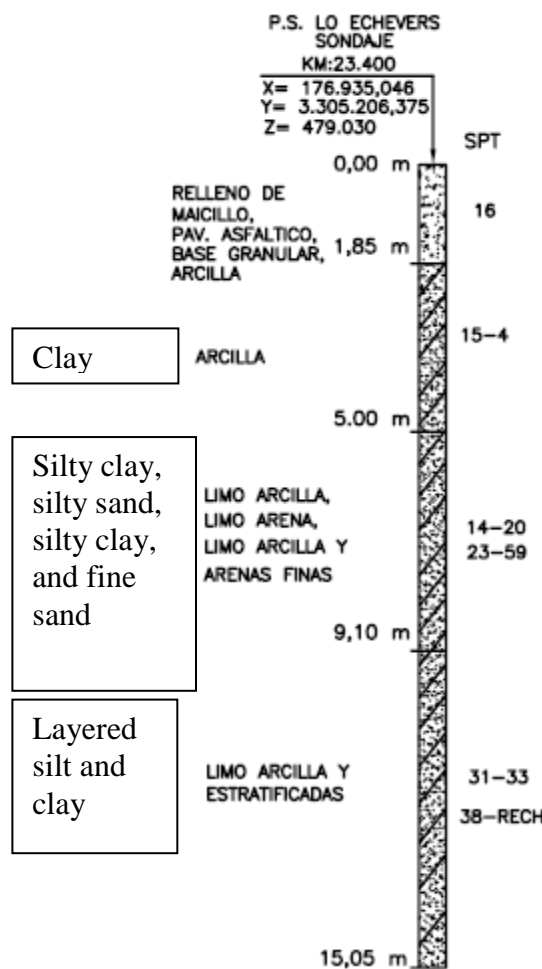
Source: MOP

Figure 287. Illustration. As-built bridge plan for site 2.



Source: MOP

Figure 288. Illustration. As-built bridge profile for site 2 showing footing foundations.



Source: MOP

Figure 289. Illustration. Boring log at site 2.

A.1.3 Subsurface Data for Avenida Romero Acceso Sur (Site 7)

The location of bridge site 7 is shown in figure 290. A copy of as-built drawings and one boring log at site 7 are included in figure 291 and figure 292.

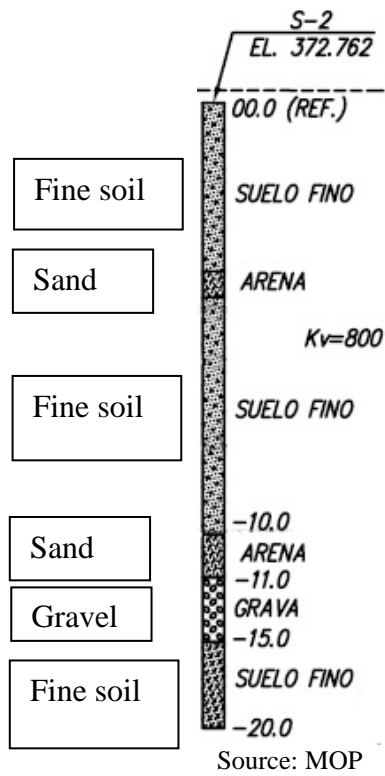


Figure 292. Illustration. Boring log for site 7.

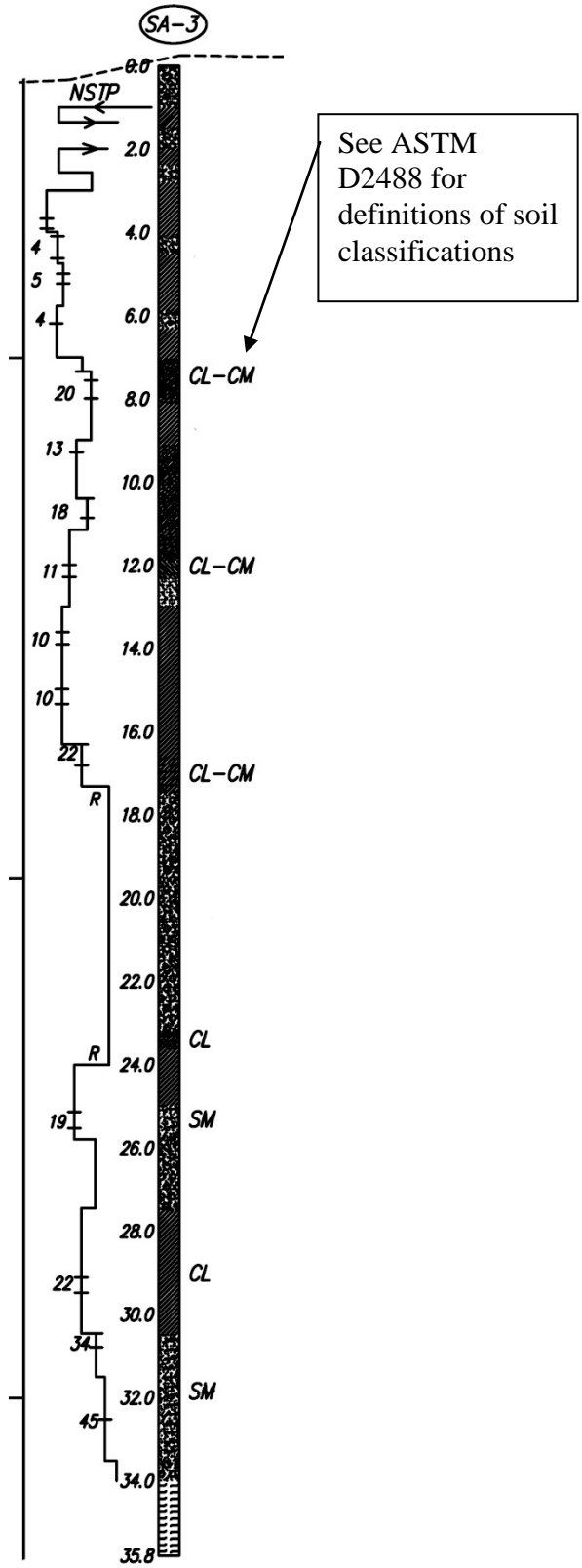
A.1.4 Subsurface Data for Avenida Chada Acceso Sur (Site 8)

The location of bridge site 8 is figure 293. A copy of as-built drawings and one boring log at site 8 are included in figure 294 and figure 295.



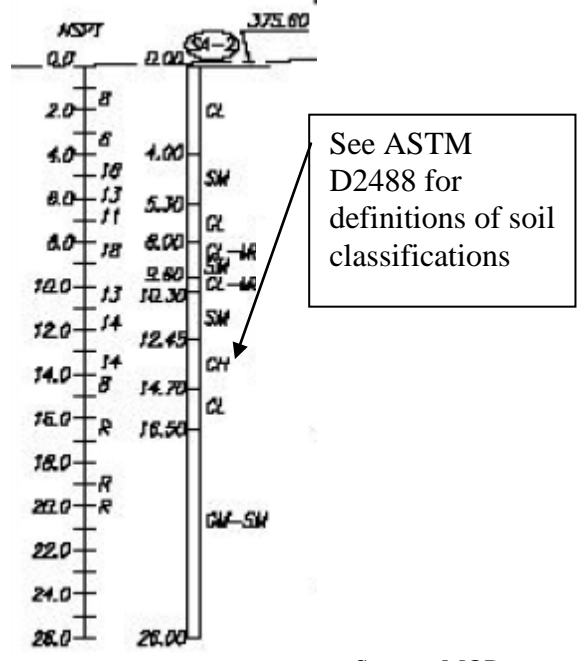
© Google, DigitalGlobe, and Inav/Geosistemas SRL

Figure 293 Map. Image of site 8 taken prior to earthquake and showing approximate location of test hole.



Source: MOP

Figure 295. Illustration. Boring log for site 8.



Source: MOP

Figure 298. Illustration. Boring log SA-2 for site 10.

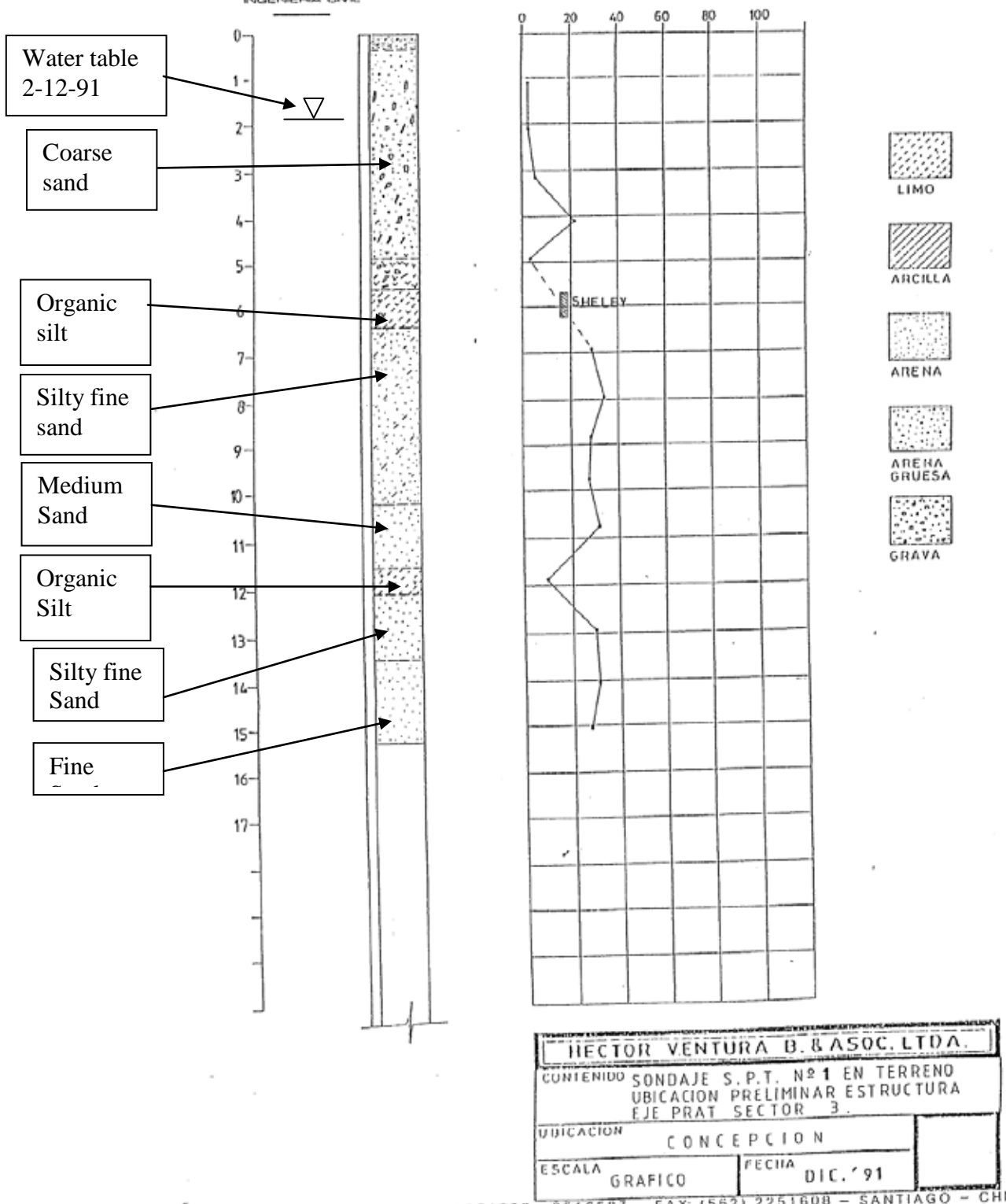
A.1.6 Subsurface Data for Via Elevada 21 de Mayo/Cruce Ferroviario (Site 28)

The location of bridge site 28 is shown in figure 299. Red dots indicate the location of the test holes with the corresponding numbers labeled. Copies of three boring logs at site 28 are given in figure 300 through figure 305.



© Google, DigitalGlobe, Inav/Geosistemas SRL, and Europa Technologies

Figure 299. Map. Image of site 28 taken prior to earthquake and showing approximate locations of test holes.



Source: W. Neely

Figure 300. Illustration. Boring log S-1 for site 28.

Ubicación : Boring No. 1

Fecha : 2/12/91

Entre colas: (m)		N ₁ *	N ₂ **	Entre colas: (m)		N ₁ *	N ₂ **
0.79	1.24	1	3				
1.84	2.29	2	3				
2.91	3.36	1	6				
3.84	4.29	5	12				
4.71	5.16	2	3				
5.62	6.12	SHELBY					
6.68	7.13	17	29				
7.70	8.15	15	34				
8.61	9.06	13	29				
9.56	10.01	11	28				
10.54	10.99	10	32				
11.63	12.08	4	10				
12.75	13.20	14	30				
13.84	14.29	15	31				
14.82	15.27	10	27				

N₁ = number of blows per 15 cm.

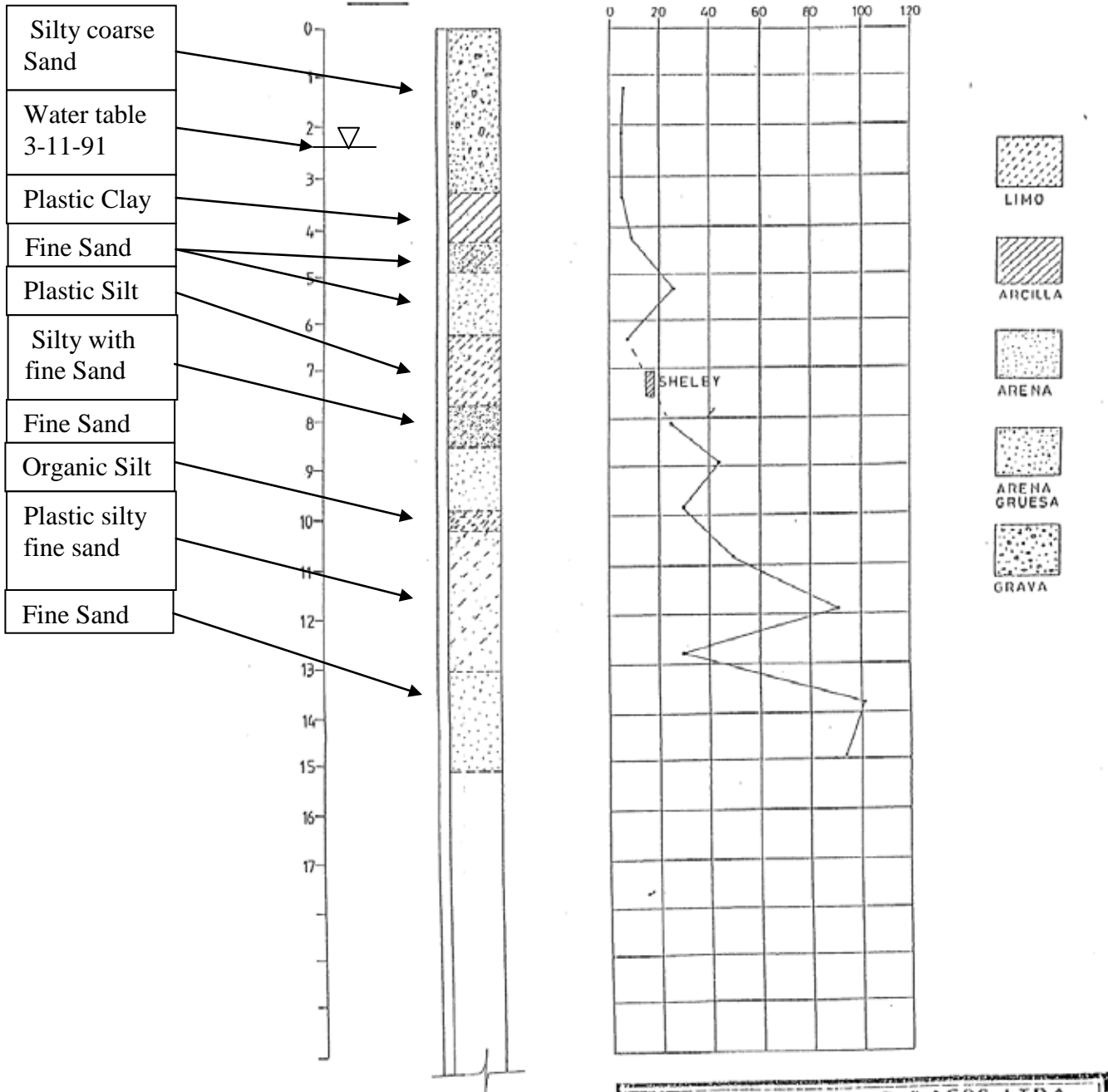
N₂ = number of blows per 30 cm.

Entre colas = depth range.

1 cm = 0.39 inches.

Source: W. Neely

Figure 301. Illustration. Detailed standard penetration test blow counts for boring log S-1 for site 28.



HECTOR VENTURA B. & ASOC. LTDA.	
CONTENIDO SONDAJE S. P. T. Nº 2, EN TERRENO UBICACION PRELIMINAR ESTRUCTURAS EJE PRAT SECTOR 3.	
UBICACION	CONCEPCION
ESCALA	FECHA
GRAFICO	DIC. ' 91

TELÉFONO: 497207 - 2251608 - 2516587 - FAX: (562) 2251608 - SANTIAGO - CH

Source: W. Neely

Figure 302. Illustration. Boring log S-2 for site 28.

Ubicación : Boring No. 2

Fecha : 30/11/91

Entre colas: (m)		N ₁ *	N ₂ **	Entre colas: (m)		N ₁ *	N ₂ **
1.02	1.47	4	6				
1.96	2.41	4	5				
3.18	3.63	2	5				
4.02	4.47	9	9				
5.08	5.53	10	26				
6.16	6.51	9	7				
7.02	7.52	SHELBY					
7.83	8.22	9	25				
8.72	9.09	29	83*				
9.59	10.04	29	30				
10.58	10.95	32	79*				
11.62	12.08	36	91				
12.63	12.84	30	50*				
13.52	13.97	33	101				
14.62	15.08	30	94				

N₁ =number of blows per 15 cm.

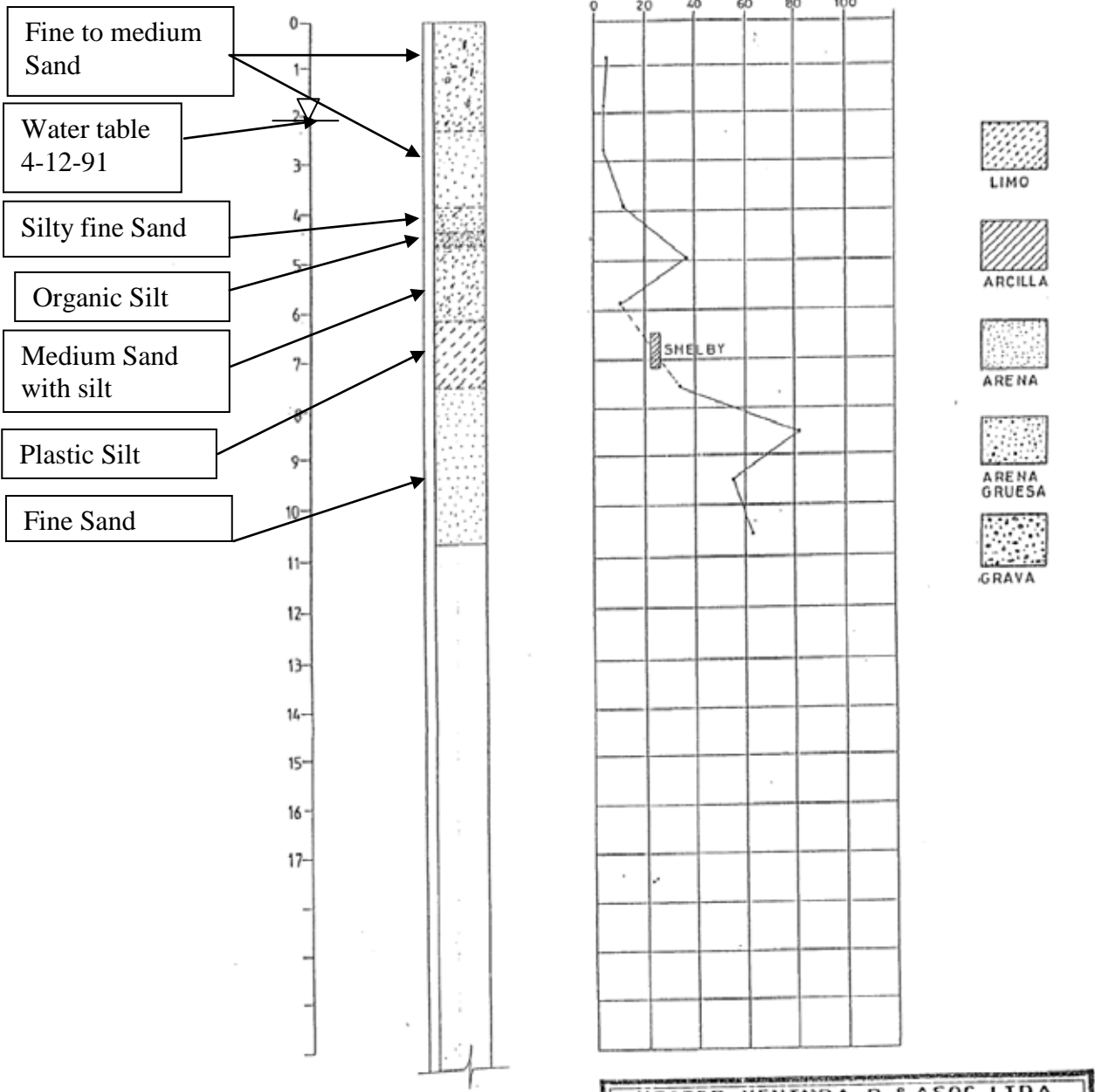
N₂ =number of blows per 30 cm.

Entre colas = depth range.

1 cm = 0.39 inches.

Source: W. Neely

Figure 303. Illustration. Detailed standard penetration test blow counts for boring log S-2 for site 28



HECTOR VENTURA B. & ASOC. LTDA.	
CONTENIDO SONDAJE S.P.T. N°3 EN TERRENO UBICACION PRELIMINAR ESTRUCTURA EJE PRAT SECTOR 3	
UBICACION	CONCEPCION
ESCALA GRAFICO	FECHA DIC. '91

RRITZ 1953 - TELEFONOS: 497207 - 2251606 - 2516567 FAX: (562) 2251608 - SANTIAGO - CHILE

Source: W. Neely

Figure 304. Illustration. Boring log S-3 for site 28.

Ubicación : Boring No. 3

Fecha : 4/12/91

Entre colas: (m)		N ₁ *	N ₂ **	Entre colas: (m)		N ₁ *	N ₂ **
0.57	1.02	4	5				
1.61	2.06	2	4				
2.56	3.01	1	4				
3.66	4.11	2	12				
4.70	5.15	14	37				
5.62	6.07	15	10				
6.47	7.17	SHELBY					
7.52	7.77	9	34				
8.28	8.73	26	82				
9.34	9.64	27	55*				
10.41	10.71	29	63*				

N₁ = number of blows per 15 cm.

N₂ = number of blows per 30 cm.

Entre colas = depth range.

1 cm = 0.39 inches.

Source: W. Neely

Figure 305. Illustration. Detailed standard penetration test blow counts for boring log S-3 for site 28.

APPENDIX B. SEISMIC DESIGN REQUIREMENTS FOR BRIDGES AND WALLS IN CHILE

B.1 SEISMIC DESIGN REQUIREMENTS FOR BRIDGES

Section 3.1004 of the MOP Highway Handbook establishes the seismic design requirements for small to medium span bridges (viaducts, overheads, and pedestrian bridges) with span lengths less than 230 ft (70 m).⁽¹¹⁾ Longer bridges and those with special structural configurations (arches, suspension, and cable-stayed bridges) are not covered by these specifications.

The philosophy underlying these specifications is to ensure public safety, but significant damage and disruption to service is accepted. The ground motions and design forces are calculated based on a probability of exceedance of 10 percent in 50 years, which is equivalent to a return period of 475 years. For design purposes, the country is divided into nine regions from north to south and in three seismic zones from east to west. These zones are determined by the value of the PGA in stiff soil, as shown in table 8. Zonation maps are included in the seismic provisions for all of the nine regions. The map for central Chile is shown in figure 22.

Table 8. Seismic zones.

Seismic Zone	PGA, A_o	Seismic Coefficient
1	0.20 g	0.20
2	0.30 g	0.30
3	0.40 g	0.40

The effect of the soil stiffness on the values of PGA at a specific site are taken in account by multiplying the values in table 8 by a soil coefficient defined in table 9.

Table 9. Soil coefficients.

Soil Type	Description	S
I	Rock with measured shear wave velocity, $V_s > 2,600$ ft/s (800 m/s)	0.9
II	Very dense soil with measured shear wave velocity, $1,300$ ft/s (400 m/s) $< V_s < 2,600$ ft/s (800 m/s)	1.0
III	Soft to medium-stiff clays and sands. Unsaturated sands with $N > 20$ blows/ft	1.2
IV	Saturated cohesive soils with $S_u > 0.0036$ ksi (0.025 MPa)	1.3

S = Soil coefficient.

V_s = Shear wave velocity.

N = Blow count number.

S_u = Average undrained shear strength in top 100 ft (30 m).

For seismic zones 2 and 3, an importance coefficient is included in the calculation for seismic forces. Bridges are classified as either “essential” (importance coefficient I) or “other” (importance coefficient II).

Since scour around or under a bridge foundation may influence its seismic behavior, the consequences of this hazard are included in the design. Two values of a seismic scour index (PSS) are defined. A value of PSS equal to 1 requires 75 percent of the total depths of scour to be considered in design, and a value of 2 requires 100 percent of the total scour to be considered in design. The depth of scour is included in the determination of the height of the superstructure (substructure slenderness) and consequently affects the appropriate analysis method.

Four categories of seismic behavior are defined based on the PGA, PSS, and the importance coefficient, as shown in table 12.

Table 10. Seismic behavior categories.

PGA, A_o	PSS	Importance Coefficient	
		I	II
0.20 g	1	a	a
	2	b	b
0.30 g	1	b	b
	2	c	c
0.40 g	1	c	c
	2	d	d

B.1.1 Analysis Methods

One of five analysis methods is used in to determine the elastic seismic forces, depending on the geometry and importance of the bridge. These methods are: the seismic coefficient method, the seismic coefficient method modified by structural response, the modal spectral analysis method, the modal spectral analysis method using site-specific spectra, and the time history analysis method (linear and nonlinear).

B.1.1.1 Seismic Coefficient Method

This method is applied to simply supported bridges with a maximum of two spans (each less than 230 ft (70 m) and substructure heights less than 39 ft (12 m). The substructure height is measured between the seat and the foundation soil including the maximum scour effect. The horizontal seismic coefficient K_h is calculated as shown in equation 1.

$$K_h = K_I \cdot S \cdot \frac{A_o}{2g} \leq 0.10 \quad (1)$$

where:

K_I = importance factor defined in table 11.

S = soil coefficient defined in table 9.

A_o = peak ground acceleration defined in table 8.

g = acceleration due to gravity (32 ft/s² (9.8 m/s²)).

Table 11. Importance factor, K_I

Importance coefficient	K_I
I	1.0
II	0.8

In this method, all structural components are designed to be elastic, which means the response modification factor is equal to one. The analysis is done for both the longitudinal and transverse directions.

B.1.1.2 Seismic Coefficient Method Modified by Structural Response

This method is applied to simply supported bridges of more than two spans (spans lengths less than 230 ft (70 m)) and substructure heights less than 82 ft (25 m) including the maximum scour effect. The horizontal seismic coefficient K_h is calculated as shown in equation 2.

$$K_h(T_n) = \begin{cases} \frac{1.5 K_1 S A_o}{g} & T_n \leq T_1 \\ \frac{K_1 K_2 S A_o}{g T_n^{2/3}} & T_n > T_1 \end{cases} \quad V_b \geq 0.22 K_1 \cdot S \cdot \frac{A_o}{2g} \cdot P \quad (2)$$

where:

K_2, T_1 = spectral constants, defined in table 12.

T_n = natural period determined using simplified formulas (table 13) or exact methods.

V_b = total base shear in the bridge.

P = total weight of the bridge.

Table 12. Spectral constants, T_1 and K_2 .

Soil type	T_1	K_2
I	0.20	0.513
II	0.30	0.672
III	0.70	1.182
IV	1.10	1.598

Table 13. Approximate formulas for natural periods for bridges.

Structural system	Direction	Fundamental period	
Simply supported bridges	Longitudinal or transverse	Reinforced concrete support	$T_n = 2\pi \sqrt{\frac{0.3 W_p + W_u}{3 E_c I g} H^3}$
Continuous bridges with fix supports on intermediate substructure and rigid abutments. One superstructure end on a fix support	Transverse ¹	Reinforced concrete	$T_n = 2\pi \sqrt{\frac{0.3 W_p + W_u}{3 E_c I g} H^3}$
		Steel	$T_n = 2\pi \sqrt{\frac{0.3 W_p + W_u}{4.5 E_c I g} H^3}$
	Longitudinal	$T_n = \frac{\pi}{8} \sqrt{\frac{W_p}{E_c I g} H^3}$	

¹ This formula should not be applied to multiple column bents.

W_p = weight of the pier or column (ton).

W_u = weight of the superstructure supported on the pier or column (ton).

E_c =elastic modulus (ton/m²).

I = moment of inertia of the file or column in the direction of analysis (m⁴).

H = height of the pile or column, measured as the difference in levels between the seat and the foundation soil considering the maximum scour effect (m).

B.1.1.3 Modal Spectral Method

This method is applied to tall bridges with simple supported continuous bridges (spans lengths less than 230 ft (70 m)) and substructure heights greater than 82 ft (25 m) including the maximum scour effect. This method may be used in place of the seismic coefficient method and the seismic coefficient method modified by structural response.

The absolute spectral acceleration for the vibration mode m , $S_a(T_m)$ is calculated using equation 3.

$$S_a(T_m) = \begin{cases} 1.5 K_1 S A_o & T_m \leq T_1 \\ \frac{K_1 K_2 S A_o}{T_m^{2/3}} & T_m > T_1 \end{cases} \quad V_b \geq 0.20 K_1 \cdot S \cdot A_o \cdot P/g \quad (3)$$

where:

T_m = period of mode m .

The displacements, rotations, and forces in each structural element are calculated in both the longitudinal and transverse directions from the contributions of each of the vibration modes. The combination of the maximum modal values to obtain elastic response values are calculated using the expressions shown in equation 4 and equation 5.

$$S = \sqrt{\sum_i \sum_j \rho_{ij} S_i S_j} \quad (4)$$

$$\rho_{ij} = \frac{8 \xi^2 r^{3/2}}{(1+r)(1-r)^2 + 4 \xi^2 r (1+r)} \quad r = \frac{T_i}{T_j} \leq 1.0 \quad (5)$$

where:

$\sum_i \sum_j$ = summation of the contribution of the considered modes.

ρ_{ij} = coupling factor.

T_i, T_j = modal periods.

z = damping ratio and taken equal to 0.05.

The number of modes to be included in the analysis is chosen such that the summation of the effective mass ratios will be larger than 90 percent.

B.1.1.4 Modal Spectral Method Using Site-Specific Spectra

In special cases, MOP requires that the design of a bridge is based on the modal spectral method of analysis based and a spectrum developed for the specific site.

B.1.1.5 Linear and Nonlinear Time History Analysis

In specific cases, especially for bridges incorporating base isolation systems, MOP requires time history analysis, either linear or nonlinear, using synthetic accelerograms reflecting the site seismic risk and the soil conditions.

B.1.2 Response Modification Factors (R)

The design seismic forces for members and connections are calculated by dividing the elastic response values by a response modification factor R . Special detailing is required to accommodate inelastic behavior and the formation of plastic hinges when R factors greater than 1 are used. Values of these factors are summarized in table 14 for the longitudinal and transverse directions.

Table 14. Response modification factors (*R*).

Element	Longitudinal	Transverse
Supports		
Wall-type pier	3	2
Single column with foundation cap	3	3
Column bent with foundation cap	3	4
Inclined column with foundation cap	3	2
Piles or micropiles		
Individual	3	3
Batter piles	3	4
Inclined batter piles	3	2
Foundations¹		
Spread footing	1	1
Batter of piles	1	1
Drilled shaft	1	1
Caisson or foundation pile	1	1
Connections²		
Expansion joint	0.8	0.8
Bearing plate	0.8	0.8
Shear key	1	1
Bearing	1	1

¹ For bridges in seismic categories C or D, seismic forces are those developed by plastic hinges in the column. These forces are frequently less than those calculated using $R = 1$.

² Connections are all elements that transfer shear or axial loads from one point to another in the structure. Moment connections are not included in this definition.

B.1.3 Determination of Elastic Forces and Displacements

For bridges classified in seismic categories C or D, the elastic forces and displacement are calculated in both the longitudinal and transverse directions. For the case of curved bridges, the longitudinal direction is the chord joining the abutments.

B.1.4 Combination of Forces in Two Perpendicular Directions

The forces calculated independently in two perpendicular directions are combined to take in account the uncertainty in the direction of the seismic waves and the effect of the two horizontal components of the earthquake. Two load stages are considered. Load stage I is shown in equation 6, and load stage II is shown in equation 7.

$$F = 100\% F_L + 30\% F_T \quad (6)$$

$$F = 30\% F_L + 100\% F_T \quad (7)$$

where:

F = absolute value of force or moment for all structural members due to load combination.

F_L = absolute value of force or moment in the longitudinal direction.

F_T = absolute value of force or moment in the transverse direction.

B.1.5 Minimum Support Length

Minimum values for support lengths of beams are shown in equation 8 for seismic behavior categories A and B and in equation 9 for seismic behavior categories C and D.

$$N = (203 + 1.67L + 6.66H)(1 + 0.000125 \alpha^2) \quad (\text{mm}) \quad (8)$$

$$N = (305 + 2.5L + 10H)(1 + 0.000125 \alpha^2) \quad (\text{mm}) \quad (9)$$

where:

L = length of the bridge deck to the adjacent expansion joint, or to the end of the bridge deck; for hinges within a span, L is the sum of the distances to either side of the hinge; for single-span bridges, L is the length of the bridge deck (m).

α = angle of skew of support measured from a line normal to span (degrees).

$H = 0$ for abutments and single-span bridges; average height of columns supporting the bridge deck from the abutment to the next expansion joint (m); pier height (m) for columns and piers; average height of the adjacent two columns or piers (m) at hinges within a span.

B.1.6 Modified Design Forces for Structural Elements and Connections

The seismic design forces from load stages I and II are divided by the R factors to obtain modified design forces. These modified forces are combined with other loads to obtain the maximum load combination as shown in equation 10.

$$1.0(D + B + SF + E + EQM) \quad (10)$$

where:

D = dead load.

B = buoyancy.

SF = stream-flow pressure.

E = earth pressure.

EQM = elastic seismic forces for the load stages I and II divided by R .

B.1.7 Modified Design Forces for Foundations

The seismic design forces for spread footings, pile caps and micropiles shall be those from load stages I and II divided by the response modification factor $R = 1$ to obtain modified design forces. These modified forces are combined with other loads to obtain the maximum load combination as previously shown in equation 10.

The load combinations are based on division I-A of AASHTO's Standard Specifications.⁽¹⁰⁾

B.1.8 Seismic Design of Foundations, Abutments, and Retaining Walls

The specifications for the seismic design of these elements are covered in section 3.1003 of the Highway Handbook.⁽¹¹⁾

B.1.9 Seismic Design of Reinforced Concrete Elements

The design and construction of CIP reinforced concrete elements (columns, foundations, and connections) are required to satisfy the provisions of division I-A of the AASHTO specifications. If the design is based on the allowable stress method, all the stresses are increased by 33.3 percent. If this method is used for bridges in seismic categories C and D, conservative designs are to be expected unless the design is based on the maximum forces developed from plastic hinging.

B.1.9.1 Requirements for Columns

Section 7.6.2 of division I-A of the AASHTO specifications for seismic performance category C and D is followed.

B.1.9.2 Columns and/or Piers

Section 7.6.3 of division I-A of the AASHTO specifications for seismic performance category C and D is followed.

B.1.9.3 Column Connections

Section 7.6.4 of division I-A of the AASHTO specifications for seismic performance category C and D is followed.

B.1.9.4 Construction Joints in Piers and Columns

Section 7.6.5 of division I-A of the AASHTO specifications for seismic performance category C and D is followed.

B.1.9.5 Reinforced Concrete Micropiles

These elements are designed for elastic forces ($R = 1$). Alternatively, these elements may be designed using the maximum forces from the column or pier plastic hinges.

B.1.10 Forces from Plastic Hinges on Piers or Columns

Design forces for columns, piers, and foundations are determined from the maximum forces due to plastic hinges. The procedure for calculation of these forces is based on section 7.2.2 of division I-A of the AASHTO specifications.

B.1.11 Diaphragms

Due to the high values of vertical acceleration in seismic zone 3, the beams of bridges in this zone are connected by transverse beams (diaphragms).

B.1.12 Anchor Bars (Seismic Bars)

No.7 (22 mm) deformed bars are provided to resist a vertical seismic coefficient of $K_v = A_o/4g$. These bars are required to satisfy the provisions of ASTM A706. ASTM A 615M bars are permitted if the difference between the true yield force and the nominal value is less than 17.4 ksi (120 MPa) and the relationship between ultimate stress and yield stress is less than 1.25.

B.1.13 Lateral Stoppers (Shear Keys)

To avoid excessive lateral displacement of the superstructure due to seismic forces, lateral stoppers are provided on bent caps. The design force used for these stoppers is the seismic force acting in the transverse direction divided by four. These stoppers are required to have sufficient ductility to avoid the deck collapse. The height of these shear keys is required to be greater than 12 inches (300 mm) and a gap between the shear key and the superstructure is provided to accommodate the seismic displacement plus 2 inches (50 mm).

B.1.14 Seismic Joints

Seismic joints between deck segments have a minimum spacing to allow the displacements of the elastomeric bearings. The minimum spacing is given by equation 11:

$$S_j \geq 6.25 \frac{A_o}{g} + S_1 + S_2 \quad (\text{cm}) \quad (11)$$

where S_1 and S_2 are the seismic displacements of each of the elastomeric bearings in cm.

B.1.15 Seismic Isolation Systems

Seismic isolation systems used as supporting elements are designed and tested according to AASHTO's *Guide Specifications for Seismic Isolation Design*.⁽²¹⁾

B.2 SEISMIC DESIGN REQUIREMENTS FOR WALLS

Walls that are part of the public transportation system controlled by MOP are generally designed in accordance with the AASHTO Standard Specifications.⁽¹⁰⁾ PGAs given in the Chilean design guide for wall design are used (i.e., PGAs of 0.2, 0.3, or 0.4 g in zones 1, 2, or 3, respectively). MOP requirements allow concrete gravity walls to be designed for a reduced acceleration, providing that the wall can slide during shaking. For MSE walls however, MOP requirements do not allow the design acceleration to be reduced for internal and external wall stability. For walls not under MOP jurisdiction, design accelerations may be established as a site-specific value. In general, however, even these walls are designed using the AASHTO Standard Specifications.⁽¹⁰⁾

For MSE walls, typical practice is to select good, frictional backfill materials and overexcavate poorer soils, replacing them with the backfill materials. Because of this practice, a reinforcement length of 70 percent of the wall height is typically used to meet seismic design requirements.

ACKNOWLEDGMENTS

Financial support for the postearthquake reconnaissance trip to Chile was provided mainly by FHWA, with Sheila Duwadi serving as the point of contact for U.S. team members. The authors would also like to acknowledge the financial support of EERI. The findings and opinions expressed in this report are those of the authors and do not necessarily reflect those of the sponsors. Special thanks are due to José Miguel Ortega for his support and coordination with local authorities to make the reconnaissance trip a success, Mauricio Guzmán and Sandra Achurra for their escort and introduction to various bridge sites, Alex Unión Villarroel for his posttrip assistance, and Rodrigo Oviedo for his participation throughout the reconnaissance trip.

REFERENCES

1. Earthquake Hazards Program (2010). “Magnitude 8.8—Offshore Maule, Chile.” U.S. Geological Survey, Reston, VA. Accessed online: January 25, 2010. (<http://earthquake.usgs.gov/earthquakes/recenteqsww/Quakes/us2010tfan.php>)
2. GEER Association (2010). *Geo-Engineering Reconnaissance of the February 27, 2010 Maule, Chile Earthquake, Version 2, May 25, 2010*, Report No. GEER-022, Jonathan Bray and David Frost (Eds.). Accessed online: May 28, 2009. (http://www.geerassociation.org/GEER_Post%20EQ%20Reports/Maule_Chile_2010/Ver2_Cover_Chile_2010.html)
3. Ruegg, J.C., Rudloff, A., Vigny, C., de Chabaliér, J.B., Campos, J., Kausel, E., Barrientos, S., and Dimitrov, D. (2009). “Interseismic strain accumulation measured by GPS in the seismic gap between Constitución and Concepción in Chile.” *Physics of the Earth and Planetary Interiors* 175, pp. 78–85, Elsevier, San Francisco, CA.
4. Atwater, B.F., Musumi-Rokkaku, S., Satake, K., Tsuji, Y., Ueda, K., and Yamaguchi, D.K. (2005). *The Orphan Tsunami of 1700—Japanese Clues to a Parent Earthquake in North America*, Professional Paper 1707, U.S. Geological Survey and University of Washington Press, Reston, VA.
5. Earthquake Hazards Program (2010). “Seismicity Cross Section, Magnitude 8.8 Offshore Maule, Chile,” U.S. Geological Survey, Reston VA. Accessed online: January 25, 2010. (http://neic.usgs.gov/neis/eq_depot/2010/eq_100227_tfan/neic_tfan_c.html)
6. Boroschek, R., Soto, P., Leon, R., and Comte, D. (2010). *Terremoto Centro Sur Chile, 27 de Febrero de 2010, Informe Preliminar No. 4*, University of Chile, Department of Civil Engineering and Department of Geophysics, Santiago, Chile.
7. Barrientos, S. (2010). *Informe Técnico, Terremoto Cauquenes 27 Febrero 2010*, University of Chile, Department of Geophysics, Santiago, Chile. Accessed online: January 25, 2010. (http://ssn.dgf.uchile.cl/informes/INFORME_TECNICO.pdf)
8. National Strong-Motion Project (2010). “Offshore Maule, Chile, Earthquake.” U.S. Geological Survey, Reston, VA. Accessed online: January 25, 2010. (http://nsmp.wr.usgs.gov/data_sets/20100227_0634.html)
9. Flores, R. (1999). “Ingeniería Sísmica en Chile.” *Revista Chilena de Ingeniería* 428, Pontifical Catholic University of Chile, Santiago, Chile.
10. American Association of State Highway and Transportation Officials (2002). *Standard Specifications for Highway Bridges, 17th Edition*, Washington, DC.
11. Ministry of Public Works (2001). “Sección 3.1004, Diseño Sísmico,” *Manual de Carreteras*, Vol. 3, Santiago, Chile.

12. Kramer, S.L. (1996). *Geotechnical Earthquake Engineering*, Prentice Hall, Upper Saddle River, NJ.
13. Washington State Department of Transportation (2010). *Geotechnical Design Manual*, Publication No. M46-03, Olympia, WA.
14. American Association of State and Highway Transportation Officials (2008). *AASHTO Guide Specifications for LRFD Seismic Bridge Design*, Washington, DC.
15. Vucetic, M., Tufenkjian, M.R., Felio, G.Y., Barar, P., and Chapman, K.R. (1998). "Analysis of Soil-Nailed Excavations Stability during the 1989 Loma Prieta Earthquake," *The Loma Prieta, California, Earthquake of October 17, 1989—Earth Structures and Engineering Characterization of Ground Motion*, Professional Paper 1552-D, United States Geological Survey, Washington, DC.
16. Collin, J.G., Chouery-Curtis, V.E., and Berg, R.R. (1992). "Field Observation of Reinforced Soil Structures Under Seismic Loading." *Earth Reinforcement Practice*, Vol. 1, pp. 223–228, A.A. Balkema Publishers, Netherlands.
17. Bathurst, R.J., and Cai, Z. (1995). "Pseudo-Static Seismic Analysis of Geosynthetic-Reinforced Segmental Retaining Walls." *Geosynthetics International*, Vol. 2, No. 5, pp. 787–830, ICE Publishing, London.
18. Tatsuoka, F., Koseki, J., and Tateyama, M. (1996). "Performance of Reinforced Soil Structures during the 1995 Hyogo-ken Nanbu Earthquake," *Earth Reinforcement*, Special Report, pp. 1–36, A.A. Balkema Publishers, Netherlands.
19. Koseki, J., Bathurst, R.J., Guler, E., Kuwano, J., Mauerger, M. (2006). "Seismic Stability of Reinforced Soil Walls." Presented at 8th International Conference of Geosynthetics, Yokohama, Japan.
20. Anderson, D.G., Martin, G.R., Lam, I.P., and Wang, J.N. (2008). *Seismic Analysis and Design of Walls, Buried Structures, Slopes, and Embankments*, NCHRP Report No. 611, Transportation Research Board, Washington, DC.
21. American Association of State and Highway Traffic Officials (1999). *Guide Specifications for Seismic Isolation Design, 3rd Edition*, Washington, DC.

